UC Berkeley
UC Berkeley Electronic Theses and Dissertations

Title

Exploring Biofabrication and Print State Detection in Tomographic Volumetric Additive Manufacturing

Permalink

https://escholarship.org/uc/item/3mr436r9

Author

Luk, Sui Man

Publication Date

2024

Peer reviewed|Thesis/dissertation

eScholarship.org Powered by the California Digital Library
University of California

Exploring Biofabrication and Print State Detection in Tomographic Volumetric Additive Manufacturing

By

Sui Man Luk

A dissertation submitted in partial satisfaction of the

requirements for the degree of

Doctor of Philosophy

in

Biophysics

in the

Graduate Division

of the

University of California, Berkeley

Committee in charge:

Professor Hayden Taylor, Co-Chair
Professor Sanjay Kumar, Co-Chair
Professor Kevin Healy
Maxim Shusteff

Spring 2024

Abstract

Exploring Biofabrication and Print States Detection in Tomographic Volumetric Additive Manufacturing

By

Sui Man Luk

Doctor of Philosophy in Biophysics

University of California, Berkeley

Professor Hayden Taylor, Co-Chair

Professor Sanjay Kumar, Co-Chair

The intricate interplay between cellular microenvironments and the development of tissue constructs, particularly the dynamics of cell proliferation and vascular formation within hydrogel matrices, has attracted great interest in the tissue engineering field and motivated numerous innovations from the biofabrication community. In particular, the recent invention of volumetric additive manufacturing (VAM) opens unique opportunities in bioprinting because it offers geometric freedom, enables overprinting, and imposes fewer rheological constraints on the printing material than traditional bioprinting methods do.

This dissertation presents the use of Computed Axial Lithography (CAL), an implementation of tomographic VAM, to fabricate complex, perfusable structures within biomaterial hydrogels. These hydrogels, exhibiting storage moduli as low as a few hundred pascals, support the formation of extensive microcapillary networks, indicating their potential to replicate tissue systems. Additionally, this dissertation introduces an innovative perfusion device designed for contact-free CAL printing and subsequent processing of these hydrogel constructs. This device also demonstrates CAL's ability to intricately overprint soft structures onto pre-existing solid components.

This dissertation concludes by presenting a novel print visualization method that leverages the temperature and curing-sensitive fluorescent properties of Rhodamine B (RhB). This technique, a first in the field, demonstrates real-time sensing capabilities in VAM, paving the way for advanced measurement systems that can precisely gauge both temperature and degree of conversion (DOC) during the printing process. This innovation lays foundational work for future research in the domain.

Acknowledgments

I want to thank my advisor, Prof. Hayden Taylor, for his guidance and the opportunity to explore the fascinating world of AM and the many incredible things AM can achieve. My heartfelt thanks also go to my thesis committee members: Prof. Sanjay Kumar, Prof. Kevin Healy, and Dr. Maxim Shusteff. I especially thank Maxim and his colleagues at Lawrence Livermore National Laboratory for being long-standing collaborators in this work and many others in our group. I am grateful to the Biophysics program members: Kate Chase, Prof. Susan Marquesee, and Prof. Ahmet Yildiz who supported my program study at important times.

My lab life is enriched by the many colleagues I have: Chi Chung (Alvin) Li, Joeseph Toombs, X (Yaxuan) Sun, Nour Akiki, Taylor Waddell, Jennings Ye, and Abrar Amin Khan have all provided valuable research discussions as well as fun times together. I thank Dr. Hossein Heidari for being the pioneer of the biofabrication work in our group and for his work that produced some of the data reported in this dissertation (credits in corresponding figure captions). I also thank Quinten Thijssen, Dr. Elizabeth Gill, Dr. Yongdeok Kim, Dr. Karen Dubbin, Dr. Monica Moya, Dr. Rick Hynes, Dr. Martin de Beer, Dr. Erika Fong, Dr. Sijia Huang, Caitlyn Krikorian, and Daniel Wang for bringing stimulating perspectives to our work. My appreciation goes to Paul Lum, Mary West, Alison Killilea, Scott McCormick, Alex Jordan, and Dan Chapman for tirelessly running the core research facilities (Biomolecular Nanotechnology Center, QB3 Cell & Tissue Analysis Facility, Cell Culture Facility, Mechanical Engineering Student Machine Shop, and CITRIS Invention Lab).

PhD is not only a journey for academic pursuits but also self-discovery. My gratitude and love go to my friends and mentors who have supported me from time to time and made me who I am today.

Chapter 5 of this thesis is adopted from a previously-published conference proceeding in the 34th Annual International Solid Freeform Fabrication Symposium: “Probing Temperature and Degree-of-conversion States via Tomographic Fluorescence Imaging”, co-authored with Chi Chung (Alvin) Li, Joeseph Toombs, Martin de Beer and Prof. Hayden Taylor. I thank the co-authors for their hard work and insights toward the research project.

Table of contents

Abstract 1

Acknowledgments i

Table of contents ii

List of figures vi

List of tables x

Chapter 1 1

Introduction to bioprinting 1

1.1. Biofabrication technologies 1

1.1.1. Extrusion bioprinting 2

1.1.2. Inkjet bioprinting 2

1.1.3. Two-photon polymerization 3

1.1.4. Stereolithography/Digital Light Processing 3

1.1.5. Volumetric AM 3

1.2. Biological significance of soft materials 5

1.3. Importance of vascularized tissue model 6

1.3.1. Engineered microvasculatures 7

1.4. Structure of this thesis 7

Chapter 2 9

Bioprinting methods 9

2.1. Computed Axial Lithography 9

2.1.1. Operation principle 9

2.1.2. Advantages of CAL for bioprinting 10

2.1.3. Implementation of CAL 10

2.2. MicroCAL system 11
2.3. Considerations related to hydrogel bioprinting with CAL 12
2.3.1. Radical inhibition by oxygen 12
2.3.2. Dark polymerization 13
2.3.3. Temperature 13
2.3.4. Cytocompatibility 14
Chapter 3 15
Development of perfusable bioprinting device 15
3.1. Perfusable device for CAL system 15
3.1.1. Design considerations 15
3.1.2. Development of capsule prototypes 16
3.1.3. Printing perfusable hydrogel structure in-capsule 17
3.2. Perfusable device for microCAL system 18
3.2.1. Design considerations 18
3.2.2. Cap prototypes 20
3.3. Discussion and summary 21
Chapter 4 23
Bioprinted constructs and characterizations 23
4.1. Biomaterial preparation 23
4.1.1. Hydrogels 23
4.1.2. Cell culture and preparation of cell-laden hydrogel precursors 24
4.2. CAL-printed perfusable structures 24
4.2.1. Acellular prints 24
4.2.2. Cellular prints 25
4.3. microCAL-printed perfusable structure 27

4.3.1. Choice of the degree of substitution and effect of radical inhibitor in Gel-MA 28
4.4. Cell seeding study 30
4.4.1. Planar seeding 30
4.4.2. Cell seeding chip—motivation and design 33
4.4.3. Chip assembly and sterilization 34
4.4.4. Gel casting and functionalization 34
4.4.5. Testing cell seeding conditions on the chip 34
4.5. Summary 36
Chapter 5 37
Probing temperature and degree-of-conversion states via tomographic fluorescence imaging ... 37
5.1. Introduction and Motivation 37
5.2. Methodology 38
5.2.1. Resin formulation 38
5.2.2. Absorbance/emission measurement and fluorescence calibration 39
5.2.3. Tomographic fluorescence imaging setup 39
5.2.4. Computational reconstruction 40
5.2.5. Electronic synchronization of patterning projection and image acquisition 40
5.2.6. Data acquisition, processing, and tomographic reconstruction pipeline 41
5.2.7. Scattering observation by dark-field imaging 41
5.2.8. Derivation of the relation between spatial and fluorescence intensity resolution in tomographic imaging 42
5.2.9. Fourier transform infrared spectroscopy measurement 44
5.3. Temperature- and curing-dependent optical properties of RhB 45
5.4. Tomographic reconstruction of VAM-printed objects 48
5.5. Discussion and future work 51

5.6. Conclusion 52

Chapter 6 53

Future directions and conclusion 53

References 55

List of figures

Figure 1. Throughput versus resolution for several prevalent bioprinting techniques. DLP: Digital Light Processing, SLA: Stereolithography, EBP: Extrusion Bioprinting, EW: Electrowriting, MPL: Multiphoton Lithography, VP: Volumetric Printing. Reproduced from [7]. 2

Figure 2. The elastic moduli (E′) of different human body tissues, with common tissue engineering materials included for comparison. Reproduced from [39]. 5

Figure 3. (A) Underlying concept and (B) schematic of CAL system. Reproduced from [27]..... 9

Figure 4. Optomechanical setup of MicroCAL. Reproduced from [77]..... 11

Figure 5. Refractive index ($\Delta\hat{\boldsymbol{n}}$) vs time of a CAL print. The red-shaded section indicates the portion of the measurement in which the projected light was on. In the gray-shaded section, the patterning light was turned off and the refractive index continued to increase. Reproduced from [87]. 13

Figure 6. Schematic of capsule device and its placement in a CAL setup. 16

Figure 7. Illustration of capsule connector prototyping process, showing design generations in the order of time from left to right. Bullet points describe the design generations directly above. ... 17

Figure 8. An assembled capsule in open and closed modes. A two-channel hydrogel structure was printed in the capsule and was perfused with dyed water as shown in the open mode image. 17

Figure 9. Visualization of multiple insertion angles allowed by the current shell vial cap for needle puncture (black line), lowering the precision for needle insertion to the printed channel in the vial (red). 19

Figure 10. Terminologies used for microCAL capsule cap design. 19

Figure 11. Types of glass cut finishes. Shell vial is fire-polished, while a vial cut by a glass tube cutter gives a scribe cut-like finish. Adopted from [96]. 20

Figure 12. Representative views of CAD models of the (a) first- and (b) second-round prototype. 21

Figure 13. Capsule prototypes. (a) a glass tube with fire-polished end on the left and scribe-cut on the right; (b) the two caps optimized for each cut, inserted into the tube on each end; (c) an assembled capsule prototype filled with water. 21

Figure 14. Printing multivascular non-axisymmetric perfusable structures using CAL. (a) CAD model of a multi-vascular architecture featuring both straight and spiral channels; (b) the structure in (a) printed from 3 v/v % Gel-MA in 120 s; (c) CAD model of a triple-level branched architecture; (d) the structure in (c) printed from 5 v/v % Gel-MA in 100 s. Image credit for (a) and (c): Hossein Heidari. 24

Figure 15. Printing cell-embedded cylindrical disks with CAL. (a)–(c): a vertical stack of disks printed within a composite hydrogel containing 3 w/v % Gel-MA (a), 5 w/v % Gel-MA (b), and 7.5 w/v % PEG-DA-700 and 5 w/v % Gel-MA hydrogel (c). (d)–(f): fluorescence images of disks printed in materials in (a)–(c) cellularized with HUVEC at 0h and stained with calcein-AM (green) and ethidium homodimer-1 (red) at 24h. (g)–(i): fluorescence images of disks printed in materials in (a)–(c) cellularized with HMEC-1 at 0h and stained with calcein-AM (green) and ethidium homodimer-1 (red) at 24h. Scale bars: 200µm. Experiment and image credit: Hossein Heidari. 25

Figure 16. HMEC-1 and HUVEC viability 24h after printing embedded in 3 w/v % Gel-MA, 5 w/v % Gel-MA and 5 w/v % Gel-MA + 7.5 w/v % PEG-DA-700, respectively. Control: petri dish culture with the same media and duration. Experiment credit: Hossein Heidari..... 26

Figure 17. Development of HMEC-1 networks within the hydrogel prints from 3 w/v % Gel-MA, 5 w/v % Gel-MA and 5 w/v % Gel-MA + 7.5 w/v % PEG-DA-700, imaged after 7 and 11 days of culture. Orange: Alexa Fluor 594 phalloidin, blue: DAPI. Scale bars: 200 µm. Experiment and image credit: Hossein Heidari..... 27

Figure 18 (a) light projection of a trifurcated structure, color bar: normalized light dose; shadowgraph of (b) 50% and (c) 90% DS Gel-MA after printing the trifurcated structure under the same exposure times. The structure overcured in both instances but (c) is more visible on the shadowgraph. 28

Figure 19. Printing linear channel with microCAL. (a) Light projection of a linear channel rotated 45° from vertical to accommodate for the optomechanical configuration in microCAL. Colorbar: gray value of projector pixel; (b) photograph of the channel printed from 5 w/v % 90% DS Gel-MA + 0.33mM TEMPO + 6.78 mM LAP. Scale bar: 300 µm..... 30

Figure 20. Cell adhesion on Gel-MA without surface treatment. Brightfield images of HUVEC at 0 h and 36 h of culture, and HMEC-1 at 12 h of culture on 3 w/v % and 5 w/v % Gel-MA respectively. The dark regions in the HMEC-1 3 w/v % Gel-MA sample were caused by gel ruptured during washing. Scale bars: 500 µm (first two columns) and 530 µm (last column). ... 32

Figure 21. HMEC-1 adhesion on Gel-MA improved after surface treatment with gelatin. Brightfield images of HMEC-1 at 36 h of culture on 1% gelatin-treated 3 w/v % and 5 w/v % Gel-MA, and on non-treated 3 w/v % Gel-MA, respectively. Scale bars: 100µm..... 32

Figure 22. Confluent HMEC-1 on planar Gel-MA of different concentrations, both coated with 1% gelatin. Blue: DAPI, orange: Alexa Fluor 594 phalloidin. Seeding density: 2000 cell/mm^2, passage number at seeding: 8. Scale bars: 200µm..... 33

Figure 23. (Top) Schematic of cell seeding chip showing terminology and key dimensions. (Bottom) An overview of the workflow for chip assembly, seeding and perfusion..... 33

Figure 24. Endothelial cells (HUVEC) adhering to a substrate consisting of 5 w/v % Gel-MA that has been functionalized with 1 w/v % gelatin, which exhibit a cobble-stone-like morphology. . 35

Figure 25. Schematic of tomographic fluorescence imaging system presented in this work..... 39

Figure 26 Real-time FTIR data of acrylate group conversion of PETRA + 5 μM RhB + 0.1 w/v% I369. 45

Figure 27. Normalized absorption (blue) and normalized fluorescence intensity (orange) of PETRA + 5 μM RhB upon excitation at 532 nm and normalized absorption of 2 mM I369 in isopropanol (gray). The 405 nm patterning light used in this study is plotted in purple. 45

Figure 28. Normalized absorption (blue) and normalized fluorescence intensity (orange) of PEG-DA-700 + 5 μM RhB upon excitation at 532 nm, and normalized absorption of 2 mM I369 in isopropanol (gray). The 405 nm patterning light used in this study is plotted in purple. 46

Figure 29. Fluorescence intensity (right axis) and relative fluorescence intensity compared to a baseline of 25°C and 0 mJ/cm^3 absorbed dose (left axis) of PETRA + 5 μM RhB + 0.1 w/v% I369, as a function of temperature and absorbed optical dose. The polymer precursor is excited at 532 nm. 46

Figure 30. Fluorescence intensity (right axis) and the relative fluorescence intensity compared to a baseline of 25 °C and 0 mJ/cm3 absorbed dose (left axis) of PEG-DA-700 + 5 μM RhB + 0.3 mM BAPO, as a function of temperature and absorbed optical dose. The polymer precursor is excited at 532 nm. 47

Figure 31. Absorbance of PETRA + 5 μM RhB + 0.1 w/v % I369 of various absorbed optical doses measured on a well plate. The onset of scattering is indicated by an increase in measured absorbance..... 48

Figure 32. (a) Geometry of trihelix target object; (b) raw fluorescence image captured at 166 s into printing of a trihelix, (c) geometry of pyramid truss target object; (d) raw image captured at 133 s into printing of a pyramid truss (black region at the bottom: bottom of the vial, grey region directly above: reduced fluorescence at the bottom of the pyramid truss). 49

Figure 33. Central vertical and horizontal reconstruction slices of relative fluorescence intensity during printing of a trihelix (a–f) and a pyramid target (g–l). Scale bars: 3 mm..... 50

Figure 34. (a) a vertical slice of the reconstructed trihelix print at an example time point (85.36 s); (b) temporal temperature profile at a location near the top of the trihelix structure (red dot in (a)), where absorbed dose is assumed to be zero. At this location, a spatial average is taken over relative intensity in nine adjacent voxels in the horizontal plane of reconstruction. The average intensity is then mapped to temperature with the material's response surface along the line of zero absorbed dose. The red star indicates the temperature value at the location at 85.36 s. 50

Figure 35. Illustration of obtaining material state information from RhB material response surface. Colored surface plot: response surface of PETRA + 5 μM RhB + 0.1 w/v % I369, in terms of fluorescence intensity relative to that at 25 °C and 0 mJ/cm^3 absorbed dose. The intersection of a specific reconstructed relative fluorescence intensity (gray plane) and the response surface gives a set of possible corresponding temperatures and absorbed dose (gray contour line). At spatial locations where the resin is unexposed (assumed absorbed dose = $\mathbf{0}\ \boldsymbol{mJ \cdot cm - 3}$), the temperature at that location is uniquely determined by the response surface (red star). 51

Figure 36. A printed trihelix object from captured fluorescence intensity. Scale bar: 1 mm. 51

List of tables

Table 1. List of 3D printed materials used for connector prototyping. From [84]–[86]..... 16

Table 2. Final dimensions in mm for microCAL capsule caps designed for fire-polished and scribe-cut glass tube ends. 20

Table 3. Testing print times with bisection method to obtain the optimal print time for a perfusable linear channel from 5 w/v % 90% DS Gel-MA + 0.33mM TEMPO + 6.78 mM LAP. Only print 5 resulted in a perfusable structure. 30

Table 4. List of seeding times and rotation screened, and the observed HUVEC adhesion in each case..... 35

Chapter 1

Introduction to bioprinting

This introductory chapter defines biofabrication and bioprinting methods and describes the current state-of-the-art technologies and their unique properties. The chapter also gives a brief overview of tissue stiffness and vascular tissue in the human body, and their significance, as motivations to fabricate soft vascular structures via bioprinting.

1.1. Biofabrication technologies

Biofabrication and bioprinting are emerging technologies increasingly utilized to precisely deliver cells, biomaterials, and biological factors, aiming to replicate the complex heterogeneity of natural tissues [1]. Biofabrication is defined as the coordinated assembly of cells and tissues [2]. While the ultimate goal of biofabrication is to print functional tissues and organs for transplantation, current drivers of its development include drug discovery, tissue regeneration, and medical devices [3], [4]. Biofabrication and bioprinting hold the promise of significantly transforming the drug development process, by enhancing the speed, cost-efficiency, and effectiveness of clinical trials, while also reducing the reliance on animal testing.

The most common techniques in biofabrication encompass bioassembly and bioprinting [2]. Bioassembly techniques in biofabrication strategies leverage forces such as acoustophoretic, magnetophoretic, electrophoretic, and photophoretic to arrange cells and spheroids into specific two-dimensional (2D) or three-dimensional (3D) configurations [5]. On the other hand, bioprinting involves using additive manufacturing (AM) methods to create tissues through the controlled spatiotemporal patterning of bioinks [6]. These AM methods can be classified based on their serial unit processes. Zero-dimensional (0D) process represents a deposition or conversion of a single point at a time, 1D refers to a single line, 2D for a plane, and 3D for a volume at a time. The dimensionality of these processes fundamentally influences both the scale and speed of printing achievable and is summarized in Figure 1.

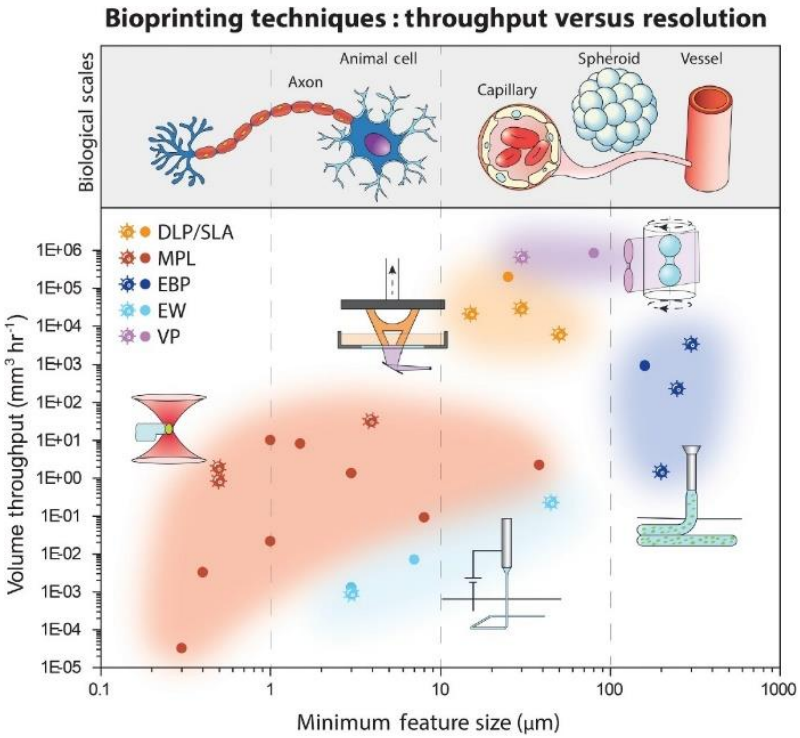


Figure 1. Throughput versus resolution for several prevalent bioprinting techniques. DLP: Digital Light Processing, SLA: Stereolithography, EBP: Extrusion Bioprinting, EW: Electrowriting, MPL: Multiphoton Lithography, VP: Volumetric Printing. Reproduced from [7].

1.1.1. Extrusion bioprinting

Extrusion bioprinting is a prevalent method in biofabrication, favored for its simplicity, adaptability, and compatibility with various bioinks [8]. It involves bioink being extruded through a nozzle using pneumatic pressure or mechanical force, applied by a piston or screw mechanism. Extrusion bioprinting allows an array of printing functions, including temperature control, ultraviolet (UV) curing, co-axial extrusion, and the use of interchangeable cartridges, enabling multi-material bioprinting [9].

Extrusion bioprinting has shown success in bioprinting cells, tissue scaffolds, and organ-on-a-chip devices for various applications such as tissue engineering, drug development, and cancer research [8], [10]. However, this method faces limitations in resolution, print speed, and microscale positioning due to the typically large nozzle used. The inherent 0D serial unit nature of extrusion also fundamentally limits print speeds, potentially leading to hypoxic conditions for cells in prolonged prints. Increasing extrusion rates can mitigate these issues but also raise shear stresses which may harm cell viability [11]. Therefore, achieving a balance between cell viability and structural complexity is essential, requiring precise tuning of nozzle impedance and extrusion rates.

1.1.2. Inkjet bioprinting

Inkjet bioprinting evolved from the inkjet printing technology developed in the 1950s [12]. In this approach, standard ink cartridges are substituted with cartridges filled with bioink, producing

droplets through piezoelectric actuation or thermal cavitation [13]. Its popularity stems from the affordability of its components, rapid printing capabilities, and the ability to pattern droplets over extensive areas [14]. The key benefits of inkjet bioprinting include its relatively high spatial resolution (around 50 μm droplets), fast dispensing rates (up to 10,000 droplets per second), and the cost-effective adaptation of existing inkjet technologies [15], [16]. However, it faces hurdles in accurately replicating tissue volumes with high resolution on a large scale due to constraints like small dispensing volumes, the necessity for low-viscosity bioinks (about 3–12 mPa·s), and significant shear stresses at the microscale opening [16].

1.1.3. Two-photon polymerization

Two-photon polymerization (2PP) is a technique for creating nanoscale structures [17]. It involves focusing pulses from an infrared laser into a volume of photosensitive resin, which either crosslinks (in negative photoresists) or decomposes (in positive photoresists) under energetic radiation [2]. This process, characterized by multiphoton absorption, displays nonlinear properties with a polymerization threshold, allowing for the direct creation of intricate 3D structures with ultra-high resolutions in the tens of nanometers range [18]. This exceptional resolution is due to the low probability of absorption outside the voxel, limiting reaction location. 2PP's capability for precise microarchitecture definition offers fine control over cell positioning, movement, and mechanical organization [19]. Although inherently a 0D-order process, significant advancements have been made to enhance its serial scanning speed and implement parallel processing techniques. Innovations aimed at accelerating fabrication include the use of multiple foci [20], Bessel beams [21], and multi-beam interference [22].

1.1.4. Stereolithography/Digital Light Processing

Stereolithography (SLA) or Digital Light Processing (DLP) techniques employ photochemical processes where light, usually UV or near-UV, triggers the polymerization of monomers into 3D networks. Stereolithography (SLA) technologies utilize a scanning laser beam, whereas digital light processing (DLP) technologies utilize a digital mirror device to rapidly mask light into 2D patterns [23].

A notable advancement aimed at enhancing DLP production rates is Continuous Liquid Interface Production (CLIP) [24]. It operates using a polymerization-inhibited dead zone, created by an oxygen-permeable curing window, which prevents the part from adhering to the bottom [25]. Like traditional DLP, CLIP offers a wide range of photoactive resins. The viscosity and reactivity of the monomers are critical, as slight variations significantly affect oxygen diffusion and consequently the dimensions of the dead zone, which is typically a minimum of 20–30 μm. In this region, diffused oxygen completely consumes initiating radicals to prevent polymerization and bottom adhesion. A major advantage of CLIP is its ability to create microscale features with z-axis print speeds reaching up to 1000 mm/h, significantly faster than conventional DLP methods [26].

1.1.5. Volumetric AM

Volumetric AM (VAM) represents a major shift away from traditional light-based AM by allowing for the simultaneous polymerization of all components of an object. While 0D, 1D, and 2D unit

processes can process points, lines, or cross-sectional layers at a time, volumetric techniques, as 3D unit processes, dynamically adjust light into specific locations to enable the concurrent curing of the entire structure within a vat of photosensitive resin. VAM processes can be divided into those that depend only on the superposition of intensity, namely tomographic methods [27], multi-beam intersection [28], and xolography [29], [30], and that which depends on controlling the phase of light (holography).

Multi-beam techniques involve the overlay of patterned optical fields created by several beams projected into a photosensitive resin [27]. The intersection of these multiple light beams results in the formation of a cured component [28]. On the other hand, xolography is a dual-color technique using photoswitchable photoinitiators to induce local polymerization inside a confined monomer volume upon linear excitation by intersecting light beams of different wavelengths [29]. The currently reported combination of molecular photoswitches and light sheet setup achieves a print resolution of approximately 25 μm in the x and y directions and 50 μm in the z-direction. Holographic lithography adopts spatial light modulators (SLM) for rapid display of different phase holograms where light can be directed in any pattern without the use of a mechanical stage or photomask. Compared to the point-by-point approach of two-photon polymerization (2PP), significantly faster fabrication speeds can be attained by sequentially generating applied holograms to create 3D structures, potentially accelerating the process by orders of magnitude.

Tomographic VAM takes inspiration from computed tomography (CT) [27]: it deposits a light dose to a vat of polymer from multiple angles in a uniaxial rotation, triggering polymerization where the light dose exceeds the curing threshold (this technology will be further discussed in Chapter 2). Tomographic VAM has attracted great interest from the bioprinting community since its conceptualization because of its speed (in tens of seconds) as well as its contactless and supportless printing mode. It has been used to print biomimetic structures including bone-like constructs [31], [32], liver organoid structures [33], and branched vessels [34]. The unique properties of tomographic VAM have also been explored for new bioprinting modalities such as filamented light (FLight) biofabrication for aligned microfilament growth [35] and scattering-corrected VAM [36]. Tomographic VAM has also been combined with other AM technologies to achieve multimaterial and multicell bioprinting, for example, melt electrowriting for tubular structures [37], and extrusion bioprinting for intricate geometry and co-culture models [38].

1.2. Biological significance of soft materials

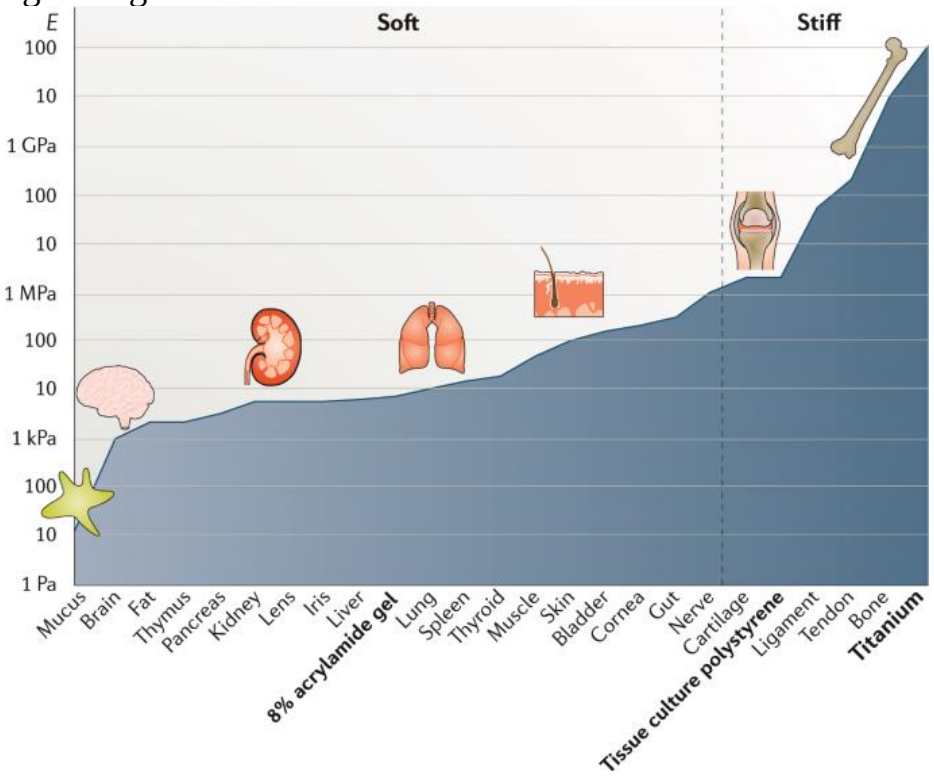


Figure 2. The elastic moduli (E′) of different human body tissues, with common tissue engineering materials included for comparison. Reproduced from [39].

In the human body, from the macroscopic level of organs down to microscopic blood vessels, there is a wide spectrum of mechanical properties. The stiffness of a material, a key mechanical property, is defined by its reaction to loads (forces applied) and deformations (resulting in shape changes). Stiffness is influenced by the material's type, quantity, and shape distribution, and can be described by moduli that relate to the intrinsic viscoelastic properties of materials. Under uniaxial forces, the storage modulus (E′) reflects a material's elastic behavior, showing how it stores and releases energy through bond stretching during loading and unloading. Conversely, the loss modulus (E″) indicates the viscous, time-dependent aspect, linked to irreversible internal changes like polymer chain slippage. In cases of shear forces, two analogous properties are assessed: the shear storage modulus (G′) and the shear loss modulus (G″). These are often measured using rheology and oscillatory experiments [39].

The human body comprises tissues that span a remarkable spectrum of stiffness; elastic moduli range from 20 GPa of cortical bone to 11 Pa of intestinal mucus. Between these extremes, almost all orders of magnitude are represented by a distinct tissue [39]. Bone tissues, being the hardest in the human body (10.4–20.7 GPa elastic moduli), form the skeleton support. Following in decreasing elastic moduli are other supportive structures including cartilage (250 kPa–3 MPa) [40], ligaments (25–93 MPa), as well as muscles (5–170 kPa). Softer tissues include abdominal organs like the pancreas (3 kPa) and liver (4–6.5 kPa), and ultimately, the brain (1–3 kPa), which is anatomically well-protected inside the skull.

Soft biomaterials are significant beyond modeling organs of their respective stiffness level (e.g. brain): this is because general tissue development moves towards increasing stiffness i.e. softer environments precede the emergence of stiffer ones [39]. For instance, in bone regeneration post-fracture, the process begins with softer materials like hematoma, granulation tissue, and fracture callus, which stiffen over time as ECM fibers accumulate and mineralize to form bone [41], [42]. Understanding the stiffening of early structures and their development into mechanically mature tissues naturally requires an understanding of softer biomaterials as the basis of engineered tissues.

1.3. Importance of vascularized tissue model

Another ubiquitous feature of human tissues is the vascular network. Nearly all body tissues have blood vessels, except for the cornea, cartilage, and skin epithelium [43]. It is found that only tissues with a maximum of 3×10^5 cells per cubic centimeter and less than 200 μm thickness can survive without active nutrient and oxygen transport by vasculature [44]. However, physiological cell density is in the order of 1×10^8 cells per cubic centimeter, necessitating high oxygen levels [45]. Engineered tissues or organs with such high metabolic needs cannot last without a supporting vascular network. Therefore, developing adequate vascular networks in engineered tissues is a significant quest in the field.

The principal function of the blood vascular network is the exchange of oxygen, nutrients, and waste. Large arteries with a diameter greater than 6 mm transport oxygen-rich blood to smaller arteries measuring 1–6 mm. This blood then flows into the arteriolar network, which ranges from 100–1000 μm in diameter, before reaching the capillary beds that are 10–15 μm wide. Venules carry oxygen-depleted blood away from the capillaries to larger veins, leading back to the heart. From there, blood is sent through the pulmonary artery to the lungs for reoxygenation. Endothelial cells (ECs) line the inner surfaces of all blood vessels, acting as a selective barrier for circulating immune cells, nutrients, hormones, and ions. In larger vessels like arteries and veins, the endothelium is encased in a thick basal lamina and one or more layers of smooth muscle cells, providing strength and durability. In contrast, capillaries are only surrounded by a thin basal lamina and scattered pericytes, which provide structural support during the formation of new blood vessels from existing ones (“angiogenesis”). The exchange of solutes mainly occurs in these small capillaries, either through gaps between the cells (“paracellular”) or through the cells themselves (“transcellular” transport) [43].

The self-assembly and remodeling of ECs, and angiogenesis, are highly dependent on matrix mechanical properties as well as the dynamics of blood flow. The pulsatile nature of blood flow applies cyclic tensile strain to ECs. Cyclic stretch within the physiological range (5–10%) significantly boosts proangiogenic growth factor secretion, microvessel sprouting, and lumen orientation [46]. However, higher cyclic stretch, indicative of pathological conditions, triggers endothelial inflammatory pathways and apoptosis [47]. Unidirectional laminar blood flow constantly applies shear stress to ECs. It has been shown that physiological shear stress plays a crucial role in promoting angiogenic sprouting, EC interactions, alignment, increased barrier functionality, and vessel maturation [48], [49], [50]. In contrast, nonphysiological shear stress can cause cytoskeleton disassembly, vascular leakiness, and inflammatory gene expression [51]. Physiological mechanical stimuli via vascular flow are critical in maintaining the growth, functions, and integrity of ECs on engineered vasculature.

1.3.1. Engineered microvasculatures

Recently, numerous biofabrication methods have been developed, leveraging advancements in lithography and AM. These techniques enable the engineering of vasculature with resolutions from meso- to microscale.

A more traditional approach utilizes molds and soft lithography to create channels with specific designs in polydimethylsiloxane (PDMS). These channels are sealed by bonding two PDMS or PDMS/glass layers, and ECs are then seeded to form a continuous endothelium lining. The maturity of the endothelium can be enhanced by applying shear stress [50], [52], [53]. The fluid flow through these channels can be mathematically modeled and adjusted according to channel dimensions [54], [55]. A limitation of this approach is the non-physiological rectangular shape of the channels. To overcome this, advanced lithography techniques like backside and dual-projection lithography have been employed to produce microvessels with circular cross-sections [56], [57]. In addition, PDMS is stiff relative to the tissue being modeled (elastic modulus around 1 MPa [58]), synthetic, and hydrophobic. It requires surface treatment for reduced hydrophobicity, and/or passivation with hydrophilic or biological molecules for proper cell and biomaterial adhesion, as well as aqueous flow. Soft lithography has also been used to create vessel-like structures in natural hydrogel materials, offering a more biologically relevant environment than PDMS.

As introduced in Section 1.1, AM allows for greater geometrical freedom compared to traditional lithography, a benefit for vasculature patterning. For example, freestanding vascular structures can be directly printed using coaxial nozzles in extrusion printing [59], [60]. Uniaxial channels can also be fabricated by extruding a sacrificial material within a bulk material to form a template structure, that is later removed to leave a lumen [61], [62], [63]. SLA has also been used for studying breast cancer metastasis to bone, utilizing Gel-MA/poly(ethylene glycol) di-acrylate (PEG-DA) with or without the addition of nano-hydroxyapatite [64]. Additionally, Grigoryan et al. used SLA to construct complex 3D vascular networks within biocompatible hydrogels, including a lung mimetic unit and a multi-material liver tissue, demonstrating the potential for creating functional tissues and advancing preclinical studies [65]. Recent developments in VAM have also demonstrated the technology's capability to print vasculatures in ECM-derived photopolymers down to about 100 µm diameter [33], [34]. Multimodal printing that combines VAM with another AM method to provide structural support [37] or finer patterning resolution [66], is also reported for vasculature fabrication.

1.4. Structure of this thesis

Biofabrication and bioprinting are innovative technologies used to precisely deliver cells, biomaterials, and biological factors for replicating the complex heterogeneity of natural tissues. These technologies, involving methods like extrusion bioprinting, inkjet bioprinting, and SLA, show potential in advancing drug discovery, tissue regeneration, and medical device development. In particular, engineered microvasculatures, crucial for tissue viability, are created using various advanced techniques like soft lithography and AM, allowing for the formation of vascular networks with meso- to microscale resolutions. VAM is well-positioned for vasculature fabrication because it allows geometrical freedom, rapid print speed, and contactless and supportless printing modes.

The remaining chapters of this thesis are dedicated to bioprinting with CAL and a related process monitoring method, tomographic fluorescence thermography (TFT).

Chapter 2 describes the CAL and microCAL methods and things to consider when they are applied to hydrogel bioprinting.

Chapter 3 documents the development of a perfusable bioprinting device for CAL, focusing on design and prototype development for both CAL and microCAL systems.

Chapter 4 then examines the bioprinted constructs and their characterizations, including biomaterial preparation, cell culture, and the effects of various factors on the bioprinted structures. Finally, it analyses the current status and challenges of this work, motivating the discussion of the development of a new CAL metrology method in the next chapter.

Chapter 5 explores TFT, which probes temperature and degree-of-conversion states via tomographic fluorescence imaging. The chapter covers resin formulation, fluorescence calibration, and the tomographic imaging setup.

Chapter 2

Bioprinting methods

So far, this dissertation has described the essential role of simulating soft tissue *in vitro* and the critical function of vascular networks in numerous organs and diverse tissue types. The present chapter introduces a tomographic VAM method, computed axial lithography (CAL), for bioprinting. I will discuss CAL's innovative aspects, unique capabilities for general and biology-related AM, and its setup. "MicroCAL" will also be introduced, a variant of CAL specifically designed to produce microscale features with a low étendue optical system, making it well-suited for fabricating physiologically-sized capillary structures.

2.1. Computed Axial Lithography

As discussed in Section 1.1, many of the limitations of current AM methods arise from their serial nature. Often, they require support structures to hold the part during fabrication. The print times for these methods can be lengthy, ranging from several minutes to hours. The layering process can lead to a "staircasing" effect, resulting in rough surface finishes. Additionally, the mechanical properties of the parts produced can be anisotropic, meaning they vary depending on the direction of the layers [67]. These characteristics pose inherent challenges in these types of AM processes.

Recent advancements in VAM have adopted an innovative approach, simultaneously polymerizing all points within a part by precisely controlling the three-dimensional accumulation of light exposure. Being a layer-less process, recent applications of VAM have shown its ability to fabricate centimeter-scale parts that are free from support structures and have low surface roughness, all within a matter of seconds to minutes [27]. VAM methods utilize optical and/or chemical nonlinearity to create 3D objects; in particular, tomographic VAM, also known as Computed Axial Lithography (CAL), as introduced by Kelly et al., draws several of its fundamental principles from CT [27].

2.1.1. Operation principle

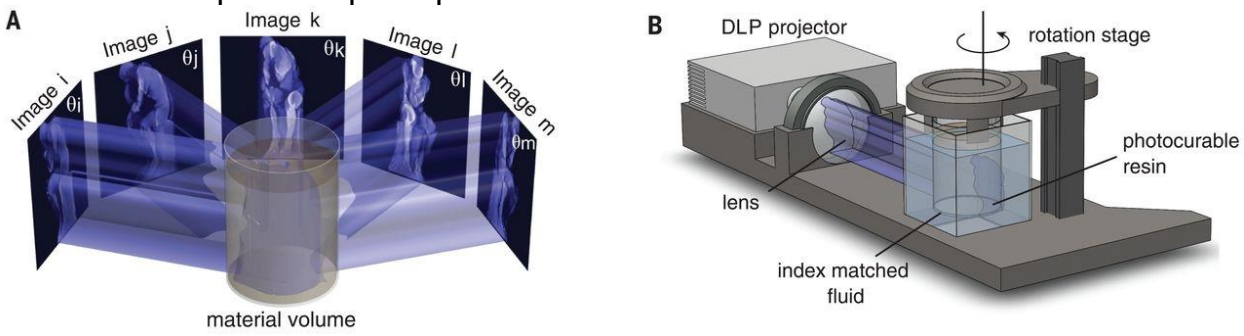


Figure 3. (A) Underlying concept and (B) schematic of CAL system. Reproduced from [27].

The operation of CAL takes inspiration from CT. In conventional CT imaging, X-rays are transmitted through a static subject from various angles. The attenuation of these X-rays, after passing through the subject, is recorded. This results in a series of 2D projections which are then used to reconstruct a 3D attenuation map of the subject.

CAL operates by selectively solidifying a photosensitive liquid within a defined volume. The system delivers light energy to the material in the form of a series of 2D images, where each of these image projections is directed through the material from a unique angle. Over time, the superposition of light exposures resulted in a 3D energy dose distributed throughout the material. At points where this dose exceeds the curing threshold of the photopolymer, the material solidifies, enabling it to take on the desired geometric shape (Figure 3).

In CT, reconstructing 3D objects from 2D axial projections is typically achieved using the Fourier slice theorem and various other iterative or direct algorithms. In CAL, variants of this reconstruction as well as other methods have been adapted and applied, including dose matching [27], penalty minimization [68], object space model optimization (OSMO) [69], [70], maximum likelihood-expectation maximization (ML-EM) [71], [72], a generalized L_p-norm model [73], and physics-incorporated methods such as those including ray tracing [74], occlusion [75], and molecular diffusion and reaction [76]. In this dissertation, an implementation of a penalty minimization scheme was used [68].

2.1.2. Advantages of CAL for bioprinting

In terms of bioprinting, CAL presents unique advantages. First of all, the resin provides a degree of mechanical support to the object during printing, so that the need for dedicated solid supporting structures is eliminated. This allows for intricate elements to be printed such as overhangs, moving parts, and complex lattice-like or porous networks typical of native tissues [32], [33]. Secondly, because of the lack of boundaries between lower dimensional units such as lines and layers, the prints tend to have a smooth surface finish. Thirdly, the overprinting capability allows for direct interfacing of the prints with the external world such as fluidic connectors for perfusion [27]. Lastly, unlike extrusion-based or layer-based processes, the lack of relative motion between the print and resin lifts many rheological constraints to the resins and allows us to work with highly viscous materials such as thermally-crosslinked hydrogels. The lack of shear stress to cell-embedded material and the minute-scale print times also help preserve cell viability [11].

2.1.3. Implementation of CAL

The CAL system developed in-house utilizes a digital video projector to emit computed intensity-modulated projections. These projections are synchronized with the rotation rate of the uncured photopolymer precursor material, ensuring precise timing and exposure (Figure 3).

The DLP projection system employed in this work was based on a Lightcrafter 4500 projector. This projector, featuring 4K resolution, was customized by Keynote Photonics. The light source in this setup was a 405 nm LED with an optical output power of 2.5 W. Control over the projection system was achieved through custom MATLAB scripts, which were programmed to display patterned intensity images using the 405 nm wavelength.

To collimate the light emitted from the built-in lens tube of the projector, two plano-convex lenses with focal distances of 100 mm and 200 mm were used. In the setup, the projector's image size at the central plane of the cylindrical build volume measured 130 mm by 75 mm. This configuration resulted in a nominal pixel size of 47 μm and a light intensity of about 25 mW/cm^2. Such a setup

was integral to the precise and effective printing of hydrogel structures, ensuring appropriate resolution and light intensity for the photopolymerization process. Each vial is rotated about its long axis using a motorized precision rotation mount (Thorlabs K10CR1) with a 3–25 °/s rotation rate. The coupling of the vial with the rotation stage is achieved using a magnetic kinematic coupling mount (Thorlabs SB1).

2.2. MicroCAL system

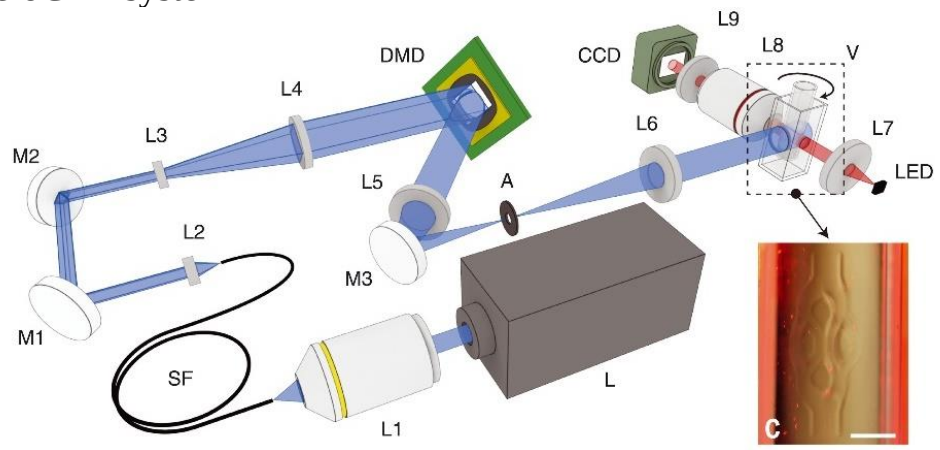


Figure 4. Optomechanical setup of MicroCAL. Reproduced from [77].

As detailed in Section 1.3, the size scale of physiological capillary vasculature is in the subhundred μm range, motivating microscale printing to replicate the geometry and the associated fluid dynamics. While multiphonon lithography can produce submicron-sized features that match the size scale of cells and smaller, they are generally limited to volumetric throughput of a few mm^3/h [7].

As an effort to enable volumetric microscale feature production in our group, a "microCAL" apparatus has been previously constructed in-house. In the previous CAL printer, LED illumination with a large optical étendue caused increased light divergence when the source size was reduced. This increased divergence led to blurred optical doses, decreasing the resolution of printed features. MicroCAL couples a laser light source into an optical fiber with a small mode field size and low numerical aperture, and demagnifies the light pattern defined by the digital micromirror device. The system's étendue is then minimized hence the divergence and blurring of light [77].

The optomechanical setup of MicroCAL is detailed in Figure 4 [77]. A 442 nm continuous wave laser is directed into a square core fiber (SF) by Lens 1 (L1), producing a square light intensity that efficiently fills the rectangular digital micromirror device (DMD). Lens 2 (L2) collimates this output, and Mirrors 1 and 2 (M1, M2) align the beam into a beam expander (L3, L4), creating an expanded square beam. The DMD, rotated 45°, reflects light from its "on"-state pixels into the print container (V) through a 4f system formed by Lenses 5 and 6 (L5, L6), which can adjust the demagnification level to either 0.45× or 1.25×. An aperture (A) blocks unwanted diffraction orders from the DMD. Additionally, the LED, Lenses 7 to 9 (L7–L9), and a CCD camera form a shadowgraph system for *in situ* imaging. The rotated DMD allows for a maximum build volume determined by the revolution of a right isosceles triangle, resulting in build volumes of 54.9 mm^3

and 1147.5 mm³ for the 0.45× and 1.25× demagnification settings, respectively, assuming a low optical étendue.

Combined with gradient descent digital mask optimization [27], the microCAL system enabled rapid printing (within about 30 to 90 s) of microstructures with minimum feature sizes demonstrated to be 20 and 50 μm in polymer and fused silica glass, respectively. The ability of microCAL to print microscale hydrogel features is discussed in Section 4.3.

2.3. Considerations related to hydrogel bioprinting with CAL

This section aims to highlight the unique properties and challenges that emerge from tomographic volumetric printing, and how that translates to factors worth considering in hydrogel bioprinting with CAL.

2.3.1. Radical inhibition by oxygen

In CAL processes that employ free-radical polymerization, radicals can either propagate or react with dissolved oxygen. The reaction with oxygen is significantly faster, typically three to four orders of magnitude higher than the propagation rate. As a result, oxygen in the local environment is consumed first before the onset of radical propagation. This leads to a delay known as the inhibition period and also contributes to the nonlinear dose response [11].

Therefore, several key factors such as initiator-to-inhibitor ratio, species diffusion, and light intensity must be considered for effective process control. The initiator concentration should exceed that of oxygen to avoid extended or indefinite inhibition times. Feature size also impacts polymerization due to oxygen diffusion into illuminated regions, especially if the feature size is comparable to the oxygen diffusion length. This effect varies with the resin's viscosity; in low-viscosity PEG-DA resins (viscosity ~0.012 Pa·s), oxygen diffuses over 100 to 200 μm in just a few seconds [28], [78]. In contrast, in high-viscosity di-pentaerythritol penta-acrylate resins (viscosity ~10 Pa·s), oxygen diffusion is much slower, less than 2 μm over 20 seconds of printing time [78]. Adding radical scavengers such as 2,2,6,6-Tetramethylpiperidine 1-oxyl (TEMPO) has also been explored with acrylate and thiol-ene resins to create the necessary nonlinear threshold behavior for CAL (more in Section 4.3.1) [77], [79], [80].

In the context of bioprinted hydrogel scaffolds, it is generally recognized that cells embedded in scaffolds may suffer from hypoxia at a distance greater than 200 μm from the nearest vessel because of hindered diffusion of oxygen [81], [82]. While oxygen's diffusion coefficient in room-temperature water (2.42×10^{-9} m^2 /s) sets an upper limit for the diffusivity of oxygen in hydrogels, measurements of oxygen's diffusion coefficients in both acellular and cellularized hydrogels revealed that the value falls in a range below the upper threshold in water (2.4×10^{-10}–$1.2\times10^{-9}m^2/s$) depending on hydrogel concentration and cell density [83], [84]. It also also been observed in-house that Gel-MA prints exhibit nonuniformity along the direction of oxygen gradient in the vial, an effect that is thought to arise from the diffusion of oxygen from the liquid-air interface at the top of the vial [85]. Besides using standard oxygen sensors [86] to determine oxygen diffusion coefficients in hydrogels, a method akin to Fluorescence Recovery After Photobleaching (FRAP)

has also been reported by Orth *et al.* for *in situ* measurement of oxygen re-diffusion in DUDMA/PEG-DA and DUDMA resins [78] and shows potential to be applied to hydrogels.

2.3.2. Dark polymerization

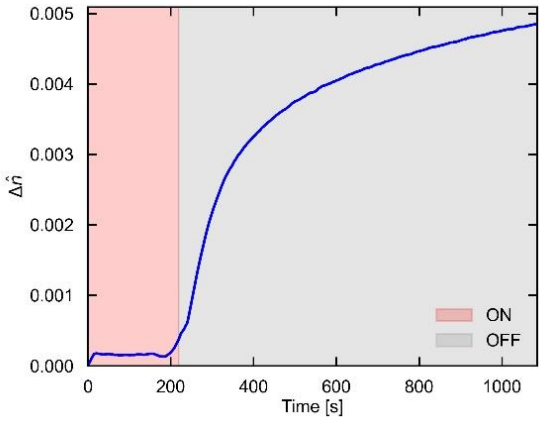


Figure 5. Refractive index ($\Delta\hat{n}$) vs time of a CAL print. The red-shaded section indicates the portion of the measurement in which the projected light was on. In the gray-shaded section, the patterning light was turned off and the refractive index continued to increase. Reproduced from [87].

In free-radical polymerization, the rates of photoinitiation, propagation, and termination reactions determine the overall polymerization speed. As the monomer is consumed, the rate of termination reactions slows down compared to photoinitiation and chain propagation. This leads to continued polymerization after the light source is turned off (termed "dark polymerization"), lasting until all free radicals are either depleted or recombined, and all active chains terminate.

Dark polymerization has a more pronounced impact on parts created using CAL than those produced by conventional stereolithography, mainly due to CAL's tomographic nature. Unlike stereolithography, where light is restricted to the boundaries of the layer being printed, tomographic VAM exposes the out-of-part monomer. Consequently, dark polymerization can cause overcuring of adjacent background resin, leading to the outgrowth of gelled regions and dimensional errors in the final part. It also complicates achieving accurate material properties, such as refractive index, in the patterned part, affecting applications and processes reliant on the conversion state [87].

2.3.3. Temperature

Print temperature affects monomer packing in photopolymer precursor; therefore, it plays a role in determining the structure and rheological properties of the crosslinked polymer network. This is even more significant in hydrogels that are already thermally crosslinked at the time of printing. It has been shown that Gel-MA photopolymerized after thermal gelation has up to eight times higher storage modulus (G′) compared to Gel-MA in liquid form under 37 °C [88].

Besides, temperature is a critical factor in the photopolymerization process itself due to its ability to auto-accelerate the reaction and induce mechanical and optical changes in the material. These effects will be discussed in further detail in Chapter 5.

2.3.4. Cytocompatibility

Living cells can be damaged during bioprinting from various stimuli, including shear stress, thermal stress, and radiative stress. The extent of cell injury depends on both the intensity and duration of these stimuli. When the stresses applied surpass a cell's tolerance threshold, irreversible damage occurs, potentially leading to cell death through mechanisms like apoptosis [89].

Although mechanical stress to cells is less of a concern in VAM than in other AM processes, cells will be exposed to UV/visible light illumination, elevated temperature from exothermic photopolymerization, and free radicals. UV radiation induces mutagenic and cytotoxic DNA damage [90] and can be avoided in the CAL process by selecting water-soluble photoinitiators that absorb at visible wavelengths, such as lithium phenyl-2,4,6-trimethylbenzoylphosphinate (LAP), ethyl phenyl(2,4,6-trimethylbenzoyl)phosphinate (Li-TPO-L) [80] and tris(2,2-bipyridyl)dichlororuthenium(II) hexahydrate/sodium persulfate (Ru/SPS) [91]. The print and postprocessing time, as well as photoinitiator concentration, should be optimized to minimize the heat stress and radical species the cells are exposed to, and the time away from nutrients and oxygen.

Chapter 3

Development of perfusable bioprinting device

As mentioned in Section 1.3, approaches for regulating fluid flow within structured vascular networks are essential in creating physiologically relevant tissue constructs for regeneration medicine and *in vitro* physiological studies. Bioprinting on tomographic VAM systems presents unique challenges and opportunities because of the axisymmetric configuration at printing, the absence of motion between the print and surrounding resin, and the fact that resin can be enclosed throughout the entire print process. This chapter introduces hardware designs and development for devices for perfusable bioprinting compatible with CAL and microCAL systems.

3.1. Perfusable device for CAL system

3.1.1. Design considerations

The fact that the resin can be enclosed from the surrounding environment during tomographic VAM allows sterile, potentially biohazardous materials to be patterned outside of the biosafety environment where the VAM system is located. This also necessitates the development of an enclosure for sterile biological materials. In the process of designing such an enclosure, several criteria were considered.

First, the device must be an airtight and sterile enclosure to shield sterile biological samples from the outside environment, as well as to support soft gel materials. The device should be transparent for photopolymerization, visual inspection as well as any potential imaging downstream. Since VAM is rotation-based, an axisymmetric chamber design would minimize the reflection of patterning light off the device surface and thus increase illumination efficiency. Finally, it should allow flexibility for the geometry of the perfusable print.

Based on the above criteria, a capsule-like device is designed to fit the CAL system in-house (Figure 6). It has a transparent gel chamber tube at the center which can be opened and closed via screw caps on the connectors. During printing, the caps are on which also serve as an adaptor to the clamping mechanism on the CAL setup. A user-defined vascular geometry would be printed inside the gel chamber that mates with the inlets and outlets. After printing, the caps are removed to expose the ports on the outside of the device, ready to be adapted to perfusion. The piece interfacing the gel chamber and the caps, termed “connector”, is fabricated with commercial 3D printers so that the number and positions of the gel chamber inlets can be readily modified via rapid prototyping. As for disinfection, the plastic tube and device can be disinfected in 70 v/v % ethanol and reused.

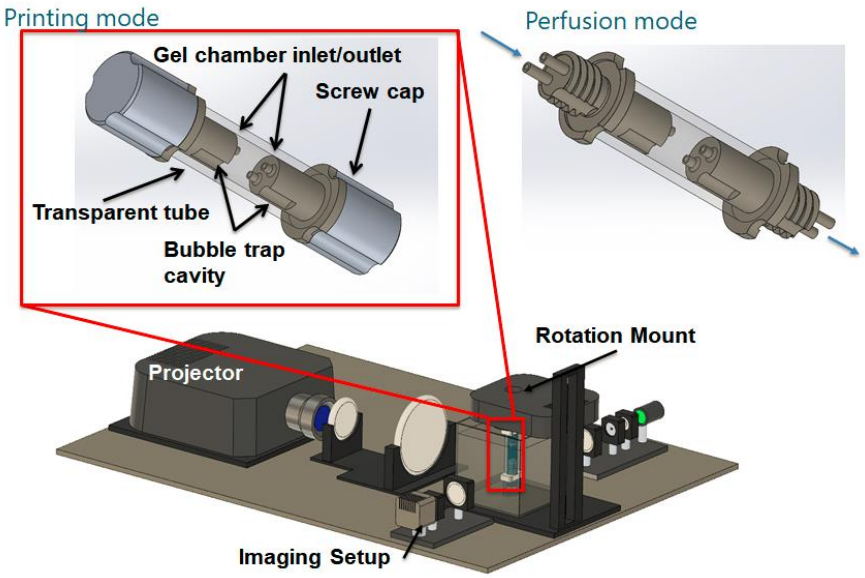


Figure 6. Schematic of capsule device and its placement in a CAL setup.

3.1.2. Development of capsule prototypes

The development of the cap and connector took several iterations, considering the material properties as well as the sealing and alignment requirements. The first generations relied on an interference fit between the gel chamber tube and the shaft of the connector for alignment. The flexible, rubbery material for the connector (Stratasys Tango) created an alignment issue since straight insertion of the gel chamber tube into the connector cannot be guaranteed by the compliant material. The third generation (Figure 7) incorporated rigid material (Stratasys Vero) to the connector and added a flat flap feature so that the tube mouth could be flush with the flap after insertion. Nonetheless, the lack of closure on the tubing side prompted a screw thread and complementary cap to be added for both capsule closure and alignment (generations 4–6). In addition, in later generations, an O-ring was added between the cap and the flap on the tubing size for sealing, bubble traps, air vents were added for air pressure management, and grooves were added to the flap to fix the rotation stage orientation relative to the connector. Finally, Formlabs Surgical Guide was adopted instead of Stratasys Vero for its certified biocompatibility.

Table 1. List of 3D printed materials used for connector prototyping. From [84]–[86].

Manufacturer	Name	3D printer type	Postprocessing method	Flexural Strength (MPa)	Tensile strength (MPa)
Stratasys	Tango	PolyJet	Support removal by water jet or alkaline bath	-	0.8-1.5
Stratasys	Vero	PolyJet	Support removal by water jet or alkaline bath	75-110	60-70
Formlabs	Surgical Guide	SLA	UV post-cure followed by cutting for support removal	≥102	-

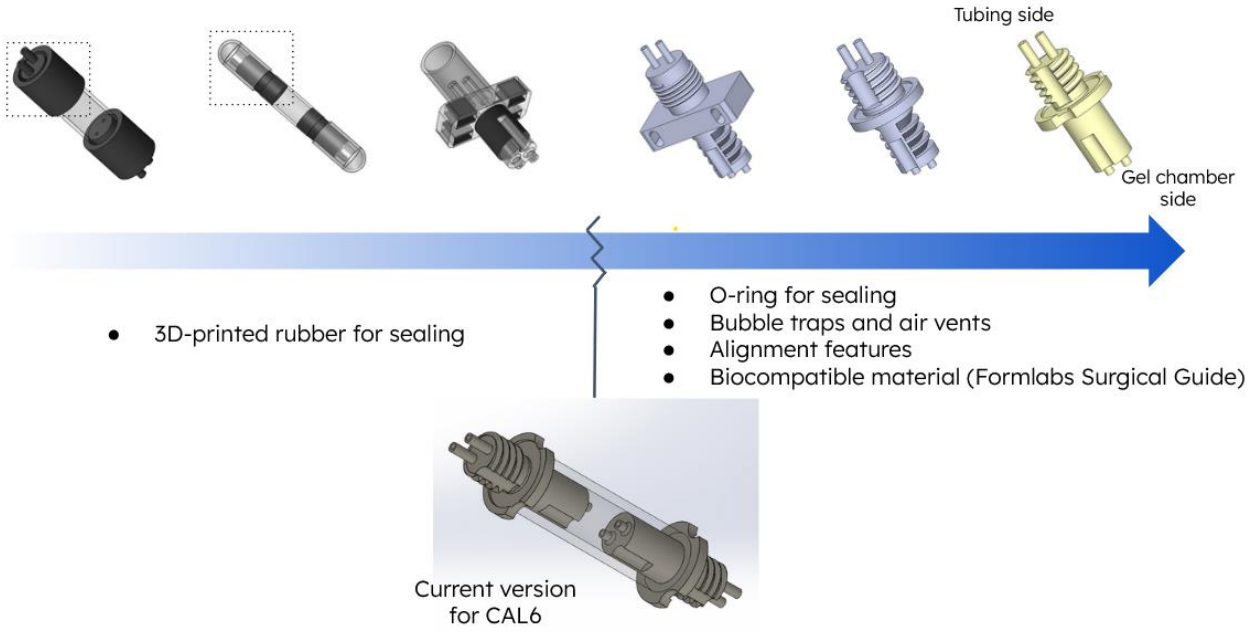


Figure 7. Illustration of capsule connector prototyping process, showing design generations in the order of time from left to right. Bullet points describe the design generations directly above.

3.1.3. Printing perfusable hydrogel structure in-capsule

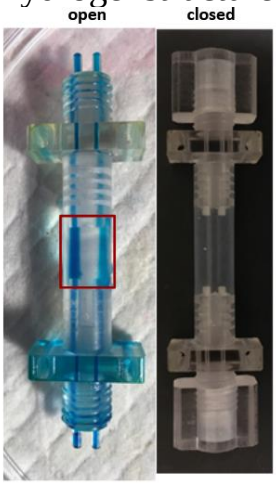


Figure 8. An assembled capsule in open and closed modes. A two-channel hydrogel structure was printed in the capsule and was perfused with dyed water as shown in the open mode image.

To assemble the capsule for sterile hydrogel printing, the parts (connectors, caps, gel chamber tubes) were first sterilized by soaking with 70 v/v % ethanol for 5 min, before being dried in air or an oven. Sterile hydrogel solution was prepared separately before the assembly. In a sterile environment, the capsule was assembled along the long axis, from bottom to top, to avoid bubble entrapment. A cap was filled with hydrogel solution and placed on the work surface before a connector was screwed on the cap. An identical cap-connector assembly would be prepared at the same time. A gel chamber tube was then inserted on top of the connector in one of the assemblies, which was subsequently filled with hydrogel solution using a pipette. The other cap-connector assembly would then be inserted into the filled tube, pressurizing the gel chamber, and allowing

bubbles in the hydrogel solution to escape. Throughout the process, the long axis of the assembly stayed vertical, and sufficient hydrogel solution was added to fill all the cavities without any airspace left.

Mounting the capsule to CAL requires minimal modification to the existing method since the same self-centering lens mount (Thorlabs SCL60C) is used for mounting both capsules and scintillation vials for engineering resins. For connectors with non-axisymmetric inlets/outlets on the gel chamber side, registering projection images with the capsule is necessary. The rotational-symmetric grooves on the cap allow for manual registration of the capsule to the rotation stage. Registering projection images with the rotation stage was done by adding a script to the open-source control program CAL-software-Matlab, that starts the projection at a designated angle of the rotation stage read by Thorlabs APT software.

The capsule prototype allows for soft perfusable structures to be printed in-capsule while closed, shielding the structure from the external environment until the point of perfusion (Figure 8). A controlled perfusion can be established by connecting the capsule to a peristaltic pump and a sterile medium reservoir.

3.2. Perfusable device for microCAL system

During the development and early implementation of the microCAL system, a glass shell vial (Thermo Fisher 6EKSHV8-1) was selected for resin containment because of its size and the good dimension tolerance associated with glass tube drawing. Designed for core chromatography systems [95], the shell vial comes with a flexible polypropylene push-fit cap that is puncturable with a needle for sample extraction. Both the vial and cap designs are beneficial to designing a perfusable microCAL device.

3.2.1. Design considerations

A perfusable device for microCAL was modified from the above glass shell vial. Special consideration was given to the cap design. As the cap has no needle guide and given the small dimension of prints anticipated, there is low precision tolerance for needle insertion in terms of both location and angle. Furthermore, the layer that the needle punctures at the cap is thin and flexible, allowing room for needle movement and slanting (Figure 9) as well as instability for clamping at microCAL. Given all resin in the vial should be either cured or removed after the print to avoid further reaction, clamping at the glass vial is not preferred since a portion of the resin will not be exposed.

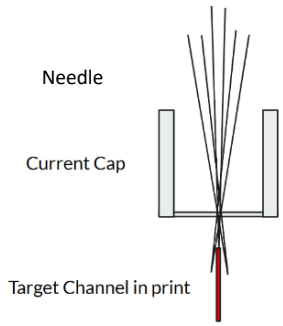


Figure 9. Visualization of multiple insertion angles allowed by the current shell vial cap for needle puncture (black line), lowering the precision for needle insertion to the printed channel in the vial (red).

In short, a new vial cap design is required to center the needle, while being compatible with the print material, maintaining ease of use by push-fitting to a fire-polish neck glass vial/tube and being stiff enough to be mounted in the microCAL system.

Several parameters have been defined to describe the fit and usability of the new cap (Figure 10). The inlet type refers to the needle guide at the cap inlet. The length of the clamp area is the length needed for the capsule to be clamped by the cap using microCAL's iris diaphragms. Snap flex refers to the overhanging flaps at the cap periphery; changing the snap flex width will change the bending stiffness at the push-fit section. On the other hand, different groove shapes will be needed per glass tube finish (Figure 11) to optimize fit. The tube's inner groove may improve the fit in case a polished glass tube is not available.

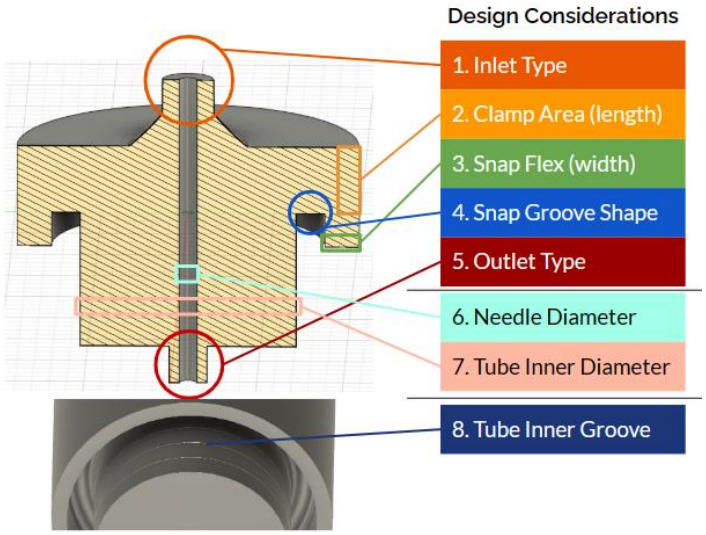


Figure 10. Terminologies used for microCAL capsule cap design.

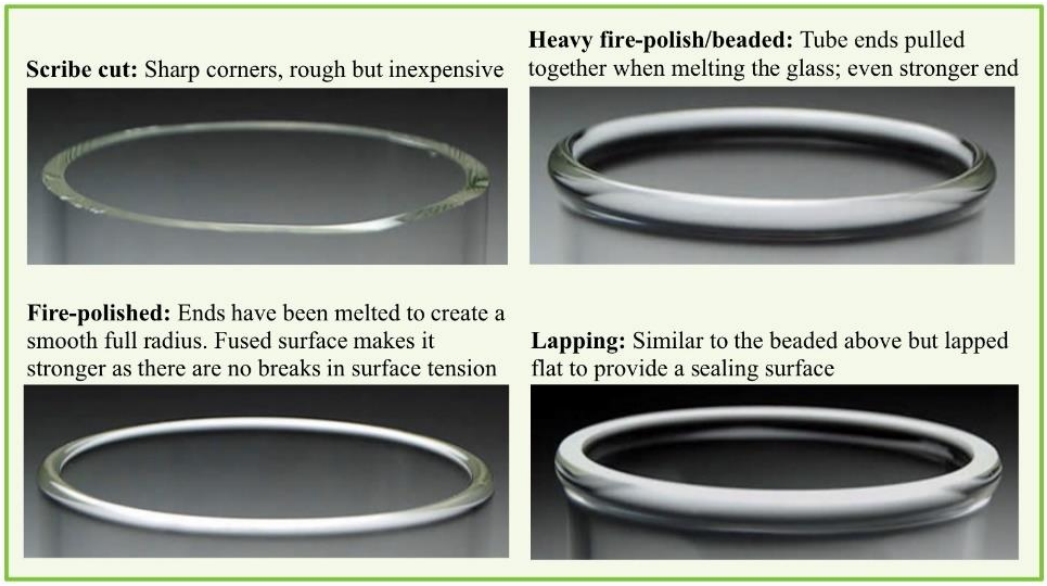


Figure 11. Types of glass cut finishes. Shell vial is fire-polished, while a vial cut by a glass tube cutter gives a scribe cut-like finish. Adopted from [96].

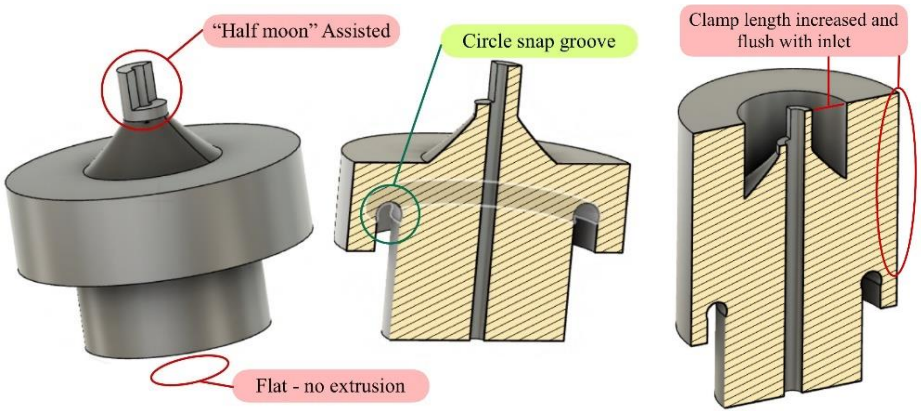
Table 2. Final dimensions in mm for microCAL capsule caps designed for fire-polished and scribe-cut glass tube ends.

Specifications	Fire-polished	Scribe-cut
Clamp area (length)	3	3
Snap flex (length)	3	3
Snap flex (width)	3	3
Snap groove shape	2	2
Needle diameter	4	4
Tube inner diameter	6	5

3.2.2. Cap prototypes

The CAD models were created using Autodesk Fusion 360 and were printed using an SLA printer (Formlabs Form3) with Durable resin. Formlabs printing was chosen as the prototyping method given its high resolution and a wide range of available materials. Durable resin was chosen as it simulates the strength and stiffness of polyethylene and is ISO-certified to be non-cytotoxic [97].

Three rounds of prototyping took place to compare and test different features of each design consideration mentioned above. The first prototyping rounds resulted in an assisted inlet shape, a circular snap groove, and a flat outlet (Figure 12). Round two of prototyping increased the clamp area length and made it flush with the inlet for easier clamping and push-fit of the cap. Round three optimized the dimensions of the features for fit as well as post-processing, where a manual washing step was added with an IPA-filled syringe to expel any resin out of the channel and the snap groove.



(a) (b)

Figure 12. Representative views of CAD models of the (a) first- and (b) second-round prototype.

Table 2 shows the final dimensions and feature type for caps for fire-polished and scribe-cut glass tube ends. A prototype capsule from a glass tube with a glass vial with a scribe-cut and a fire-polish finish and their corresponding caps were produced. A 25G needle (0.515 mm OD) can be inserted. The push-fit is stable and resists pulling, and the assembled capsule is water-tight (Figure 13).



(a) (b) (c)

Figure 13. Capsule prototypes. (a) a glass tube with fire-polished end on the left and scribe-cut on the right; (b) the two caps optimized for each cut, inserted into the tube on each end; (c) an assembled capsule prototype filled with water.

3.3. Discussion and summary

The unique nature of tomographic VAM necessitates a custom enclosure to house biomaterials that will be patterned and perfused. As such, capsule devices that allow for perfusion were developed for the CAL system and its microscale counterpart. Their designs have informed the availability of prototyping methods and materials, the necessity for fluid containment and precise alignment, as well as ease of use and assembly. In a prototype stage, soft hydrogels were successfully patterned into perfusable vascular structures.

The limitations of this work include:

Choice of tube materials. Glass provides high precision dimensions and tight tolerance in processing but is more expensive to source and process. Glass cutting and polishing often requires a glass shop which increases the cost of labor significantly. On the other hand, plastic is more affordable but often compromised by poor dimensional tolerances and straightness—issues particularly pronounced in tubes stored in coils—as well as potential light scattering and autofluorescence during patterning and imaging.

Compatibility with microscopy. The non-planar design and refractive index mismatch between the capsule and biomaterials require special consideration in microscopy. Imaging of previously reported VAM-printed samples has typically been done with the samples outside of their containers. Preliminary imaging studies carried out with these new CAL capsules show that the center of the CAL capsule can be imaged using long-working-distance air or water objectives. Nonetheless, further examination is needed to understand the extent of image distortion and to explore potential RI-matching strategies.

Alignment. Misalignment with the projection's vertical (defined by a nonzero angle between the capsule's long axis and the projection vertical) and misalignment between capsule connectors (a nonzero azimuthal angle between two connectors) impacts the positioning of the printed construct within the capsule and perfusion ability of the final product. The coupling mechanism between the capsule and CAL's rotation stage must be carefully designed since misalignment can arise from between any pair of mating parts and can propagate downstream.

Chapter 4

Bioprinted constructs and characterizations

Previously, it was highlighted that CAL offers two distinct benefits: printing objects without requiring support structures and maintaining the integrity of highly fragile objects during printing, irrespective of their flexibility or deformability. This section will empirically showcase these advantages by demonstrating the printability of perfusable structures in hydrogels, printed with CAL and microCAL systems. This chapter will also describe efforts made toward endothelializing vascular hydrogel structures.

4.1. Biomaterial preparation

4.1.1. Hydrogels

Gelatin is a macromolecule derived from hydrolyzing collagen, the most abundant extracellular matrix (ECM) component in native mammalian tissues. It is a single-stranded biopolymer containing lysine groups, presenting free amines that can be chemically modified [98], [99]. A methacrylate-functionalized gelatin, gelatin methacrylate (Gel-MA), has been developed to undergo free radical polymerization via the methacrylate group. Like collagen and gelatin, a dilute aqueous solution of Gel-MA crosslinks reversibly at a threshold temperature in the room temperature range. This is useful for supporting and maintaining the structure during patterning.

Photoinitiator lithium phenyl-2,4,6-trimethylbenzoylphosphinate (CAS no. 85073-19-4, Sigma Aldrich) was used at a concentration of 0.2 w/v % of the solution. It was slowly mixed with sterile Dulbecco's Phosphate Buffered Saline (DPBS, Gibco, Rockville, MD, USA) at 45 °C, before being sterilized by passing through a 0.2 μm pore-size filter. The solution was then added to lyophilized Gel-MA (Cellink) before slow, overnight mixing at 45 °C. In the case requiring PEG-DA composites as a comparison, 7.5 w/v % PEG-DA-700 (average molecular weight 700) (CAS no. 26570-48-9, Sigma Aldrich) was also added. Afterward, the hydrogel precursor was aliquoted into vials or dispensed into capsule devices and then cooled to 4°C to trigger thermal crosslinking. Thermal crosslinking before photocrosslinking prevents print sinking; moreover, it was also shown to enhance the mechanical stiffness of the final print [88].

Printing with low-viscosity resins such as hydrogels requires consideration of diffusing oxygen, a strong quencher of free radicals. The solubility of oxygen in water is highly temperature-dependent, with lower temperatures allowing for higher steady-state oxygen concentrations. When cooling the Gel-MA from a mixing temperature of 37–45 °C, oxygen diffuses inwards from the liquid-air interface at the top of the vial. This process can take two to three days to evenly penetrate the 3 cm depth of the vials and achieve a uniform distribution. To ensure a consistent oxygen concentration throughout the Gel-MA and for the sake of time, the gel was used immediately after thermal gelation, which restricts the oxygen diffusion into the material.

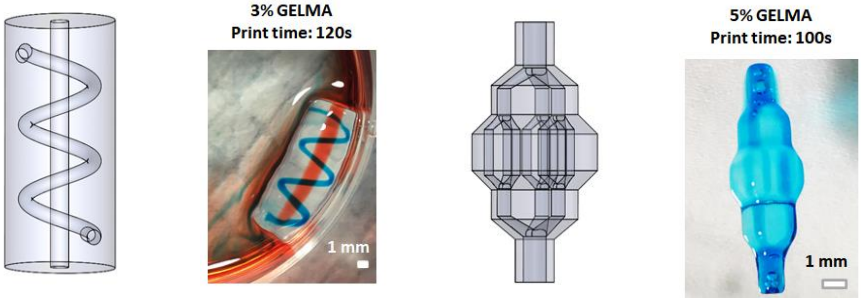
4.1.2. Cell culture and preparation of cell-laden hydrogel precursors

Human microvascular endothelial cells (HMEC-1s, ATCC CRL-3243, American Type Culture Collection) were cultured in MCDB 131 medium (Thermo-Fisher Scientific) supplemented with 10% fetal bovine serum, 10 ng/mL endothelial growth factor (EGF, Thermo-Fisher Scientific), and 1% penicillin/streptomycin at 37 °C in a humidified 5% CO2 atmosphere. Human umbilical vein endothelial cells (HUVECs, ATCC CRL-1730, American Type Culture Collection) were cultured in α-MEM containing 10% FBS, 10 ng/mL TGFb1, 1% glutamine, and 1% penicillin-streptomycin, and EBM-2 supplemented with EGM-2 BulletKit and 10% FBS, respectively. All subcultures were passaged at 80–90% confluence. The cells were recovered at this stage after detachment from the culture plates using fresh 0.05% trypsin-EDTA (1X) solution (Gibco) and then either passaged or used in the experiments.

In experiments requiring cell-embedded hydrogels, cell suspension of density 1 million/mL was mixed with hydrogel precursor then refrigerated and thermally gelled at 4 °C. Due to the sedimentation of cells, either the mixture needs to be gently stirred during the cooling phase or the cooling should be short enough to prevent the cells from settling at the vial's bottom. Viability assay was performed using LIVE/DEAD® Viability/Cytotoxicity Kit (Thermo Fisher) following the manufacturer's protocol. For visualization purposes, fluorescent staining on the actin cytoskeleton and cell nucleus was performed with Alexa Fluor 594 phalloidin and DAPI, respectively. Brightfield and fluorescence imaging was done under an inverted microscope (Echo Revolve).

4.2. CAL-printed perfusable structures

4.2.1. Acellular prints



(a) (b) (c) (d)

Figure 14. Printing multivascular non-axisymmetric perfusable structures using CAL. (a) CAD model of a multi-vascular architecture featuring both straight and spiral channels; (b) the structure in (a) printed from 3 v/v % Gel-MA in 120 s; (c) CAD model of a triple-level branched architecture; (d) the structure in (c) printed from 5 v/v % Gel-MA in 100 s. Image credit for (a) and (c): Hossein Heidari.

Using the CAL printer described in Chapter 2, existing in-house designs of multivascular structures such as a spiral around a straight tube (Figure 14b) and a trifurcated vascular structure (Figure 14d) were printed in 3 v/v % and 5 v/v % Gel-MA respectively after exposure times of 120 and 100 s.

The shadowgraph imaging system on CAL has low sensitivity to minor refractive index changes, which made it challenging to observe the emergence of the object, particularly with low Gel-MA concentrations. Therefore, for each set of geometry and hydrogel used, the timing of print termination had to be determined from trial and error, lowering the efficiency and throughput of the prints.

4.2.2. Cellular prints

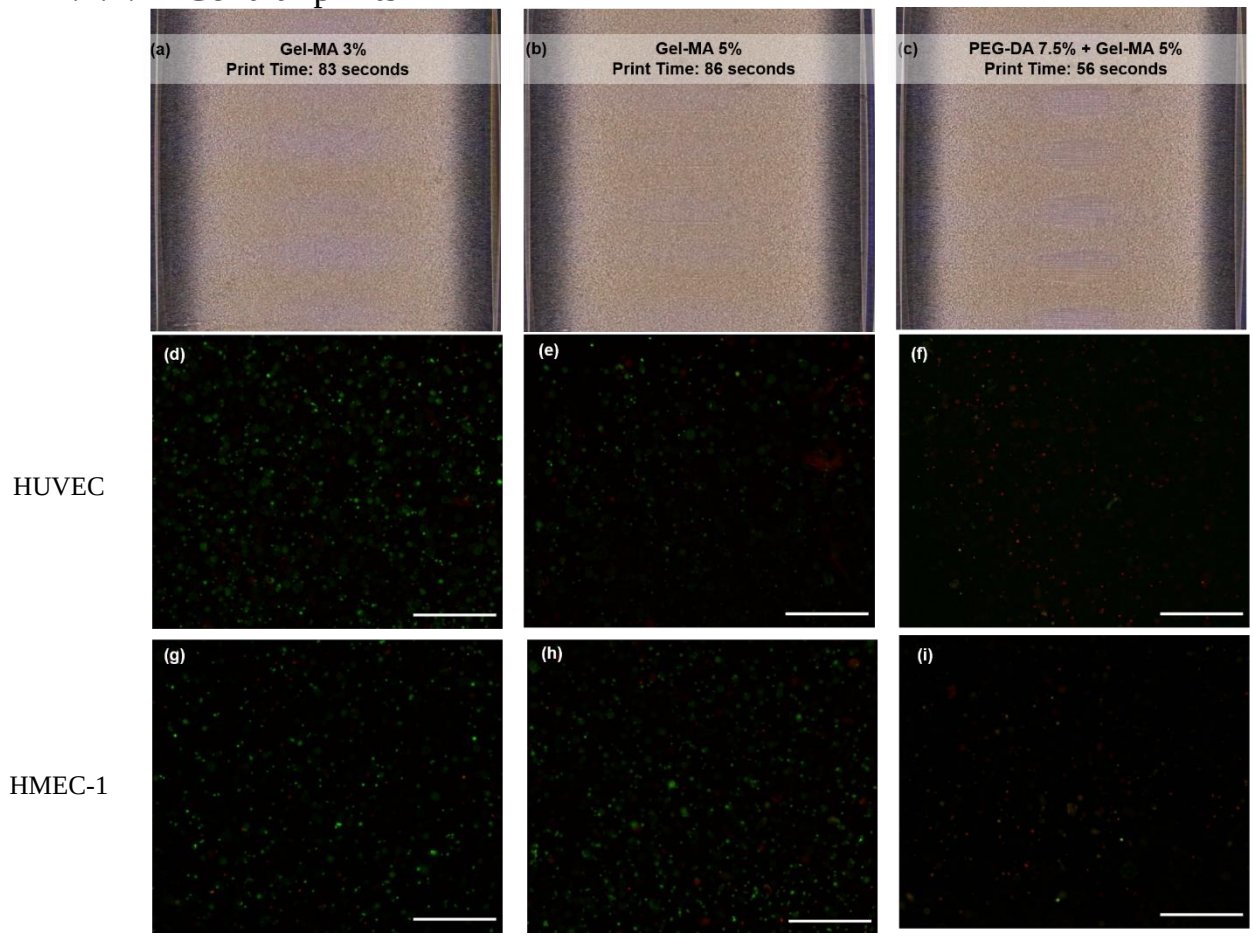


Figure 15. Printing cell-embedded cylindrical disks with CAL. (a)–(c): a vertical stack of disks printed within a composite hydrogel containing 3 w/v % Gel-MA (a), 5 w/v % Gel-MA (b), and 7.5 w/v % PEG-DA-700 and 5 w/v % Gel-MA hydrogel (c). (d)–(f): fluorescence images of disks printed in materials in (a)–(c) cellularized with HUVEC at 0h and stained with calcein-AM (green) and ethidium homodimer-1 (red) at 24h. (g)–(i): fluorescence images of disks printed in materials in (a)–(c) cellularized with HMEC-1 at 0h and stained with calcein-AM (green) and ethidium homodimer-1 (red) at 24h. Scale bars: 200μm. Experiment and image credit: Hossein Heidari.

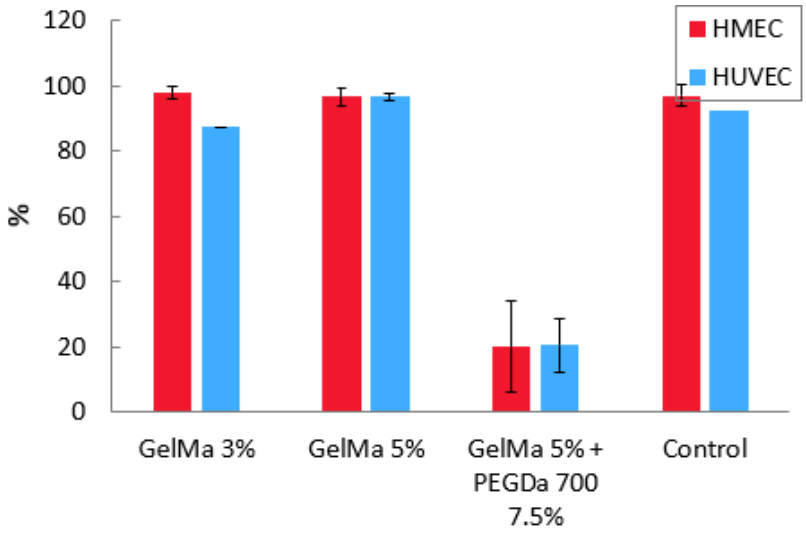


Figure 16. HMEC-1 and HUVEC viability 24h after printing embedded in 3 w/v % Gel-MA, 5 w/v % Gel-MA and 5 w/v % Gel-MA + 7.5 w/v % PEG-DA-700, respectively. Control: petri dish culture with the same media and duration. Experiment credit: Hossein Heidari.

As described in ection 4.1.1, to produce the cell-embedded prints, HMEC-1 or HUVEC were uniformly dispensed within the hydrogel precursors, then rapidly cooled and moved to the printer. To explore the potential for vascular network formation in various gel compositions, stacks of cylindrical disks were printed using three different hydrogels: 3 w/v % Gel-MA, 5 w/v % Gel-MA and a composite of 7.5 w/v % PEG-DA-700 and 5 w/v % Gel-MA (Figure 15). Following the printing process, the disks were incubated at 37 °C while the uncured mixture surrounding the disks was collected and incubated separately as control. 24 h after incubation, a subset of disks were sampled for a terminal live-dead assay (Section 4.1.1, Figure 16), where the rest were kept in incubation for a total of 11 days. The proliferation, colonization, and vascularization capabilities of the embedded cells within the hydrogel environment were observed throughout the incubation (Figure 17).

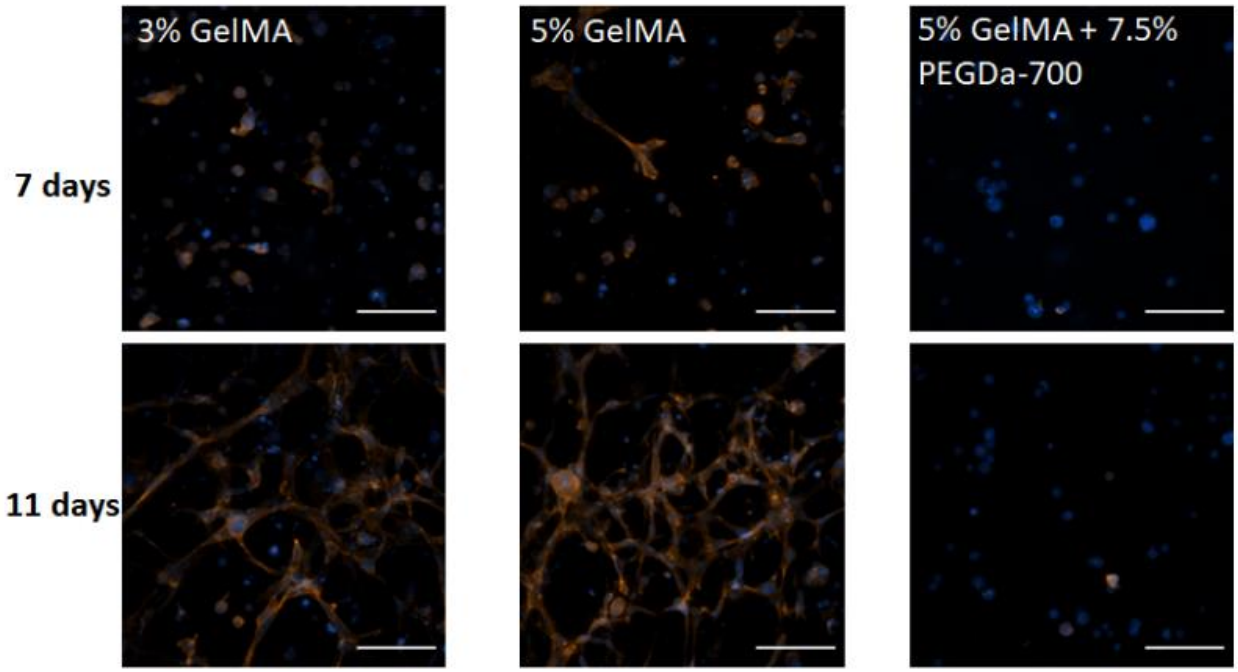


Figure 17. Development of HMEC-1 networks within the hydrogel prints from 3 w/v % Gel-MA, 5 w/v % Gel-MA and 5 w/v % Gel-MA + 7.5 w/v % PEG-DA-700, imaged after 7 and 11 days of culture. Orange: Alexa Fluor 594 phalloidin, blue: DAPI. Scale bars: 200 µm. Experiment and image credit: Hossein Heidari

Both gel compositions had equal cell concentrations. Initially, during the first 24 h post-printing, there were no visible differences. After 11 days, the 3% Gel-MA prints developed extensive branched capillary networks, covering over 500 µm, as illustrated in Figure 17. These networks were exclusive to the 3 w/v % Gel-MA composition; neither the Gel-MA + PEG-DA composites nor the higher concentration 5 w/v % Gel-MA prints showed similar growth. The viability of the disk 24h after printing was also quantified (Figure 16), where cells in the GEL-MA + PEG-DA composite were the only group that failed to host live cells. The cells in the sample also failed to proliferate in the subsequent incubation.

These findings underscore the importance of matrix stiffness as well as the amount of cell adhesion proteins in influencing the development of endothelial cell networks in the gels. Factors like cell motility, and the capability to extend actin structures and interact with neighboring cells are crucial in forming a confluent tissue structure.

4.3. microCAL-printed perfusable structure

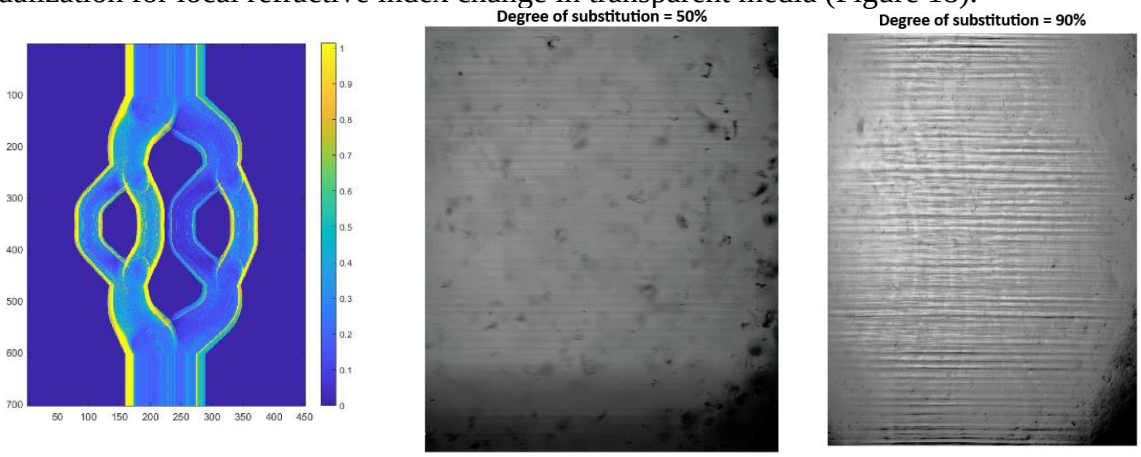
The CAL-printed perfusable structure in capsule devices is described in Section 3.1.3. However, the size scale of physiological capillary vasculature necessitates microscale printing to replicate the geometry and the associated fluid dynamics. The development of microCAL illustrated in Section 2.2 enables bioprinting microscale structures by a small étendue optomechanical system. Here, bioprinting with microCAL is explored using Gel-MA, where the effects of degree of substitution (DS) and radical inhibitor on the empirical observation of the prints were explored and discussed.

4.3.1. Choice of the degree of substitution and effect of radical inhibitor in Gel-MA

As introduced in Section 4.1.1, Gel-MA is photocrosslinkable gelatin derivatives by reacting gelatin with methacrylic anhydride [100]. During the process, amino and hydroxyl groups are substituted by methacrylate groups; the degree of substitution (DS), defined by the ratio between functionalized to originally available amino groups, can be measured by ^{1}H NMR spectroscopy or fluorescent fluoraldehyde assay [99], [101].

Since the methacrylate group actively participates in the radical polymerization of Gel-MA, DS is of critical importance to the crosslinking density and thus the physical and biochemical properties of the resulting hydrogels. For instance, one can adjust the compressive modulus of Gel-MA by altering the extent of methacryloyl substitution [102]. It is also shown that the pore sizes in Gel-MA hydrogel can be tuned by changing the degree of methacryloyl substitution [103], [104].

Here, Gel-MA of 50% (Cellink) and 90% (Advanced Biomatrix) DS have been used separately as hydrogel precursors for the microCAL-printed perfusable structures. It is expected that under the same spatial light dose, Gel-MA of higher DS would display higher local crosslinking thus higher local stiffness and change of refractive index. 90% DS Gel-MA was empirically chosen for the experiments forward due to its higher contrast under the same light dose in shadowgraph images, a visualization for local refractive index change in transparent media (Figure 18).



(a) (b) (c)

Figure 18 (a) light projection of a trifurcated structure, color bar: normalized light dose; shadowgraph of (b) 50% and (c) 90% DS Gel-MA after printing the trifurcated structure under the same exposure times. The structure overcured in both instances but (c) is more visible on the shadowgraph.

In VAM, it is also crucial to establish a specific degree of conversion threshold to attain exceptional print accuracy. This threshold is significant because it enables the precise definition of the printed object's boundaries and facilitates the easy removal of the object from the surrounding exposed photopolymer. Nonetheless, some parts of the photopolymer around the target area will inevitably be exposed. Consequently, it is essential to minimize the degree of conversion of the material in the surrounding region.

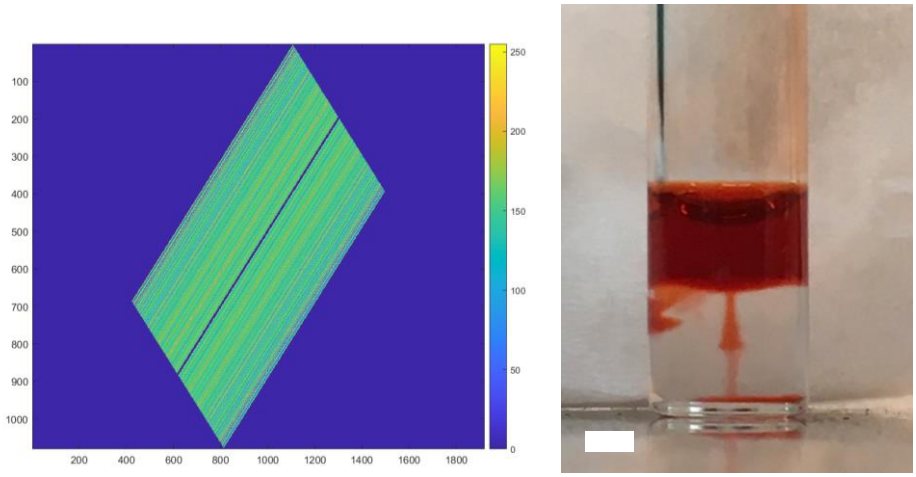
In our group's earlier research focusing on silica glass nanocomposites, it was found that incorporating nitroxide radical inhibitors, specifically TEMPO, achieves two key effects. Firstly,

it extends the induction period, which is the time during which the conversion process in the resin is delayed or inhibited by radical scavenger species. Moreover, the presence of TEMPO significantly improves the lithographic contrast of the resin. This enhancement is crucial for better modulation of features during the microCAL process [77]. Increasing the concentration of TEMPO was observed to reduce the degree of conversion both in the regions surrounding the printed object and within the internal voids and interstitial spaces of the object itself.

In experiments, it was noted that prints with microscale multivascular structures displayed low contrast, despite using Gel-MA with a high DS of 90%. To improve this, various concentrations of TEMPO, ranging from 0 mM to 1 mM, were tested to enhance printability. Ultimately, a linear channel was successfully printed in 52 seconds using a mixture of 5 w/v % Gel-MA with 90% DS, 0.33 mM TEMPO, and 6.78 mM LAP (Figure 19). The channel's diameter measured 100 μm at projection, and its void state (indicating no overcuring) was confirmed by flowing red food dye through it for visualization. The cone-geometry seen in Figure 19 is a defect resulting from forceful perfusion when the channel was manually perfused. Some gelled material may have been fragmented from the side wall under the shear and clogged the channel at the middle (where the base of the cone geometry is), rendering the dye less permeable to the lower portion of the channel and resulting in the lighter red color observed. This highlights the delicate nature of low-concentration Gel-MA and the importance of low-shear stress in perfusing such prints from a mechanical standpoint.

Although these prints could be somewhat discerned using shadowgraph imaging, they often suffered from overcuring by the time they were visible. A systematic way to narrow down the viable print time is by bisection method (also called binary search), where the time interval between two known print times with distinct results (in this context "overcured" and "undercured", defined as obstructed and unformed channels, respectively) is bisected repeatedly. Since "overcured" and "undercured" states transition continuously, the interval containing the change of result must contain a viable print time (Table 3).

Consequently, the window of ideal printing duration is found to be bound between 50 and 55 s, with print time at 52s producing a viable channel print. This finding underscores the need for more sensitive visualization techniques than shadowgraphy, such as Optical Scattering Tomography [105], tomographic color schlieren imaging [87], [106], and tomographic fluorescence imaging (Chapter 5), to optimize the printing process.



(a) (b)

Figure 19. Printing linear channel with microCAL. (a) Light projection of a linear channel rotated 45° from vertical to accommodate for the optomechanical configuration in microCAL. Colorbar: gray value of projector pixel; (b) photograph of the channel printed from 5 w/v % 90% DS Gel-MA + 0.33mM TEMPO + 6.78 mM LAP. Scale bar: 300 µm.

Table 3. Testing print times with bisection method to obtain the optimal print time for a perfusable linear channel from 5 w/v % 90% DS Gel-MA + 0.33mM TEMPO + 6.78 mM LAP. Only print 5 resulted in a perfusable structure.

Print number/bisection step	Print time (s)	Curing
1	55	Overcured
2	35	Undercured
3	45	Undercured
4	50	Undercured
5	52	Optimally cured

4.4. Cell seeding study

Chapter 1 emphasizes the critical role of vascularization in building fully functional tissues *in vitro*. Seeding of endothelial cells (ECs) within the vasculature can recapitulate the barrier function and vascular physiology of native blood vessels. For effective vascularization of a tissue scaffold built with CAL, knowledge of the optimal cell seeding conditions for a given patterned vascular network is essential. This section describes the development of EC seeding and controlled perfusion protocols intended to be applied for CAL capsule devices.

4.4.1. Planar seeding

Section 4.2.2 describes the cell-embedded bioprinted structures. To investigate the performance of the bioprinted materials for EC seeding, the same gel formula used for the bioprints was tested for EC surface growth and proliferation.

Planar Gel-MA surfaces were created in wells by flood-curing 3 w/v % or 5 w/v % Gel-MA in low-volume wells on a cover-slip (Ibidi µ-Slide 15 Well 3D). HMEC-1 and HUVEC cells before passage 8 were seeded at a density of 2000 cells/mm^2 for 1h before being washed gently with culture media and cultured until confluence (if applicable). During the culture period, samples were inspected routinely with brightfield imaging (Echo Revolve, EVOS XL Core) for proliferation and morphology. Terminal brightfield imaging was carried out after washing with

DPBS. Terminal fluorescence staining was carried out by first fixing the cells with 4 v/v % paraformaldehyde in DPBS pH 7.4 for 10 min at room temperature, before washing and permeabilization with 0.1 v/v % Triton X-100 in DPBS, followed by washing with DPBS. Alexa Fluor 594 phalloidin was diluted to a working concentration per the manufacturer's recommendation and incubated with the samples for 20 min. After washing the samples three times with DPBS, the samples were finally incubated with diluted DAPI in DPBS for 10 min followed by final washings and observation under a fluorescence microscope (Echo Revolve).

To enhance EC attachment to the channels, certain gelatin samples were crosslinked with Gel-MA with enzyme transglutaminase (TG). A solution of food-grade TG at a concentration of 60 mg/mL was prepared in DPBS. The solution was syringe-filtered with a pore size of 0.22µm. The filtration speed was controlled at a rate of one liquid drop per second or less, to prevent any loss of protein through the filtration process. A solution of 2 w/v % gelatin in DPBS was prepared separately and autoclaved. A final 0.2 w/v % TG and 1 w/v % gelatin solution in DPBS was made and incubated with the cured gel for 1 hour at 37 °C before washing and cell seeding.

At Gel-MA concentrations as low as 3 w/v % and 5 w/v %, both HMEC-1 and HUVEC cells displayed poor adhesion as they failed to spread and exhibit the typical "cobblestone" monolayer pattern. HMEC-1 cells even aggregated and showed a spheroid-like morphology in the case of 3 w/v % Gel-MA (Figure 20). This suggests the ECM ligands may be insufficient for EC attachment so that they tend to aggregate rather than spread out.

After surface treatment with 1 w/v % gelatin, more HMEC-1 spreaded and showed EC-like morphology (Figure 21 and Figure 22). This supports the hypothesis that more cell-binding/digestible peptides are required for EC binding and proliferation on 3 and 5 w/v % Gel-MA.

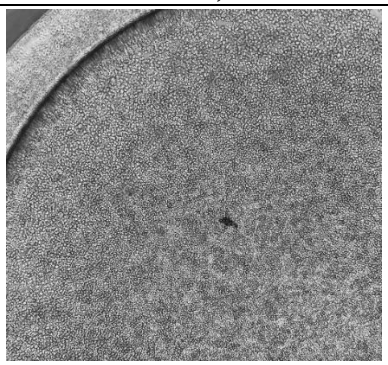
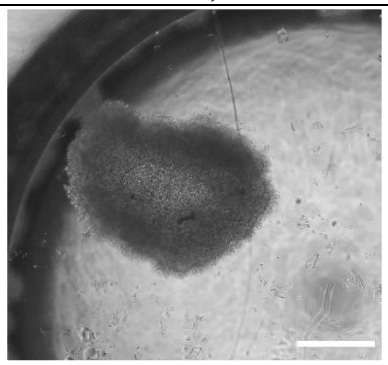
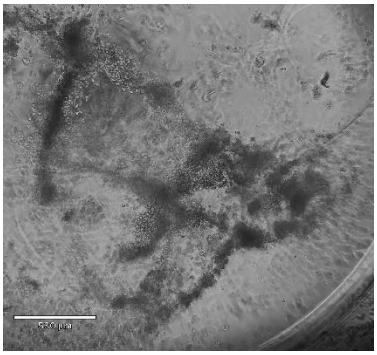
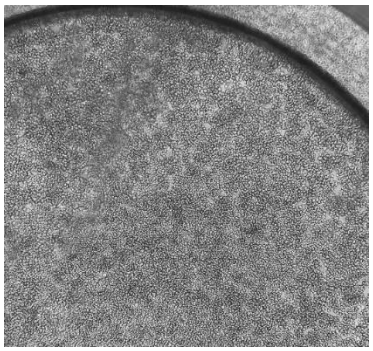
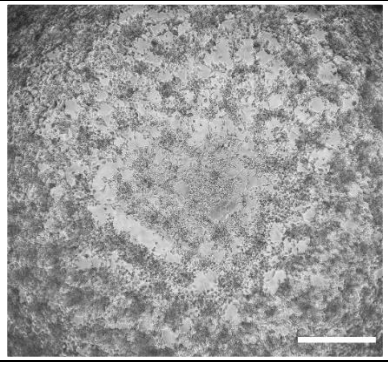
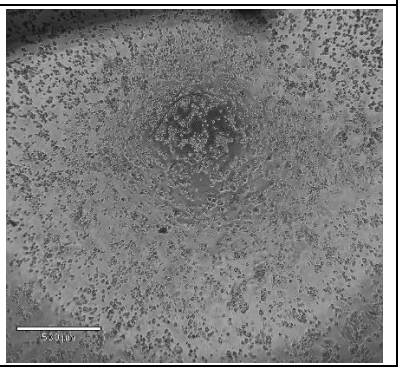
	HUVEC, 0 h	HUVEC, 36 h	HMEC-1, 12 h
3 w/v % Gel-MA			
5 w/v % Gel-MA			

Figure 20. Cell adhesion on Gel-MA without surface treatment. Brightfield images of HUVEC at 0 h and 36 h of culture, and HMEC-1 at 12 h of culture on 3 w/v % and 5 w/v % Gel-MA respectively. The dark regions in the HMEC-1 3 w/v % Gel-MA sample were caused by gel ruptured during washing. Scale bars: 500 µm (first two columns) and 530 µm (last column).

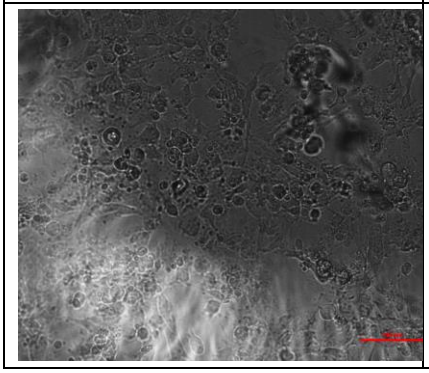
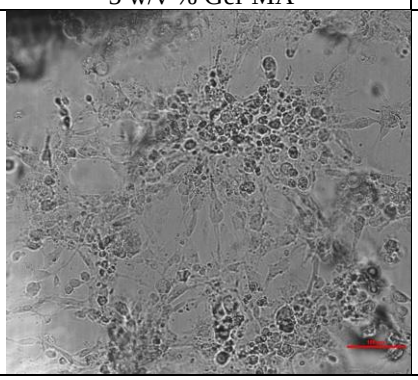
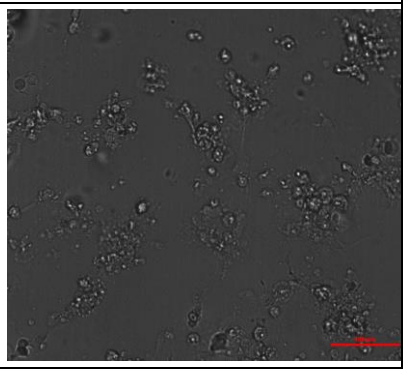
1 w/v % gelatin		No gelatin
3 w/v % Gel-MA	5 w/v % Gel-MA	3 w/v % Gel-MA
		

Figure 21. HMEC-1 adhesion on Gel-MA improved after surface treatment with gelatin. Brightfield images of HMEC-1 at 36 h of culture on 1% gelatin-treated 3 w/v % and 5 w/v % Gel-MA, and on non-treated 3 w/v % Gel-MA, respectively. Scale bars: 100µm.

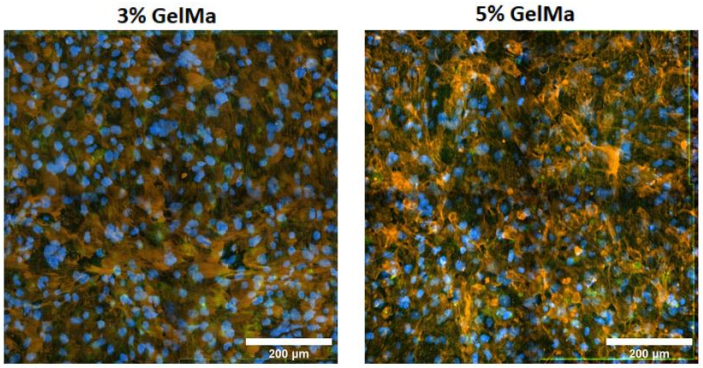


Figure 22. Confluent HMEC-1 on planar Gel-MA of different concentrations, both coated with 1% gelatin. Blue: DAPI, orange: Alexa Fluor 594 phalloidin. Seeding density: 2000 cell/mm^2, passage number at seeding: 8. Scale bars: 200µm.

4.4.2. Cell seeding chip—motivation and design

Although compatible with the CAL printer, the perfusable device described in Chapter 3 requires significant reagent volume compared to common organ-on-chip devices and is not of a standard configuration for microscopy. Therefore, a low-volume, planar housing of prefabricated hydrogel vasculature has been developed for cell seeding optimization, as well as a repeatable cell seeding setup that can run multiple samples at a time.

A chip-like cell-seeding device was developed to capture the characteristics of the CAL-compatible perfusable device described in Chapter 3. Like the perfusable device, it is 3D-printed from Formlabs Surgical Guide resin, which provides a rigid boundary for the cured hydrogel. It consists of a central gel chamber, two gel ports, and two needle guides. Acrylate-functionalized glass coverslips are glued to the gel chamber on the flat sides to allow adhesion with hydrogel, viewing, and microscopy. The gel ports and needle guides provide inlets for hydrogel. A hydrogel channel is cast in the chip with a needle as a simplified setup for CAL-printed channels.

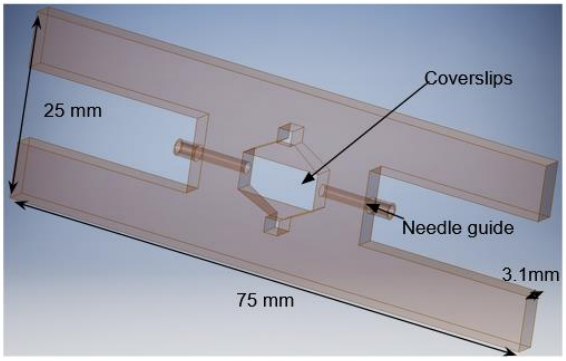




Figure 23. (Top) Schematic of cell seeding chip showing terminology and key dimensions. (Bottom) An overview of the workflow for chip assembly, seeding and perfusion.

4.4.3. Chip assembly and sterilization

Square glass coverslips (#1.5, 22×22 mm) are sonicated in pure ethanol twice for 5 min each, replacing ethanol each time. Then, the coverslips are sonicated in DI water for 5 min. A solution of 5 v/v % 3-(Trimethoxysilyl)propyl methacrylate (TMSPMA) (Sigma Aldrich) in toluene was prepared under a fume hood where the coverslips were soaked overnight at 60 °C. The coverslips were then rinsed twice in ethanol then twice in DI water, before being dried in an 80 °C oven.

The chips were printed with Formlabs Surgical Guide Resin. The support structure was removed and the surface was smoothed by sanding. Small amounts of UV-curable adhesive (Loctite AA 3961) were dispensed around the gel chamber window before two coverslips were affixed onto the chip from each side. The assembled chips were then placed in a warmed-up UV curing chamber (Loctite) for 30s. Afterward, the chips were sterilized by soaking with 70 v/v % ethanol for 5 min, before being dried in air or an oven.

4.4.4. Gel casting and functionalization

The chips and 5 w/v % Gel-MA (Cellink) + 0.2 w/v % LAP (Sigma Aldrich) solution were pre-warmed to 37°C to prevent the formation of air bubbles. To prevent adhesion to the gel, 18G needles (BD) were coated in 0.1 w/v % pluronic-F127 by dipping into the solution and dried before gel casting. In a laminar flow hood, the chips were held and tilted on their longer side while 0.4–0.45 mL of the gel solution was pipetted into the chip from the lower gel port to fill the entire gel chamber. A pre-treated needle was then inserted across the gel chamber from a needle port. The chips were then cooled to 4 °C in the dark for 10 min. Subsequently, the chips were flood-cured with a 405 nm LED light source for 5 min. The needles were slowly twisted and retracted from the chips before the newly casted channels were gently washed with DPBS.

To enhance EC attachment to the channels, a 0.2 w/v % TG and 1 w/v % gelatin solution in DPBS was made as outlined in Section 4.4.1 and injected into the gel channel. The gel channels were incubated at 37°C for a minimum duration of 1 h. The chips were then perfused with DPBS for at least 12 h, to clear any unreacted gelatin or TG from the channels.

4.4.5. Testing cell seeding conditions on the chip

HUVEC suspension of 6.3 million cells/mL in culture media was prepared and warmed to 37°C. The syringe was filled with sufficient cell suspension volume to occupy each channel, with an additional 200 μL/chip to account for dead volume in the inlets and outlets. The suspension was mixed in the syringe by holding the syringe tip-up and gently drawing the syringe plunger up and down. The cell suspension was injected into each cast channel on the chips until the channels were filled. The chips were then closed by plugging short flexible tubing (1/16″ inner diameter) with plugs (Cole Parmer EW-51519-38) on both needle guides.

The seeding times and conditions (with or without rotation) screened are listed in Table 4. In the seeding experiment requiring rotation, multiple chips were rotated synchronously on a stepper motor device [107]. A custom 3D-printed chip holder is connected to a stepper motor which is programmed by an Arduino microcontroller to rotate at a constant period. After seeding, the

channels were washed with DPBS and then imaged under a bright field microscope for HUVEC adhesion.

Table 4. List of seeding times and rotation screened, and the observed HUVEC adhesion in each case.

Time/rotation period	Chip rotation (Y/N)	HUVEC adhesion (Y/N)
15 min	N	N
30 min	N	N
1 h	N	Y
2 h	N	Y
2 h	Y	N

In static conditions (no chip rotation), it is found that 1 h seeding is sufficient for HUVEC adhesion on 5 w/v % Gel-MA functionalized with 1 w/v % gelatin (Figure 24), with cells were able to spread into "cobblestone" morphology, an indication of confluent endothelial layer [108], [109]. This is not surprising given the similar result shown in section 4.1.1. HUVECs also remained after the washing step although the morphology has become rounded. A hypothesis for this observation is the depleted oxygen and nutrients in the culture media incubated with the HUVECs during the incubation period. HUVECs failed to attach to the Gel-MA channels after 2 h rotation, suggesting the need for either slower rotation or stronger binding between the functionalized surface and HUVECs.

A major challenge of 3D bioprinting is the efficient endothelialization for tissue vascularization. For this, various strategies have been developed to date such as embedding EC in print material pre-print [110], [111], EC-containing sacrificial template [112], and seeding by perfusing concentrated cell suspension followed by rotation [107], [113]. Inspired by the work of Kinstlinger et al. [107], the cell seeding chip reported here presents a tool for rapid, parallelized testing of multiple seeding and perfusion conditions in simplified geometries (such as a linear channel) bypassing the bioprinting stage. In addition, the chip can be fabricated on a commercial 3D printer in scale, requiring a lower skill level to learn and operate.

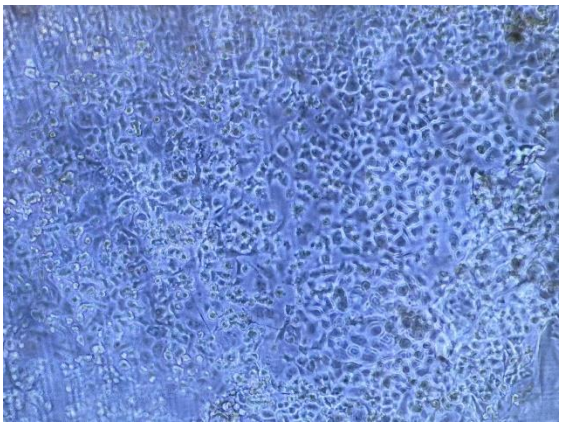


Figure 24. Endothelial cells (HUVEC) adhering to a substrate consisting of 5 w/v % Gel-MA that has been functionalized with 1 w/v % gelatin, which exhibit a cobble-stone-like morphology.

4.5. Summary

This chapter successfully demonstrates the advantages of CAL and microCAL systems in printing soft and complex structures in Gel-MA, namely the absence of support structures and the abililty to pattern soft, fragile hydrogels. It also examines different gel compositions and their impact on HMEC-1 and HUVEC viability, proliferation, and the formation of vascular networks within the gel. The contrast in viabilities in hydrogels of different compositions and stiffnesses confirms the significance of mechanical and biochemical properties in determining the fate of endothelial cells embedded in the gels.

In addition, a study on cell seeding is presented, focusing on the optimal conditions for seeding HUVECs on functionalized Gel-MA, on both petri dish and in a chip-like cell seeding device developed for this purpose. The contrast of cell proliferation in the bulk and on the surface of 3 w/v % Gel-MA highlights the different growth behaviors and mechanical/biochemical needs in different contact modes. Unlike *in vivo* angiogenesis which takes place within the bulk of tissue, cells do not have full contact with the hydrogel during the seeding of pre-patterned lumens; thus, they require additional treatment to the hydrogel surface for enhanced adhesion. As an engineering measure, the surface treatment with gelatin to 3 w/v % and 5 w/v % Gel-MA verifies that an additional amount of surface ligands is required on the hydrogel to provide the correct mechanical and biochemical signals for endothelial growth.

The fact that tomographic VAM relies on volumetric accumulation of light limits the use of CAL to patterning resins transparent/non-scattering to the patterning light. However, resins that are opaque in visible wavelengths e.g. high-density-cell-embedded hydrogels and bone-like structures/bioceramics [114] are also in significant demand for tissue engineering applications. Strategies to incorporate such bioresins into CAL's material library may include refractive-index matching [33], [111], [115], tissue maturation post-print [32], [116], and post-print chemical [114], enzymatic or thermal [77], [117] crosslinking.

On the other hand, Gel-MA resins' narrow optimal print time and its sensitivity to various print parameters, such as the degree of substitution and the use of radical inhibitors as explored here, highlight the challenges in achieving precise print accuracy and the need for sensitive visualization techniques. Current *in situ* monitoring methods in tomographic VAM mainly focus on analyzing optical changes during printing and measuring material conversion by tracking refractive index changes or scattering density. This suggests a gap in existing monitoring techniques in terms of comprehensively understanding and controlling the tomographic VAM process.

As such, the next chapter discusses the physical and chemical changes that arise from a tomographic VAM process, proposes a new print visualization method based on heat and print state, and reports an implementation of such a system utilizing a fluorescent dye.

Chapter 5

Probing temperature and degree-of-conversion states via tomographic fluorescence imaging

This chapter introduces the second part of this thesis research, a tomographic fluorescence imaging technique to detect the spatiotemporal evolution of temperature and degree of conversion during volumetric printing.

5.1. Introduction and Motivation

As outlined in Section 4.5, challenges from volumetric hydrogel printing motivate metrology methods beyond refractive index or scattering tracking. In general, photopolymerization brings multiple physical and chemical changes in the reaction volume, such as heat generation, polymer crosslinking, a heightened degree of conversion (DOC) and local density, rheological change, mass transport, as well as consumption and creation of polymerization-specific products [118], [119]. In particular, temperature plays an important role in photopolymerization due to its potential to auto-accelerate the polymerization reaction, trigger convection which leads to part floating [120], [121], [122], cause optical aberrations, and alter the mechanical properties of the final product [123]. Heating also introduces residual stress in the print as it cools down, due to a mismatch in thermal expansion coefficients between polymer domains [124]. As for polymers with low glass transition temperatures (e.g. thermally reversible hydrogels), heat generated during the process could also lead to state transition and in-print issues such as part deformation and sinking. In the case of cell-embedded biomaterials, the excess local heat generated could introduce cell stress and impact cell viability [89].

Heat generation has been acknowledged in vat-based AM as one of the fabrication speed limiters [125]. Several studies have been devoted to examining the relationship between process temperature and outcome such as mechanical, rheological, and dimensional properties of the print [126], [127], [128], and interface adhesion [125]. To address the significance of temperature in the vat AM printing process, infrared (IR) thermometry has been applied for CLIP-based processes [125], [129], [130]. However, it cannot be easily applied in volumetric measurements as it faces challenges such as limited transmission, material-dependent absorption peaks, and high background signals emitted by other objects relative to the signal from the reaction. Thermal imaging using visible light from blackbody radiation, as used in reactive sintering [131], does not apply to VAM due to a much lower reaction temperature.

The tomographic nature of VAM can be harnessed for volumetric thermometry. In clinical practice, X-ray CT thermometry has been used as a non-invasive technique for monitoring tissue temperature during thermal ablation procedures for destroying tissues such as tumors [132], [133]. It is based on the fact that the average X-ray attenuation (in terms of CT numbers) is influenced by the electronic density of the tissue and changes in physical density due to thermal expansion [134], [135]. The temperature change can be correlated to changes in CT number linearly for both artificial phantoms and bovine liver undergoing radiofrequency ablation and laser-induced thermotherapy [136], [137], [138].

Currently, methods for *in situ* monitoring in volumetric AM primarily focus on optical effects arising during printing. Color schlieren tomography (CST) [106], [87] is designed to reconstruct local refractive index changes and quantify local material conversion through conversion-index relationships. On the other hand, optical scattering tomography (OST) [105], [139] infers material conversion from reconstructed scattering density. While both spatiotemporally resolved techniques have the potential to provide process control feedback from a conversion perspective, their current development has not addressed the exothermic nature of the process.

Fluorescence thermometry, also known as luminescence molecular thermometry, offers a viable alternative. This technique has been successfully employed to monitor temperatures in small-scale and biological environments [140]. It provides a variety of readouts including fluorescence intensity, fluorescence lifetime, and absorption/emission spectrum, offering resolution down to sub-degree Celsius. Yet, these measurements are commonly made in 2D. Although 3D measurements have been made with confocal microscopy, tomographic measurements, which enable larger (cm-scale) isotropic measurements, have not been performed.

In the following sections, the dependence of rhodamine B (RhB) on the surrounding temperature and DOC is exploited to infer their possible values during a print. RhB is a cost-effective, widely available, and well-studied fluorophore. It is highly soluble in the resins used in this study at the concerned concentration (5 μM). RhB's sensitivity to the viscosity and temperature of the environment has been demonstrated previously [141], [142], [143]. Here, tomographic fluorescence imaging was employed to measure spatiotemporally the intensity of these luminescent molecular thermometers, providing a relationship between temperature and DOC (expressed in terms of absorbed dose) at various points in space and time. With *a priori* information on one of the quantities, this relationship allows us to determine the other unknown quantity. For materials undergoing significantly exothermic reactions, our method can discern the geometry of the printed object before material conversion begins to scatter light appreciably. The method can also quantify the temperature change in the surrounding uncured region.

5.2. Methodology

5.2.1. Resin formulation

To demonstrate the system's capability to detect thermal change in the print, a polymer precursor is chosen such that a significant amount of heat is generated throughout tomographic VAM printing with a typical patterning light intensity. Pentaerythritol tetraacrylate (CAS no. 4986-89-4, TCI) (PETRA) with 0.1 wt% Irgacure-369 (CAS no. 119313-12-1, Sigma-Aldrich) (I369) was found to release substantial heat under typical VAM patterning light intensity (8 mW/cm2) over 1–2 minutes, making the resin a good candidate for rapid testing of our detection system. PEG-DA-700 (CAS no. 26570-48-9, Sigma Aldrich) with 0.3 mM Phenylbis(2,4,6-trimethylbenzoyl) phosphine oxide (CAS no.162881-26-7, Sigma Aldrich) (BAPO) was also prepared for separate material characterization. The concentration of RhB (CAS no. 81-88-9, Sigma Aldrich) dissolved in the resin is chosen to be 5 μM to provide sufficient fluorescence signal without significant attenuation of excitation light or reabsorption of emitted light within the resin volume.

5.2.2. Absorbance/emission measurement and fluorescence calibration

The absorbance and emission spectra of resins were collected by a Vernier SpectroVis Plus UV-VIS spectrophotometer with a custom excitation light source at 532 nm. The fluorescence of RhB in PETRA resin as a function of absorbed optical dose and temperature was collected with a Molecular Devices SpectraMax M5 multimode microplate reader. The absorbed optical dose refers to the optical dose absorbed by the photoinitiator (I369 or BAPO). This quantity has a unit of mJ/cm3 and it is calculated by multiplying the areal optical dose in mJ/cm2 with the absorption coefficient of the photoinitiator at the patterning wavelength (405 nm). Resin samples across optical dose 0-93 mJ/cm3 were first cured in groups of four replicates on a clear-bottom 96-well plate (CellVis P96-1.5H-N). The plate was then read on the SpectraMax M5 microplate reader in fluorescence end-point mode with excitation wavelength = 532 nm and emission wavelength = 580 nm. A cutoff wavelength of 570 nm was set by the plate reader to filter unwanted signals from the excitation light. To account for signal variation across the well area induced by uneven curing or excitation illumination, a 3×3 point scan was done across each well, and the median of the nine-point signals was chosen to represent the fluorescence intensity measured at that well.

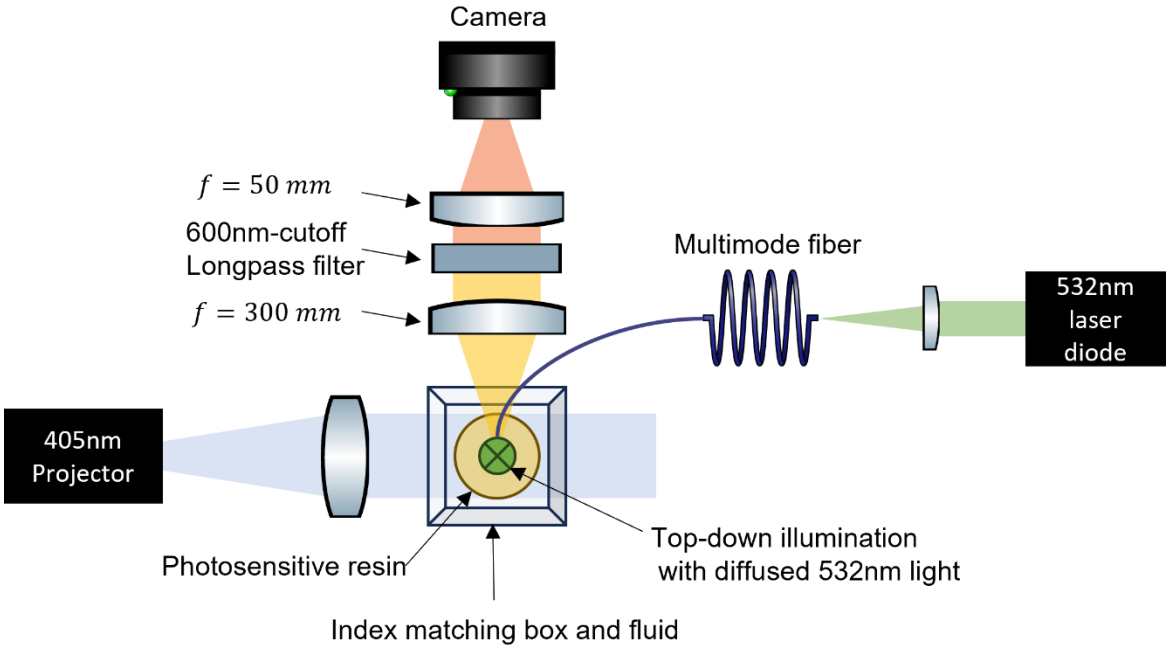


Figure 25. Schematic of tomographic fluorescence imaging system presented in this work.

5.2.3. Tomographic fluorescence imaging setup

Experimental hardware for the printing and fluorescence imaging experiments is shown in Figure 25. The optical projections used for printing had a center wavelength of 405 nm and a maximum intensity of 8 mW/cm^2 and were discretized at a spatial sampling rate of 32.8 pixels/mm at the sample volume. The vial containing the resin was immersed in a mineral oil index matching bath and was rotated at $24\ °/s$ during the experiment. A multimode optical fiber (Thorlabs AFS105/125Y) carried the excitation light output from a 532 nm diode laser to the fiber port

mounted on the top of the hollow shaft rotation stage. From the optical fiber, the 532 nm light illuminated the resin from above and through a diffuser.

The sample fluorescence was collected and imaged by a 4f system comprising two lenses with focal lengths of 300 mm and 50 mm (Thorlabs AC508-300-A-ML and LA1131-ML), through a long-pass filter (Thorlabs FELH0600) to a monochrome camera (Thorlabs 340M-USB). At the resulting 6× demagnification, the camera effectively sampled the fluorescent resin at 22.5 pixels/mm.

Image acquisition was electronically triggered to synchronize with the intermittent off-time of the patterning projection. Effectively, this synchronization prevented the camera from capturing the non-uniform fluorescence caused by the 405 nm patterning beam. Details of this electronic synchronization are described in Section 5.2.5.

5.2.4. Computational reconstruction

A multi-processing Python program was written to control the projector, diode laser, and camera. The data acquisition and processing pipeline is detailed in Section 5.2.6. During printing, a sequence of pre-computed patterning images was delivered by the projector to the resin. The set of images spanned a full vial rotation and contained one projected image per degree of rotation. These projections were optimized for the test object with the OSMO algorithm [69].

To estimate the spatial distribution of the resulting fluorescence intensity within the resin, the collected camera images were first denoised with a Gaussian filter and then used for reconstruction via filtered backprojection. This digital reconstruction process is detailed in Section 5.2.6. The resulting reconstruction is a volumetric representation of the local fluorescence intensity ratio relative to the local intensity at the baseline (25 °C and 0 mJ/cm^3 optical dose). Throughout an experiment, a temporal sequence of reconstructions can be produced, where each reconstruction is computed from images taken over one rotation period. Similar to CST [106], the multi-processing program is written such that reconstruction can be computed either in real-time during the experiment (at slower reconstruction refresh rates) or afterward (at higher refresh rates). The reconstruction demonstrated in this work was computed in real-time while analyses were performed after the experiment.

5.2.5. Electronic synchronization of patterning projection and image acquisition

To prevent imaging the fluorescence excited by the patterning light, the patterning and image acquisition were electronically synchronized to take place alternately. The LED of the projector was pulsed at 60 Hz at a duty cycle of 33 %. The camera was triggered immediately when this LED transitioned to off state and started a 9 ms of exposure. The exposure time was chosen such that the patterning and imaging do not overlap in time.

While this approach effectively rejects fluorescence excited by the patterning light, it poses a tradeoff between time spent in patterning and in image acquisition. The maximum intensity of the patterning projections was reduced to an average of 8 mW/cm^2 at 33 % duty cycle from

24 mW/cm^2 at 100 % duty cycle. The short exposure of the camera also reduced the signal-to-noise ratio (SNR) of the acquired images.

While the camera was triggered at 60 Hz, the frames were sampled at 30 Hz in experiments such that the camera captured exactly 360 images per vial rotation for reconstruction. In future experiments, a temporal averaging technique may be applied over images collected at 60 Hz to improve SNR. The SNR could also be improved by using a stronger excitation light source and a higher concentration of RhB.

5.2.6. Data acquisition, processing, and tomographic reconstruction pipeline

All hardware control, data acquisition, and processing were handled by a custom Python program. Using the multi-processing module, the main Python process spawns a new process for each of the tasks which includes image acquisition, image pre-processing, tomographic reconstruction, and data saving. This architecture was designed to concurrently process a real-time stream of data.

The image pre-processing steps included denoising, background subtraction, and Ram-Lak filtering. All collected images were first Gaussian-filtered with a kernel size of 11 pixels and a standard deviation of 7 pixels for denoising. Before printing, a set of denoised background images was collected without the presence of excitation or patterning light while the vial was rotating. All subsequent images used for reconstruction had the background image at the corresponding angle subtracted. For the subsequent filtered backprojection step in tomographic reconstruction, the images were filtered in the horizontal direction (perpendicular to the rotation axis) by a Ram-Lak filter before they were sent to another process downstream.

The tomographic reconstruction process was performed by filtered backprojection with the Astra toolbox [144]. There are multiple methods to group images together for tomographic reconstruction. These methods are defined as time-segmentation schemes in CST [106], [87]. Under the same definition, the reconstructions in this work used images within a moving window spanning one full rotation. In the real-time computation of reconstruction in this work, the entire image set was collected before the time of reconstruction. The reconstruction timestamps were set to be equal to the time when the last image in the set was taken. This contrasts with an offline implementation where reconstruction can be centered in the moving window.

The native tomographic reconstructions were expressed in units of greyscale value of the camera. To obtain the reconstructions in relative intensity, all reconstructions are normalized by a reference reconstruction. This reconstruction was collected one rotation before the start of the printing at the reference temperature and $0\,J/cm^{-3}$ absorbed dose with the excitation light turned on. Normalization was performed elementwise in each reconstruction voxel. After normalization, the reconstructions are expressed in $I_{relative}$ which physically represents the ratio of fluorescence intensity relative to the same voxel at the reference state. The local $I_{relative}$ can then be interpreted with the response surface of RhB.

5.2.7. Scattering observation by dark-field imaging

The scattering observation was done with a method similar to that of Orth et al. [11]. A diffused 635 nm laser source (Thorlabs CPS635S) illuminated top-down into the printing vial in the CAL

system. The scattered red light entered a camera (Panasonic Lumix GH4) viewing orthogonally to the light source. A long-pass filter (Thorlabs FELH0600) was placed in front of the camera to remove the 405 nm patterning light from the projector. The onset of scattering was determined directly on the acquired image by the appearance of any local increase of brightness against the background at the location of the printing object. This onset happened at 42 s and 72 s for the printing of trihelix and pyramid truss targets respectively.

5.2.8. Derivation of the relation between spatial and fluorescence intensity resolution in tomographic imaging

In tomographic fluorescence imaging, the value of each pixel in an image can be expressed as the line integral of fluorescence power along the line of imaging (optical axis). This approximation is accurate at the paraxial limit (when the system has a low numerical aperture (NA)). From this relationship, it can be shown that the resolution of fluorescence power density and spatial resolution of the tomographic reconstruction share the total bit-depth of the camera. A high-bit-depth camera is hence desirable for obtaining high spatial resolution and temperature/DOC resolution.

In a hypothetical scenario, let z be the coordinate along the optical axis of a 4f imaging system with magnification M, and x and y be the coordinates in the horizontal and vertical directions respectively. The imaging target is a fluorescent object when substantial thickness along the optical axis. The camera sensor plane is conjugated to the center plane of the imaging target. In this work, it is of interest to determine the minimum change of fluorescence power density change in one reconstruction voxel that the camera pixel can detect. In a parallel beam tomographic configuration, the reconstruction voxel width equals the width of one camera pixel.

Let $i(x', y')$ be the intensity at a particular point on the sensor plane parametrized by x' and y', $\alpha(x, y, z)$ be the solid angle subtended by the objective lens from a particular point (x, y, z) in space, $p(x, y, z)$ be the local isotropic fluorescence power density of a point (x, y, z) in space in units of $\mathrm{mW/cm^3}$, and $L(x, y)$ be z-thickness of the fluorescent object at (x, y). Assuming all light received by the objective lens is relayed to the corresponding point on the sensor, the intensity at a point on the sensor plane can be expressed as

$$i(x' = -Mx, y' = -My) = \int_{L(x,y)} \alpha(x, y, z) p(x, y, z)\, dz \tag{1}$$

under the imaging condition.

For a concise derivation, only events on a particular z-line at (x, y) is focused from this point onwards, and the functional dependence on (x, y) will be omitted. Let the bit-depth of the camera be b, and S be the saturation intensity at the given sensor setting. Each intensity level of the camera pixels is separated by $\frac{S}{2^b}$. Let $p_{ref}(z)$ be the fluorescence power density at the reference state.

For a change in fluorescence power density to be detectable,

$$\frac{S}{2^b} < \Delta i = \int_L \alpha(z) p(z)\, dz - \int_L \alpha(z) p_{ref}(z)\, dz \tag{2}$$

In low-NA systems and for objects with limited thickness such that α can be approximated as a constant,

$$\frac{S}{2^b} < \Delta i = \alpha \int_L p(z) - p_{ref}(z)\, dz \tag{3}$$

If the change of fluorescence power density is concentrated at z_0 along optical axis within a range $\left[z_0 - \frac{\Delta z}{2}, z_0 + \frac{\Delta z}{2}\right]$ where Δz is the thickness of one reconstruction voxel or equivalently width of one camera pixel size, then $p(z_0)$ and $p_{ref}(z_0)$ can be represented by their local spatial average p_{z_0} and p_{ref,z_0} respectively. Therefore, (3) can be rewritten as

$$\frac{S}{2^b} < \Delta i = \alpha \int_{z_0 - \frac{\Delta z}{2}}^{z_0 + \frac{\Delta z}{2}} p(z) - p_{ref}(z)\, dz \approx \alpha\left(p_{z_0} - p_{ref,z_0}\right) \int_{z_0 - \frac{\Delta z}{2}}^{z_0 + \frac{\Delta z}{2}} dz = \alpha\left(p_{z_0} - p_{ref,z_0}\right)\Delta z \tag{4}$$

From (4), it is clear that the product of $\left(p_{z_0} - p_{ref,z_0}\right)$ and Δz must be greater than a constant $\frac{S}{\alpha 2^b}$. For a small change in fluorescence, Δz must be large, which means the system has a poor reconstruction resolution. On the other hand, if Δz is required to be small, the fluorescence change must be large to be detectable. For a fixed hardware specification, it represents a tradeoff between spatial resolution and resolution of fluorescence power. To the goal of achieving both high spatial resolution and high temperature-DOC resolution, a high-bit-depth camera (large b) is desirable.

(4) can be rewritten in non-dimensional form. Let k be the ratio between the sensor saturation level and the reference state intensity at this (x, y) position, then $S = k\alpha \int_L p_{ref}(z)\, dz$. Then, the detection criterion becomes

$$\frac{1}{2^b} < \frac{\left(p_{z_0} - p_{ref,z_0}\right)\Delta z}{k \int_L p_{ref}(z)\, dz}\ . \tag{5}$$

With a uniform excitation light, typically the fluorescence power density at the reference state is spatially constant. This leads to a form in which both the fluorescence power density change and the voxel size are non-dimensionalized:

$$\frac{1}{2^b} < \frac{1}{k}\left(\frac{p_{z_0} - p_{ref}}{p_{ref}}\right)\left(\frac{\Delta z}{L}\right)\ . \tag{6}$$

The above equation only states the detection requirement in idealized noise-free environments. In practical situations, the minimum change in intensity change must also be significantly greater

than the average noise level Δi_{noise}. Following a similar argument as above, the signal-to-noise requirement is

$$\Delta i_{noise} \ll \Delta i = \alpha \int_L p(z) - p_{ref}(z)\, dz \approx \alpha\left(p_{z_0} - p_{ref,z_0}\right)\Delta z \tag{7}$$

$$\text{SNR} = \frac{\alpha\left(p_{z_0} - p_{ref,z_0}\right)\Delta z}{\Delta i_{noise}} \gg 1. \tag{8}$$

It can be deduced from equation (8) that SNR can be improved by using a larger NA (larger α) as well as a camera that allows for lower noise. Camera noise is typically comprised of three components: read noise, dark shot noise and photon shot noise. Read noise is inherent to the sensor and electronics design and is constant per instrument. Dark shot noise is dependent on the temperature of the sensor. Photon shot noise is a statistical noise and depends on the signal level measured. An actively cooled camera with a low-noise sensor and electronics can reduce the first two types of noises which lead to lower Δi_{noise} (SNR of the obtained data will be further discussed in Section 5.4).

5.2.9. Fourier transform infrared spectroscopy measurement

The DOC (acrylate C=C double bond conversion) as a function of absorbed dose was quantified *ex situ* using Fourier transform infrared (FTIR, Bruker Vertex80) spectroscopy. Samples of thickness ~1 mm between glass slides were prepared and the instrument backgrounded to blank slides. Samples were exposed to 405 nm light (Excelitas Omnicure S2000 with a Thorlabs FBH405-10 405 nm bandpass filter) for the duration of the experiment. The intensity of the light was measured before each experiment using a handheld radiometer (Thorlabs PM100D with S121C detector). During exposure, RT-FTIR scans were done in the range of 4000–8000 cm^{-1} with a step size of 4 cm^{-1} at a frequency of 40 kHz and measurement averaging of 64 with the CaF_2 beamsplitter and LN-MCT Mid IR detector from Bruker. The conversion was calculated from double bond concentrations determined by integrating the 6160 cm^{-1} C=C stretch peak using the tangent skim method.

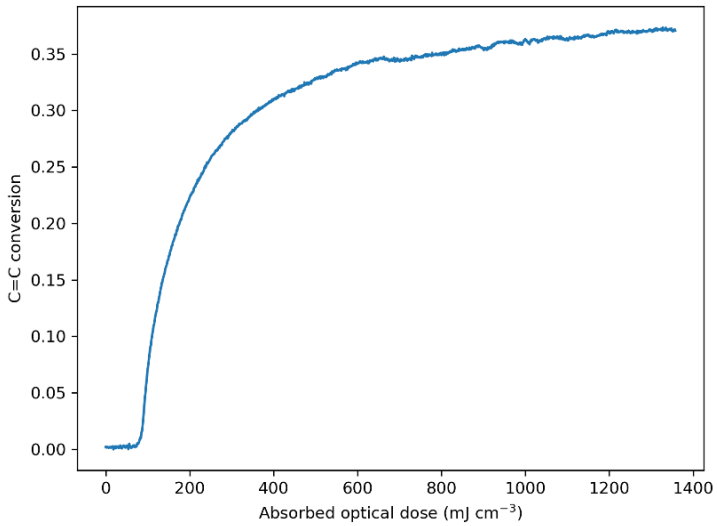


Figure 26 Real-time FTIR data of acrylate group conversion of PETRA + 5 µM RhB + 0.1 w/v% I369.

5.3. Temperature- and curing-dependent optical properties of RhB

The absorption spectrum of RhB in PETRA minimally overlapped with that of I369 or the patterning light used in this work, which had a center wavelength of 405 nm (Figure 27). Nevertheless, the residual light absorption at approximately 405 nm by RhB necessitated the application of time-gated and synchronized projection and image acquisition (Section 5.2.5). This ensured that the camera did not capture the non-uniform fluorescence created by the patterning beam.

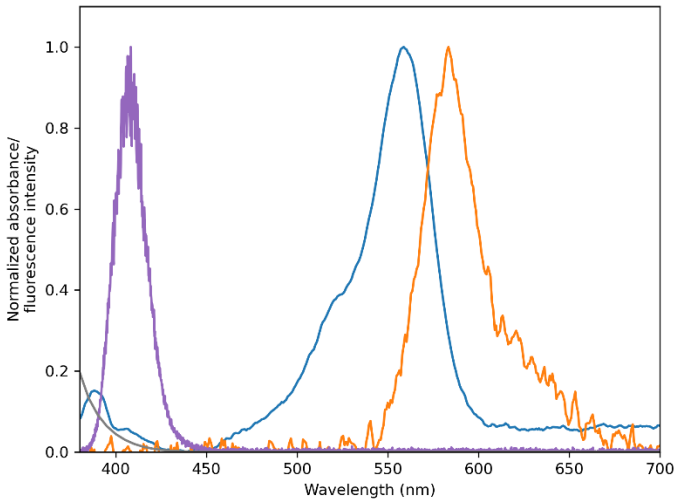


Figure 27. Normalized absorption (blue) and normalized fluorescence intensity (orange) of PETRA + 5 µM RhB upon excitation at 532 nm and normalized absorption of 2 mM I369 in isopropanol (gray). The 405 nm patterning light used in this study is plotted in purple.

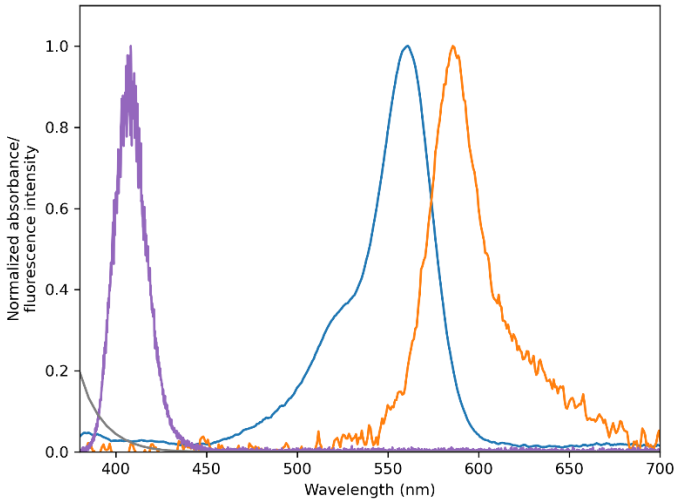


Figure 28. Normalized absorption (blue) and normalized fluorescence intensity (orange) of PEG-DA-700 + 5 µM RhB upon excitation at 532 nm, and normalized absorption of 2 mM I369 in isopropanol (gray). The 405 nm patterning light used in this study is plotted in purple.

As shown in Figure 29, the fluorescence of RhB excited by 532 nm decreases with temperature and absorbed optical dose of PETRA resin. In the case of unexposed resin, the fluorescence intensity drops 34 % over temperature increases of 34 °C. This corresponds to an average thermal sensitivity of 1 % per degree Celsius. Both the fluorescence intensity and its sensitivity to temperature decrease with absorbed dose. This effect can be attributed to the increased restriction of RhB molecules in the formed polymer network.

Notably, RhB's fluorescence intensity in PETRA resin declines significantly as a function of the resin's absorbed dose. A potential explanation for this could be the ionic nature of RhB versus the lower polarity of PETRA, given its tetrahedral acrylate moieties. This polarity difference could induce RhB aggregation and consequently result in fluorescence quenching [145].

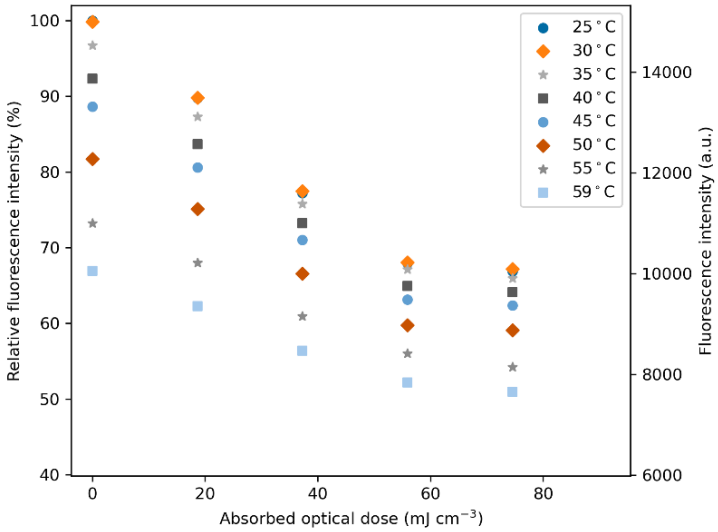


Figure 29. Fluorescence intensity (right axis) and relative fluorescence intensity compared to a baseline of 25°C and 0 mJ/cm^3 absorbed dose (left axis) of PETRA + 5 µM RhB + 0.1 w/v% I369, as a function of temperature and absorbed optical dose. The polymer precursor is excited at 532 nm.

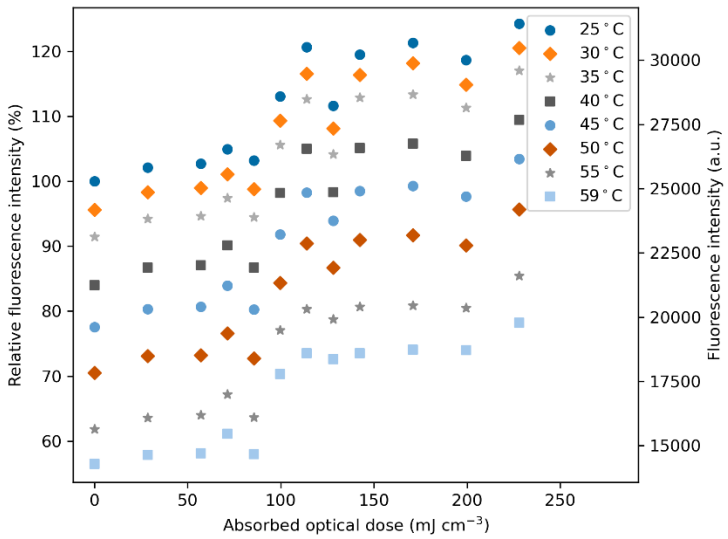


Figure 30. Fluorescence intensity (right axis) and the relative fluorescence intensity compared to a baseline of 25 °C and 0 mJ/cm3 absorbed dose (left axis) of PEG-DA-700 + 5 µM RhB + 0.3 mM BAPO, as a function of temperature and absorbed optical dose. The polymer precursor is excited at 532 nm.

On the other hand, the response surface of RhB in PEG-DA (at the same concentration of 5 µM) exhibited an opposite trend of fluorescence with absorbed dose (Figure 30). PEG-DA has a higher polarity than PETRA, which may facilitate the dispersion of RhB and allow the other temperature/exposure-dependent mechanism to dominate, such as the sensitivity related to the rotation of diethylamine groups in the molecule upon excitation as summarized in [146], [147]. These reports suggest elevated local viscosity is associated with the non-radiative decay of excited electrons, resulting in decreased fluorescence, while an increase in temperature has the opposite effect. This is in line with our intensity characterization data in Figure 30.

The formation of an amorphous polymer network induces spatial variation of refractive index and leads to scattering of both excitation light and emission from fluorophores within the material volume. As scattering lowers detected intensity in addition to temperature and exposure effects, the onset of scattering thereby established a cut-off for the absorbed dose range examined in the response surface characterization. In the above characterization, this scattering onset is indicated by an increase in measured absorbance on a well plate following an absorbed dose of 74.6 mJ/cm^3 (Figure 31).

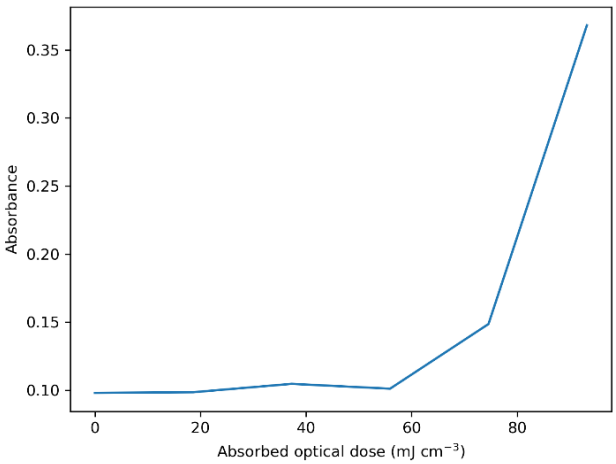
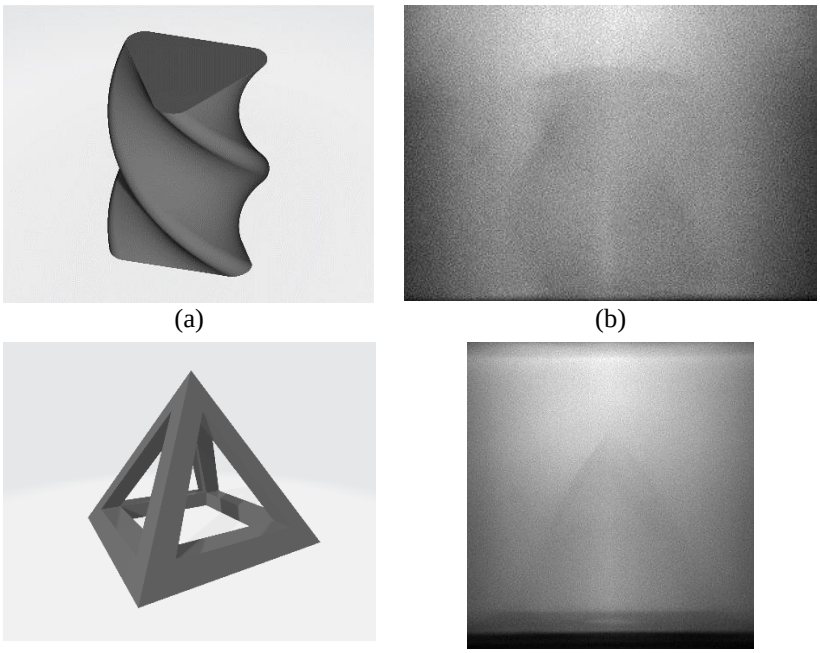


Figure 31. Absorbance of PETRA + 5 µM RhB + 0.1 w/v % I369 of various absorbed optical doses measured on a well plate. The onset of scattering is indicated by an increase in measured absorbance.

5.4. Tomographic reconstruction of VAM-printed objects

With the above material considerations in mind, two VAM-printed objects — a trihelix and a pyramid truss — were detected from their changes in fluorescence intensity. The objects were printed in the PETRA resin and their fluorescence images were collected, processed, and then used for tomographic reconstruction. From the raw fluorescence images (Figure 32), reduced intensity near the object could be detected. In the reconstruction (Figure 33), the volumetric distribution of relative fluorescence intensity ($I_{relative}$) could be recovered at each query time. From the resulting reconstructions, the reduction of $I_{relative}$ distributed in a similar shape as the printing object but extends further beyond the design part surface. The change of $I_{relative}$ is non-uniform, indicating potentially different rates of conversion and heat diffusion. From the reconstruction in the printing of the pyramid truss (Figure 33), the largest decrease of $I_{relative}$ happens in the five tips of the pyramid where the members of the truss meet. For an example location above the trihelix object, the time series of $I_{relative}$ was extracted and resolved for its local temperature under the assumption that this location has zero absorbed optical dose as it is located outside the part and above the height range under patterning exposure. As shown in Figure 34 (b), the temporal temperature profile computed from locally averaged $I_{relative}$ shows a clear increase after the end of patterning at 60 s. The onset of scattering in the prints was quantified separately with dark-field imaging (Section 5.2.7) and only the results generated before that time point are presented in Figure 29 and Figure 33. A separate run of the experiment was performed without printing to detect photobleaching of RhB by 532 nm excitation light. The effect of photobleaching was negligible throughout printing up to 450 s.

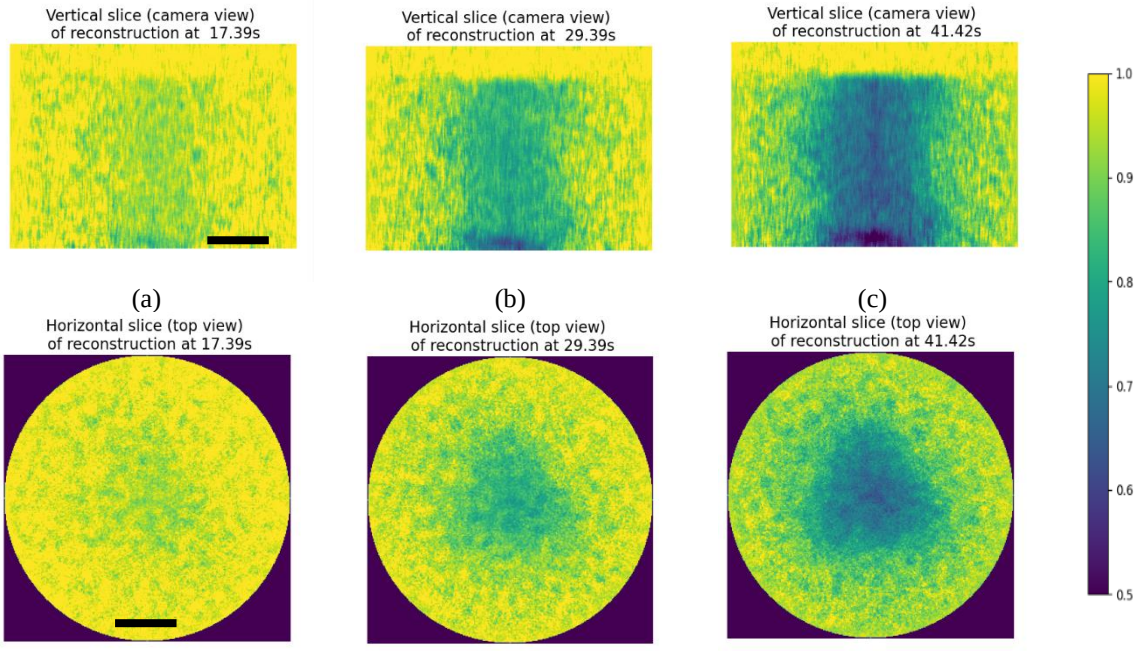
There is substantial room for improvement in the SNR on the acquired image and the computed reconstructions. The high noise level in the results can be attributed to the limited light collection during the short exposure time (9 ms) and to the low numerical aperture (0.085) of the imaging system. In future experiments, SNR can be improved by using a laser with higher power and more concentrated fluorophore in the resin. Temporal averaging over consecutively collected images can also be used to reduce noise.



(a) (b)

(c) (d)

Figure 32. (a) Geometry of trihelix target object; (b) raw fluorescence image captured at 166 s into printing of a trihelix, (c) geometry of pyramid truss target object; (d) raw image captured at 133 s into printing of a pyramid truss (black region at the bottom: bottom of the vial, grey region directly above: reduced fluorescence at the bottom of the pyramid truss).



(a) (b) (c)

(d) (e) (f)

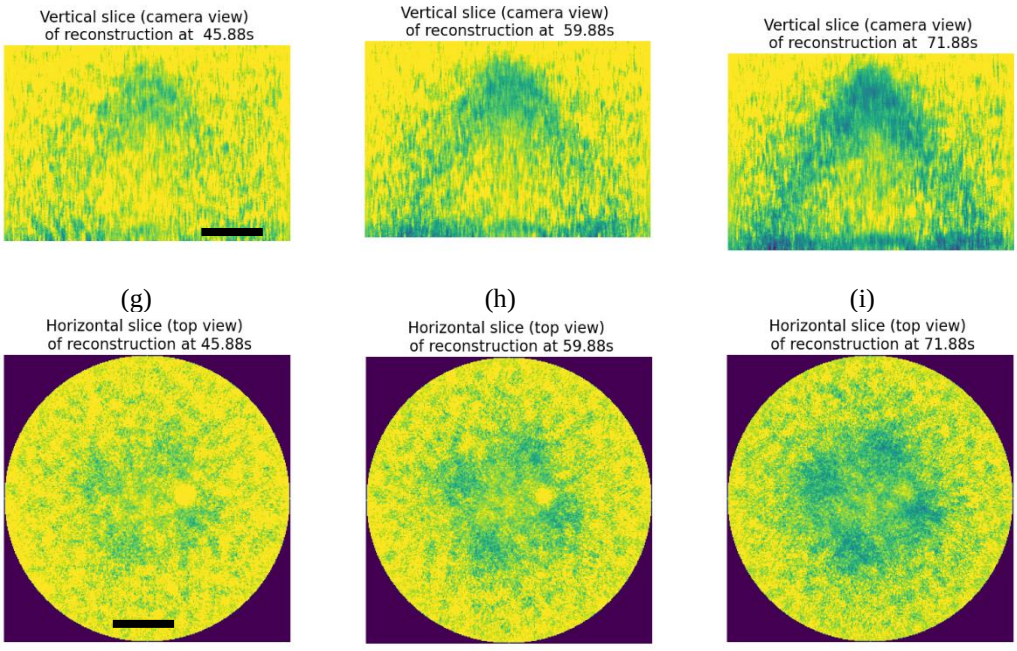


Figure 33. Central vertical and horizontal reconstruction slices of relative fluorescence intensity during printing of a trihelix (a–f) and a pyramid target (g–l). Scale bars: 3 mm.

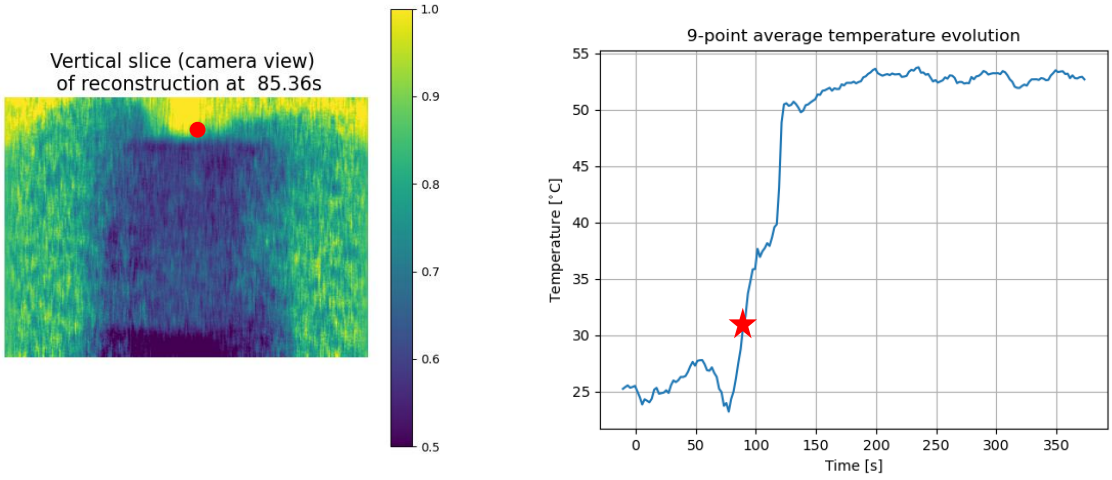


Figure 34. (a) a vertical slice of the reconstructed trihelix print at an example time point (85.36 s); (b) temporal temperature profile at a location near the top of the trihelix structure (red dot in (a)), where absorbed dose is assumed to be zero. At this location, a spatial average is taken over relative intensity in nine adjacent voxels in the horizontal plane of reconstruction. The average intensity is then mapped to temperature with the material's response surface along the line of zero absorbed dose. The red star indicates the temperature value at the location at 85.36 s.

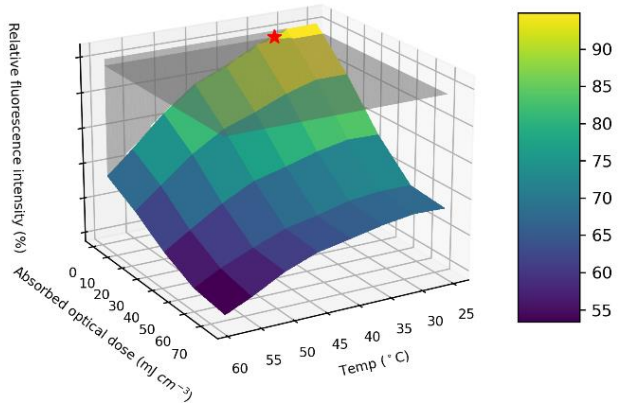


Figure 35. Illustration of obtaining material state information from RhB material response surface. Colored surface plot: response surface of PETRA + 5 µM RhB + 0.1 w/v % I369, in terms of fluorescence intensity relative to that at 25 °C and 0 mJ/cm^3 absorbed dose. The intersection of a specific reconstructed relative fluorescence intensity (gray plane) and the response surface gives a set of possible corresponding temperatures and absorbed dose (gray contour line). At spatial locations where the resin is unexposed (assumed absorbed dose = 0 $mJ \cdot cm^{-3}$), the temperature at that location is uniquely determined by the response surface (red star).

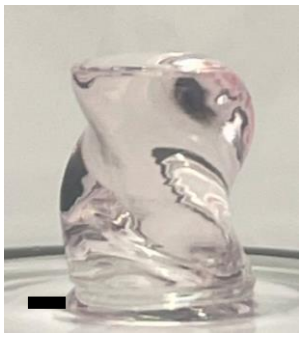


Figure 36. A printed trihelix object from captured fluorescence intensity. Scale bar: 1 mm.

5.5. Discussion and future work

Our research has established a tomographic fluorescence imaging system within the VAM framework for temperature and DOC characterization. The fluorescent probe implemented has demonstrated reasonable sensitivity to both temperature changes and photopolymerization exposure. Tomographic reconstruction further facilitates online and offline metrology, allowing us to capture volumetrically the evolution of temperature-dose profile both inside and outside the print, before the onset of substantial scattering. In a broader context, our work serves as an inaugural demonstration of tomographic measurement of material-state properties via an environment-sensitive fluorescent probe. Existing confocal measurements of state-dependent fluorescence [140] have limited axial sectioning capability at low NA due to the diffraction limit. The tomographic nature of our reconstruction method offers isotropic voxels in a low NA regime and therefore enables volumetric measurement at cm-scale or larger. This spatiotemporally resolved material-state measurement technique also presents potential applications in other AM modalities.

While RhB exhibited a thermal sensitivity of 1 % per degree Celsius, it was also found that it demonstrated varying degrees of absorbed-dose sensitivity in different polymer precursors. RhB's thermal and absorbed-dose sensitivity is also subject to the polarity of the resin and the aggregation effect, necessitating characterization specific to each resin. In the future, different fluorescent sensors can be examined for improving sensitivity. For example, BODIPY-derived molecular rotors have demonstrated tunable sensitivity to viscosity and/or temperature in both polar and non-polar solvents [146].

Certain limitations were identified in our study, particularly regarding the sensitivity of the optical system. The minimum detection level of voxel intensity change depends on the image pixel sampling rate, available bit-depth, and noise level. A relation between spatial and fluorescence intensity resolution in tomographic imaging is derived in Section 5.2.8. Apart from hardware, there are various image processing decisions (such as denoising parameters) that represent tradeoffs between spatial resolution and intensity resolution. Furthermore, scattering posed a significant challenge to interpreting results generated after the onset of the phenomenon. Scattering arises from local changes in the refractive index and the self-lensing effect associated with directed patterning illumination [148]. For reconstructions after the onset of part scattering, the quantitative analysis is limited to levels above the object height, as the tomographic light propagation model's accuracy was compromised by unaccounted scattering within the same height level as the object. The scattering onset of the print is characterized using a dark-field imaging setup (Section 5.2.7) and only presented results generated before that time point in Figure 29 and Figure 33. To mitigate the impact of scattering, future work could implement techniques such as tomosynthetic printing [149], [69] or latent image VAM [148], or utilize a low-shrinkage resin with a smaller change in refractive index. Future work could also explore dual-mode detection for simultaneous resolution of both temperature and DOC. For instance, multiple chemical probes at orthogonal wavelengths could be employed, as well as two-color ratiometric measurements on a single chemical probe.

5.6. Conclusion

This chapter establishes the use of RhB and tomographic fluorescence imaging for real-time monitoring of temperature and degree of conversion in VAM. The fluorescent properties of RhB demonstrated sensitivity to temperature and curing, though the exact effects varied across different polymer precursors. Scattering of light during printing limits the valid observation time and points to future investigations in conjunction with scattering-free printing methods. This technique, which is termed Tomographic Fluorescence Thermography (TFT), illustrates the potential of and lays the foundations for the development of two-wavelength spatiotemporal measurement systems that uniquely resolve both temperature and DOC.

Chapter 6

Future directions and conclusion

The mechanics of the cellular microenvironment determine the fate of the tissue construct, cell proliferation, and the ability of vascular cells to form organic networks within the matrix. As has been demonstrated in this thesis, an elastic modulus of even a thousand Pa can be too stiff for HMEC-1 cells and can inhibit cell motility and the formation of microvascular networks. On the other hand, hydrogels of sub-kPa stiffness are challenging to print using conventional layer-based additive processes due to their compliance and deformation during the printing process. The geometry of the vascular structure is also extremely important, not only from the biological perspectives briefly explained before but also from a fluid mechanics perspective, where the critical effects of biological flow such as pulsatility and wall compliance, and the induced wall shear stress can significantly alter cell growth, morphology, and arrangement as well as mass transport either throughout the culture process or after the *in vitro* model is culture to maturation.

Through CAL, this thesis has demonstrated the ability to print three-dimensional perfusable structures with sub-milimeter diameters within 3 w/v % and 5 w/v % Gel-MA hydrogels, which exhibit an elastic modulus down to 100 Pa. Moreover, it has been illustrated that, with typical cell seeding densities of a few million cells per mL, these matrices support the formation of microcapillary networks spanning distances exceeding 500 μm in 11 days. With the enhanced patterning resolution of microCAL, the lower limit of negative feature (void) size has been further reduced to 100 μm in 90% DS 5 w/v % Gel-MA, proving the capability to print perfusable channels close to the size of arteriole and venules (Section 1.3).

However, two major limitations remain. Gel-MA's long oligomer chains, low concentration and compliance give rise to (1) low printing contrast/accuracy and (2) small changes in material properties from the point of current *in situ* metrology e.g. refractive index tracking (further discussion on (2) below). Strategies to improve general patterning accuracy may include, from a projection generation point of view, accounting for the physics of radical species generation, transport and consumption. From a material point of view, thermally tuning the stiffness of Gel-MA pre-print, employing post-print patterning methods such as enzymatic or photo-degradation [150], and introducing multicolor patterning via orthogonal chemistry also add more freedom to patterning control [151]. As for cell-embedded hydrogels, index-matching heterogeneous refractive index brought by embedded cells with e.g. iodixanol (IDX) has shown success in Gel-MA, glycidyl methacrylate hyaluronic acid (GMHA), alginate methacrylate (Alg-MA) and gelatin [33], [111], [115]. Introducing spatially-controlled radical inhibition in addition to radical generation addresses both projection generation and material aspect, as this strategy not only introduces an additional patterning control but also effectively creates a "negative dose" and lifts the constraint for a positive light dose during projection optimization.

In general, perfusable bioprinted constructs face the challenge of interfacing with the fluidic system post-printing. Many perfusable bioprints reported to date require the transfer from the print vessel to a perfusion chamber/culture vessel before perfusion [32], [33], [112], [152], [153], which risks contamination and damage of prints during manual transfer and coupling with the fluidic source. Since the shear stress, pulsatility and material transport brought by the flow can

significantly impact endothelial cell development, having a perfusable bioprint with a stable coupling to a fluidic system that can provide controlled flow is of high significance to engineering a physiological endothelium model.

This thesis provides one of the first examples of a VAM-compatible integrated perfusion device that allows for contact-free CAL printing, post-processing, and perfusion of the printed hydrogel constructs. This system showcases the unique potential of CAL in overprinting soft structures onto pre-existing solid components positioned within the build volume. However, the effectiveness of the capsule to house, perfuse and observe bioprinted hydrogel constructs is still limited by the choice of tube materials and alignment with the CAL printers. Although glass offers excellent transparency for visible light and tight dimensional tolerance, glass tube manufacturing and cutting require specialized tools that drive up production costs and limit material availability. Meanwhile, plastic tube is a more accessible material but suffers from its compliance and low dimensional accuracy, making it unsuitable for mechanical coupling for precision vial alignment. Precision alignment of the vial with the printer should be ensured and can be improved by restricting planes of movement, for example, fixing both ends of the vial during the patterning rotations.

As mentioned previously, the properties of hydrogel set hurdles to high-accuracy printing and call for alternative inspection techniques both *in situ* and *ex situ*. Current *in situ* inspection methods offer insights into tracking the changes in the shape and refractive index of the printed object. However, to assess additional factors like temperature and chemical concentration relevant to photopolymerization, one must either develop a suitable model linking optical data to the desired property or thorough *ex situ* measurements to establish empirical correlations between these properties [154]. As such, a new *in situ* inspection method based on heat and print state sensing through a fluorescent dye was introduced in this thesis. The fluorescent properties of RhB demonstrated sensitivity to both temperature and curing, and real-time sensing using the system has been shown for two prints with engineering resins. This technique shows tremendous potential for noninvasive inspection beyond VAM and temperature/DOC detection, as any fluorescent dye showing dependence on material properties can be added to compatible samples of interest where tomographic reconstruction is permitted. The imaging and reconstruction setup themselves can also be applied for detecting other fluorescent signals tomographically.

Moving forward, a major bottleneck lies in finding a candidate dye for the resin(s) of interest that dissolves, shows a strong dependence on the desired material property, and has emission and excitation spectra orthogonal to existing chemistries in the resin(s). RhB is chosen in this study because of its accessibility and solubility in the PETRA resin; however, the dual sensitivity of RhB cannot be decoupled without additional constraints. Using molecular probes responding to a single local material properties, for instance molecular rotors [146] and molecules with aggregation-induced-emission (AIE) behavior [155], or a multi-probe/multi-channel measurement strategy, evolving material properties confounded by current inspection methods can be measured. This opens new opportunities in sensing various material properties/chemical species in VAM resins, providing valuable feedback in process control and useful validation for multiphysics models.

References

[1] S. V. Murphy and A. Atala, "3D bioprinting of tissues and organs," *Nat Biotechnol*, vol. 32, no. 8, pp. 773–785, Aug. 2014, doi: 10.1038/nbt.2958.

[2] W. S. Harley *et al.*, "Advances in biofabrication techniques towards functional bioprinted heterogeneous engineered tissues: A comprehensive review," *Bioprinting*, vol. 23, p. e00147, Aug. 2021, doi: 10.1016/j.bprint.2021.e00147.

[3] E. Bicudo, A. Faulkner, and P. Li, "Patents and the experimental space: social, legal and geographical dimensions of 3D bioprinting," *International Review of Law, Computers & Technology*, vol. 35, no. 1, pp. 2–23, Jan. 2021, doi: 10.1080/13600869.2020.1785066.

[4] M. Rodríguez-Salvador, R. M. Rio-Belver, and G. Garechana-Anacabe, "Scientometric and patentometric analyses to determine the knowledge landscape in innovative technologies: The case of 3D bioprinting," *PLoS ONE*, vol. 12, no. 6, p. e0180375, Jun. 2017, doi: 10.1371/journal.pone.0180375.

[5] N. V. Mekhileri *et al.*, "Automated 3D bioassembly of micro-tissues for biofabrication of hybrid tissue engineered constructs," *Biofabrication*, vol. 10, no. 2, p. 024103, Jan. 2018, doi: 10.1088/1758-5090/aa9ef1.

[6] L. Moroni *et al.*, "Biofabrication strategies for 3D in vitro models and regenerative medicine," *Nat Rev Mater*, vol. 3, no. 5, pp. 21–37, Apr. 2018, doi: 10.1038/s41578-018-0006-y.

[7] T. Zandrini, S. Florczak, R. Levato, and A. Ovsianikov, "Breaking the resolution limits of 3D bioprinting: future opportunities and present challenges," *Trends in Biotechnology*, vol. 41, no. 5, pp. 604–614, May 2023, doi: 10.1016/j.tibtech.2022.10.009.

[8] G. Forgacs, "Applications of extrusion bioprinting," in *3D Bioprinting in Regenerative Engineering*, 1st ed., Boca Raton : Taylor & Francis, 2018.: CRC Press, 2018, pp. 51–75. doi: 10.1201/b21916-3.

[9] I. T. Ozbolat and M. Hospodiuk, "Current advances and future perspectives in extrusion-based bioprinting," *Biomaterials*, vol. 76, pp. 321–343, Jan. 2016, doi: 10.1016/j.biomaterials.2015.10.076.

[10] A. Khademhosseini, *3D Bioprinting in Regenerative Engineering: Principles and Applications*, 1st ed. Boca Raton : Taylor & Francis, 2018.: CRC Press, 2018. doi: 10.1201/b21916.

[11] S. Boularaoui, G. Al Hussein, K. A. Khan, N. Christoforou, and C. Stefanini, "An overview of extrusion-based bioprinting with a focus on induced shear stress and its effect on cell viability," *Bioprinting*, vol. 20, p. e00093, Dec. 2020, doi: 10.1016/j.bprint.2020.e00093.

[12] P. Calvert, "Inkjet Printing for Materials and Devices," *Chem. Mater.*, vol. 13, no. 10, pp. 3299–3305, Oct. 2001, doi: 10.1021/cm0101632.

[13] M. Singh, H. M. Haverinen, P. Dhagat, and G. E. Jabbour, "Inkjet Printing—Process and Its Applications," *Advanced Materials*, vol. 22, no. 6, pp. 673–685, Feb. 2010, doi: 10.1002/adma.200901141.

[14] N. Hopkinson and P. J. Smith, "Industrial 3D Inkjet Printing/Additive Manufacturing," in *Handbook of Industrial Inkjet Printing*, 1st ed., W. Zapka, Ed., Wiley, 2017, pp. 649–660. doi: 10.1002/9783527687169.ch38.

[15] X. Zhang and Y. Zhang, "Tissue Engineering Applications of Three-Dimensional Bioprinting," *Cell Biochem Biophys*, vol. 72, no. 3, pp. 777–782, Jul. 2015, doi: 10.1007/s12013-015-0531-x.

[16] S. Iwanaga, K. Arai, and M. Nakamura, "Inkjet Bioprinting," in *Essentials of 3D Biofabrication and Translation*, Elsevier, 2015, pp. 61–79. doi: 10.1016/B978-0-12-800972-7.00004-9.

[17] J.-F. Xing, M.-L. Zheng, and X.-M. Duan, "Two-photon polymerization microfabrication of hydrogels: an advanced 3D printing technology for tissue engineering and drug delivery," *Chem. Soc. Rev.*, vol. 44, no. 15, pp. 5031–5039, 2015, doi: 10.1039/C5CS00278H.

[18] X. Zhou, Y. Hou, and J. Lin, "A review on the processing accuracy of two-photon polymerization," *AIP Advances*, vol. 5, no. 3, p. 030701, Mar. 2015, doi: 10.1063/1.4916886.

[19] M. Vaezi, H. Seitz, and S. Yang, "A review on 3D micro-additive manufacturing technologies," *Int J Adv Manuf Technol*, vol. 67, no. 5–8, pp. 1721–1754, Jul. 2013, doi: 10.1007/s00170-012-4605-2.
[20] Q. Geng, D. Wang, P. Chen, and S.-C. Chen, "Ultrafast multi-focus 3-D nano-fabrication based on two-photon polymerization," *Nat Commun*, vol. 10, no. 1, p. 2179, May 2019, doi: 10.1038/s41467-019-10249-2.
[21] L. Yang *et al.*, "Two-photon polymerization of cylinder microstructures by femtosecond Bessel beams," *Applied Physics Letters*, vol. 105, no. 4, p. 041110, Jul. 2014, doi: 10.1063/1.4891841.
[22] L. Yuan and P. R. Herman, "Laser Scanning Holographic Lithography for Flexible 3D Fabrication of Multi-Scale Integrated Nano-structures and Optical Biosensors," *Sci Rep*, vol. 6, no. 1, p. 22294, Feb. 2016, doi: 10.1038/srep22294.
[23] K. S. Lim, J. H. Galarraga, X. Cui, G. C. J. Lindberg, J. A. Burdick, and T. B. F. Woodfield, "Fundamentals and Applications of Photo-Cross-Linking in Bioprinting," *Chem. Rev.*, vol. 120, no. 19, pp. 10662–10694, Oct. 2020, doi: 10.1021/acs.chemrev.9b00812.
[24] J. R. Tumbleston *et al.*, "Continuous liquid interface production of 3D objects," *Science*, vol. 347, no. 6228, pp. 1349–1352, Mar. 2015, doi: 10.1126/science.aaa2397.
[25] R. Janusziewicz, J. R. Tumbleston, A. L. Quintanilla, S. J. Mecham, and J. M. DeSimone, "Layerless fabrication with continuous liquid interface production," *Proc. Natl. Acad. Sci. U.S.A.*, vol. 113, no. 42, pp. 11703–11708, Oct. 2016, doi: 10.1073/pnas.1605271113.
[26] D. E. Düzgün and K. Nadolny, "Continuous liquid interface production (CLIP) method for rapid prototyping," *Journal of Mechanical and Energy Engineering*, vol. 2, no. 1, pp. 5–12, Apr. 2018, doi: 10.30464/jmee.2018.2.1.5.
[27] B. E. Kelly, I. Bhattacharya, H. Heidari, M. Shusteff, C. M. Spadaccini, and H. K. Taylor, "Volumetric additive manufacturing via tomographic reconstruction," *Science*, vol. 363, no. 6431, pp. 1075–1079, Mar. 2019, doi: 10.1126/science.aau7114.
[28] M. Shusteff *et al.*, "One-step volumetric additive manufacturing of complex polymer structures," *Sci. Adv.*, vol. 3, no. 12, p. eaao5496, Dec. 2017, doi: 10.1126/sciadv.aao5496.
[29] M. Regehly *et al.*, "Xolography for linear volumetric 3D printing," *Nature*, vol. 588, no. 7839, Art. no. 7839, Dec. 2020, doi: 10.1038/s41586-020-3029-7.
[30] L. Stüwe *et al.*, "Continuous Volumetric 3D Printing: Xolography in Flow," *Advanced Materials*, vol. 36, no. 4, p. 2306716, Jan. 2024, doi: 10.1002/adma.202306716.
[31] J. Gehlen, W. Qiu, G. N. Schädli, R. Müller, and X.-H. Qin, "Tomographic volumetric bioprinting of heterocellular bone-like tissues in seconds," *Acta Biomaterialia*, vol. 156, pp. 49–60, Jan. 2023, doi: 10.1016/j.actbio.2022.06.020.
[32] P. N. Bernal *et al.*, "Volumetric Bioprinting of Complex Living-Tissue Constructs within Seconds," *Advanced Materials*, vol. 31, no. 42, p. 1904209, Oct. 2019, doi: 10.1002/adma.201904209.
[33] P. N. Bernal *et al.*, "Volumetric Bioprinting of Organoids and Optically Tuned Hydrogels to Build Liver-Like Metabolic Biofactories," *Advanced Materials*, vol. 34, no. 15, p. 2110054, Apr. 2022, doi: 10.1002/adma.202110054.
[34] R. Rizzo, D. Ruetsche, H. Liu, and M. Zenobi-Wong, "Optimized Photoclick (Bio)Resins for Fast Volumetric Bioprinting," *Advanced Materials*, vol. 33, no. 49, p. 2102900, Dec. 2021, doi: 10.1002/adma.202102900.
[35] H. Liu *et al.*, "Filamented Light (FLight) Biofabrication of Highly Aligned Tissue-Engineered Constructs," *Advanced Materials*, vol. 34, no. 45, p. 2204301, Nov. 2022, doi: 10.1002/adma.202204301.
[36] J. Madrid-Wolff, A. Boniface, D. Loterie, P. Delrot, and C. Moser, "Controlling Light in Scattering Materials for Volumetric Additive Manufacturing," *Advanced Science*, vol. 9, no. 22, p. 2105144, Aug. 2022, doi: 10.1002/advs.202105144.
[37] G. Größbacher *et al.*, "Volumetric Printing Across Melt Electrowritten Scaffolds Fabricates Multi-Material Living Constructs with Tunable Architecture and Mechanics," *Advanced Materials*, vol. 35, no. 32, p. 2300756, Aug. 2023, doi: 10.1002/adma.202300756.

[38] D. Ribezzi *et al.*, “Shaping Synthetic Multicellular and Complex Multimaterial Tissues via Embedded Extrusion-Volumetric Printing of Microgels,” *Advanced Materials*, vol. 35, no. 36, p. 2301673, Sep. 2023, doi: 10.1002/adma.202301673.
[39] C. F. Guimarães, L. Gasperini, A. P. Marques, and R. L. Reis, “The stiffness of living tissues and its implications for tissue engineering,” *Nat Rev Mater*, vol. 5, no. 5, pp. 351–370, Feb. 2020, doi: 10.1038/s41578-019-0169-1.
[40] N. Petitjean, P. Canadas, P. Royer, D. Noël, and S. Le Floc’h, “Cartilage biomechanics: From the basic facts to the challenges of tissue engineering,” *J Biomedical Materials Res*, vol. 111, no. 7, pp. 1067–1089, Jul. 2023, doi: 10.1002/jbm.a.37478.
[41] S. J. McDonald, P. C. Dooley, A. C. McDonald, J. A. Schuijers, A. R. Ward, and B. L. Grills, “Early fracture callus displays smooth muscle-like viscoelastic properties ex vivo: Implications for fracture healing,” *Journal Orthopaedic Research*, vol. 27, no. 11, pp. 1508–1513, Nov. 2009, doi: 10.1002/jor.20923.
[42] O. Chaudhuri *et al.*, “Hydrogels with tunable stress relaxation regulate stem cell fate and activity,” *Nature Mater*, vol. 15, no. 3, pp. 326–334, Mar. 2016, doi: 10.1038/nmat4489.
[43] S. Fleischer, D. N. Tavakol, and G. Vunjak-Novakovic, “From Arteries to Capillaries: Approaches to Engineering Human Vasculature,” *Adv Funct Materials*, vol. 30, no. 37, p. 1910811, Sep. 2020, doi: 10.1002/adfm.201910811.
[44] G. F. Muschler, C. Nakamoto, and L. G. Griffith, “ENGINEERING PRINCIPLES OF CLINICAL CELL-BASED TISSUE ENGINEERING:,” *The Journal of Bone and Joint Surgery-American Volume*, vol. 86, no. 7, pp. 1541–1558, Jul. 2004, doi: 10.2106/00004623-200407000-00029.
[45] M.-N. Giraud, C. Armbruster, T. Carrel, and H. T. Tevaearai, “Current State of the Art in Myocardial Tissue Engineering,” *Tissue Engineering*, vol. 13, no. 8, pp. 1825–1836, Aug. 2007, doi: 10.1089/ten.2006.0110.
[46] B.-S. Kim, J. Nikolovski, J. Bonadio, and D. J. Mooney, “Cyclic mechanical strain regulates the development of engineered smooth muscle tissue,” *Nat Biotechnol*, vol. 17, no. 10, pp. 979–983, Oct. 1999, doi: 10.1038/13671.
[47] S. V. S. Gangoda *et al.*, “Pulsatile stretch as a novel modulator of amyloid precursor protein processing and associated inflammatory markers in human cerebral endothelial cells,” *Sci Rep*, vol. 8, no. 1, p. 1689, Jan. 2018, doi: 10.1038/s41598-018-20117-6.
[48] G. M. Price, K. H. K. Wong, J. G. Truslow, A. D. Leung, C. Acharya, and J. Tien, “Effect of mechanical factors on the function of engineered human blood microvessels in microfluidic collagen gels,” *Biomaterials*, vol. 31, no. 24, pp. 6182–6189, Aug. 2010, doi: 10.1016/j.biomaterials.2010.04.041.
[49] B. Zohar, Y. Blinder, D. J. Mooney, and S. Levenberg, “Flow-Induced Vascular Network Formation and Maturation in Three-Dimensional Engineered Tissue,” *ACS Biomater. Sci. Eng.*, vol. 4, no. 4, pp. 1265–1271, Apr. 2018, doi: 10.1021/acsbiomaterials.7b00025.
[50] S. Kim, H. Lee, M. Chung, and N. L. Jeon, “Engineering of functional, perfusable 3D microvascular networks on a chip,” *Lab Chip*, vol. 13, no. 8, p. 1489, 2013, doi: 10.1039/c3lc41320a.
[51] F. W. Charbonier, M. Zamani, and N. F. Huang, “Endothelial Cell Mechanotransduction in the Dynamic Vascular Environment,” *Adv. Biosys.*, vol. 3, no. 2, p. 1800252, Feb. 2019, doi: 10.1002/adbi.201800252.
[52] I. K. Zervantonakis, S. K. Hughes-Alford, J. L. Charest, J. S. Condeelis, F. B. Gertler, and R. D. Kamm, “Three-dimensional microfluidic model for tumor cell intravasation and endothelial barrier function,” *Proc. Natl. Acad. Sci. U.S.A.*, vol. 109, no. 34, pp. 13515–13520, Aug. 2012, doi: 10.1073/pnas.1210182109.
[53] D. Huh, B. D. Matthews, A. Mammoto, M. Montoya-Zavala, H. Y. Hsin, and D. E. Ingber, “Reconstituting Organ-Level Lung Functions on a Chip,” *Science*, vol. 328, no. 5986, pp. 1662–1668, Jun. 2010, doi: 10.1126/science.1188302.

[54] A. Mathur *et al.*, "Human iPSC-based Cardiac Microphysiological System For Drug Screening Applications," *Sci Rep*, vol. 5, no. 1, p. 8883, Mar. 2015, doi: 10.1038/srep08883.
[55] C. R. Kothapalli *et al.*, "A high-throughput microfluidic assay to study neurite response to growth factor gradients," *Lab Chip*, vol. 11, no. 3, pp. 497–507, 2011, doi: 10.1039/C0LC00240B.
[56] R. He, D. Yunus, C. Uhl, W. Shi, S. Sohrabi, and Y. Liu, "Fabrication of circular microfluidic channels through grayscale dual-projection lithography," *Microfluid Nanofluid*, vol. 21, no. 1, p. 13, Jan. 2017, doi: 10.1007/s10404-017-1851-5.
[57] M. Fenech, V. Girod, V. Claveria, S. Meance, M. Abkarian, and B. Charlot, "Microfluidic blood vasculature replicas using backside lithography," *Lab Chip*, vol. 19, no. 12, pp. 2096–2106, 2019, doi: 10.1039/C9LC00254E.
[58] R. Seghir and S. Arscott, "Extended PDMS stiffness range for flexible systems," *Sensors and Actuators A: Physical*, vol. 230, pp. 33–39, Jul. 2015, doi: 10.1016/j.sna.2015.04.011.
[59] Y. Zhang, Y. Yu, A. Akkouch, A. Dababneh, F. Dolati, and I. T. Ozbolat, "In vitro study of directly bioprinted perfusable vasculature conduits," *Biomater. Sci.*, vol. 3, no. 1, pp. 134–143, 2015, doi: 10.1039/C4BM00234B.
[60] Y. Yu, Y. Zhang, J. A. Martin, and I. T. Ozbolat, "Evaluation of Cell Viability and Functionality in Vessel-like Bioprintable Cell-Laden Tubular Channels," *Journal of Biomechanical Engineering*, vol. 135, no. 9, p. 091011, Sep. 2013, doi: 10.1115/1.4024575.
[61] E. Mirdamadi, J. W. Tashman, D. J. Shiwarski, R. N. Palchesko, and A. W. Feinberg, "FRESH 3D Bioprinting a Full-Size Model of the Human Heart," *ACS Biomater. Sci. Eng.*, vol. 6, no. 11, pp. 6453–6459, Nov. 2020, doi: 10.1021/acsbiomaterials.0c01133.
[62] M. A. Skylar-Scott *et al.*, "Biomanufacturing of organ-specific tissues with high cellular density and embedded vascular channels," *Sci. Adv.*, vol. 5, no. 9, p. eaaw2459, Sep. 2019, doi: 10.1126/sciadv.aaw2459.
[63] N. Contessi Negrini, M. Bonnetier, G. Giatsidis, D. P. Orgill, S. Farè, and B. Marelli, "Tissue-mimicking gelatin scaffolds by alginate sacrificial templates for adipose tissue engineering," *Acta Biomaterialia*, vol. 87, pp. 61–75, Mar. 2019, doi: 10.1016/j.actbio.2019.01.018.
[64] H. Cui *et al.*, "Engineering a Novel 3D Printed Vascularized Tissue Model for Investigating Breast Cancer Metastasis to Bone," *Adv Healthcare Materials*, vol. 9, no. 15, p. 1900924, Aug. 2020, doi: 10.1002/adhm.201900924.
[65] B. Grigoryan *et al.*, "Multivascular networks and functional intravascular topologies within biocompatible hydrogels," *Science*, vol. 364, no. 6439, pp. 458–464, May 2019, doi: 10.1126/science.aav9750.
[66] R. Rizzo *et al.*, "Multiscale Hybrid Fabrication: Volumetric Printing Meets Two-Photon Ablation," *Adv Materials Technologies*, vol. 8, no. 11, p. 2201871, Jun. 2023, doi: 10.1002/admt.202201871.
[67] C. Koch, L. Van Hulle, and N. Rudolph, "Investigation of mechanical anisotropy of the fused filament fabrication process via customized tool path generation," *Additive Manufacturing*, vol. 16, pp. 138–145, Aug. 2017, doi: 10.1016/j.addma.2017.06.003.
[68] I. Bhattacharya, J. Toombs, and H. Taylor, "High fidelity volumetric additive manufacturing," *Additive Manufacturing*, vol. 47, p. 102299, Nov. 2021, doi: 10.1016/j.addma.2021.102299.
[69] C. M. Rackson *et al.*, "Object-space optimization of tomographic reconstructions for additive manufacturing," *Additive Manufacturing*, vol. 48, p. 102367, Dec. 2021, doi: 10.1016/j.addma.2021.102367.
[70] Y. Zhang, M. Liu, H. Liu, C. Gao, Z. Jia, and R. Zhai, "Edge-Enhanced Object-Space Model Optimization of Tomographic Reconstructions for Additive Manufacturing," *Micromachines*, vol. 14, no. 7, p. 1362, Jun. 2023, doi: 10.3390/mi14071362.
[71] T. Chen, H. Li, and X. Liu, "Statistical iterative pattern generation in volumetric additive manufacturing based on ML-EM," *Optics Communications*, vol. 537, p. 129448, Jun. 2023, doi: 10.1016/j.optcom.2023.129448.

[72] T. Chen *et al.*, "High-fidelity tomographic additive manufacturing for large-volume and high-attenuation situations using expectation maximization algorithm," *Additive Manufacturing*, vol. 80, p. 103968, Jan. 2024, doi: 10.1016/j.addma.2024.103968.
[73] C. C. Li, J. Toombs, H. K. Taylor, and T. J. Wallin, "Tomographic projection optimization for volumetric additive manufacturing with general band constraint Lp-norm minimization." arXiv, Dec. 03, 2023. Accessed: Jan. 07, 2024. [Online]. Available: http://arxiv.org/abs/2312.01548
[74] D. Webber, Y. Zhang, M. Picard, J. Boisvert, C. Paquet, and A. Orth, "Versatile volumetric additive manufacturing with 3D ray tracing," *Opt. Express*, vol. 31, no. 4, p. 5531, Feb. 2023, doi: 10.1364/OE.481318.
[75] A. Bagheri, M. R. Zakerzadeh, and M. J. Sadigh, "Weighting Method to Increase Print Fidelity of Filtered Back Projection Volumetric Additive Manufacturing Around Complex Inserts," in *2023 11th RSI International Conference on Robotics and Mechatronics (ICRoM)*, Tehran, Iran, Islamic Republic of: IEEE, Dec. 2023, pp. 682–686. doi: 10.1109/ICRoM60803.2023.10412496.
[76] T. H. Weisgraber, M. P. De Beer, S. Huang, J. J. Karnes, C. C. Cook, and M. Shusteff, "Virtual Volumetric Additive Manufacturing (VirtualVAM)," *Adv Materials Technologies*, vol. 8, no. 23, p. 2301054, Dec. 2023, doi: 10.1002/admt.202301054.
[77] J. T. Toombs *et al.*, "Volumetric additive manufacturing of silica glass with microscale computed axial lithography," *Science*, vol. 376, no. 6590, pp. 308–312, Apr. 2022, doi: 10.1126/science.abm6459.
[78] A. Orth *et al.*, "Deconvolution volumetric additive manufacturing," *Nat Commun*, vol. 14, no. 1, p. 4412, Jul. 2023, doi: 10.1038/s41467-023-39886-4.
[79] C. C. Cook *et al.*, "Highly Tunable Thiol-Ene Photoresins for Volumetric Additive Manufacturing," *Advanced Materials*, vol. 32, no. 47, p. 2003376, Nov. 2020, doi: 10.1002/adma.202003376.
[80] Q. Thijssen *et al.*, "Volumetric Printing of Thiol-Ene Photo-Cross-Linkable Poly(ε-caprolactone): A Tunable Material Platform Serving Biomedical Applications," *Advanced Materials*, vol. 35, no. 19, p. 2210136, May 2023, doi: 10.1002/adma.202210136.
[81] D. Gholobova, L. Terrie, M. Gerard, H. Declercq, and L. Thorrez, "Vascularization of tissue-engineered skeletal muscle constructs," *Biomaterials*, vol. 235, p. 119708, Mar. 2020, doi: 10.1016/j.biomaterials.2019.119708.
[82] L. Thorrez *et al.*, "Growth, differentiation, transplantation and survival of human skeletal myofibers on biodegradable scaffolds," *Biomaterials*, vol. 29, no. 1, pp. 75–84, Jan. 2008, doi: 10.1016/j.biomaterials.2007.09.014.
[83] L. Figueiredo *et al.*, "Assessing glucose and oxygen diffusion in hydrogels for the rational design of 3D stem cell scaffolds in regenerative medicine," *J Tissue Eng Regen Med*, vol. 12, no. 5, pp. 1238–1246, May 2018, doi: 10.1002/term.2656.
[84] C. Magliaro, G. Mattei, F. Iacoangeli, A. Corti, V. Piemonte, and A. Ahluwalia, "Oxygen Consumption Characteristics in 3D Constructs Depend on Cell Density," *Front. Bioeng. Biotechnol.*, vol. 7, p. 251, Oct. 2019, doi: 10.3389/fbioe.2019.00251.
[85] H. Heidari, "Fabrication of Extremely Soft Cellular Hydrogels for Vascular Modelling," Ph.D., University of California, Berkeley, United States -- California, 2020. Accessed: Jan. 07, 2024. [Online]. Available: https://www.proquest.com/docview/2560104447/abstract/D54167CE4D3B4AF8PQ/1
[86] S. M. Mavris and L. M. Hansen, "Optimization of Oxygen Delivery Within Hydrogels," *Journal of Biomechanical Engineering*, vol. 143, no. 10, p. 101004, Oct. 2021, doi: 10.1115/1.4051119.
[87] C. C. Li *et al.*, "Computational optimization and the role of optical metrology in tomographic additive manufacturing," in *Advanced Fabrication Technologies for Micro/Nano Optics and Photonics XV*, SPIE, Mar. 2022, pp. 38–44. doi: 10.1117/12.2610558.
[88] A. T. Young, O. C. White, and M. A. Daniele, "Rheological Properties of Coordinated Physical Gelation and Chemical Crosslinking in Gelatin Methacryloyl (GelMA) Hydrogels," *Macromolecular Bioscience*, vol. 20, no. 12, p. 2000183, Dec. 2020, doi: 10.1002/mabi.202000183.

[89] H.-Q. Xu, J.-C. Liu, Z.-Y. Zhang, and C.-X. Xu, "A review on cell damage, viability, and functionality during 3D bioprinting," *Military Med Res*, vol. 9, no. 1, p. 70, Dec. 2022, doi: 10.1186/s40779-022-00429-5.
[90] R. P. Sinha and D.-P. Häder, "UV-induced DNA damage and repair: a review," *Photochem Photobiol Sci*, vol. 1, no. 4, pp. 225–236, Apr. 2002, doi: 10.1039/b201230h.
[91] K. S. Lim *et al.*, "Visible Light Cross-Linking of Gelatin Hydrogels Offers an Enhanced Cell Microenvironment with Improved Light Penetration Depth," *Macromolecular Bioscience*, vol. 19, no. 6, p. 1900098, Jun. 2019, doi: 10.1002/mabi.201900098.
[92] "Resin Library and 3D Printing Materials," Formlabs. Accessed: Jan. 07, 2024. [Online]. Available: https://dental.formlabs.com/materials/#Surgical%20Guide%20Resin
[93] "Tango: A Soft Flexible 3D Printing Material." Accessed: Jan. 07, 2024. [Online]. Available: https://www.stratasys.com/en/materials/materials-catalog/polyjet-materials/tango/
[94] "Vero: Realistic Multi-Color 3D Printing Material." Accessed: Jan. 07, 2024. [Online]. Available: https://www.stratasys.com/en/materials/materials-catalog/polyjet-materials/vero/
[95] "SureSTART™ Specification Certified Shell Vial and Plug Kits, Level 1 Everyday Analysis." Accessed: Jan. 07, 2024. [Online]. Available: https://www.thermofisher.com/order/catalog/product/6EKSHV8-1
[96] "End Finishes for Tubing - Adams & Chittenden Scientific Glass Coop." Accessed: Jan. 07, 2024. [Online]. Available: https://adamschittenden.com/technical/material-properties/end-finishes-for-tubing
[97] "Resin Family: Tough and Durable | Formlabs." Accessed: Jan. 07, 2024. [Online]. Available: https://formlabs.com/materials/tough-durable/
[98] K. B. Djagny, Z. Wang, and S. Xu, "Gelatin: A Valuable Protein for Food and Pharmaceutical Industries: Review," *Critical Reviews in Food Science and Nutrition*, vol. 41, no. 6, pp. 481–492, Nov. 2001, doi: 10.1080/20014091091904.
[99] K. Yue *et al.*, "Structural analysis of photocrosslinkable methacryloyl-modified protein derivatives," *Biomaterials*, vol. 139, pp. 163–171, Sep. 2017, doi: 10.1016/j.biomaterials.2017.04.050.
[100] A. I. Van Den Bulcke, B. Bogdanov, N. De Rooze, E. H. Schacht, M. Cornelissen, and H. Berghmans, "Structural and Rheological Properties of Methacrylamide Modified Gelatin Hydrogels," *Biomacromolecules*, vol. 1, no. 1, pp. 31–38, Mar. 2000, doi: 10.1021/bm990017d.
[101] H. Shirahama, B. H. Lee, L. P. Tan, and N.-J. Cho, "Precise Tuning of Facile One-Pot Gelatin Methacryloyl (GelMA) Synthesis," *Sci Rep*, vol. 6, no. 1, p. 31036, Aug. 2016, doi: 10.1038/srep31036.
[102] K. Yue, G. Trujillo-de Santiago, M. M. Alvarez, A. Tamayol, N. Annabi, and A. Khademhosseini, "Synthesis, properties, and biomedical applications of gelatin methacryloyl (GelMA) hydrogels," *Biomaterials*, vol. 73, pp. 254–271, Dec. 2015, doi: 10.1016/j.biomaterials.2015.08.045.
[103] Y. Lee, J. M. Lee, P.-K. Bae, I. Y. Chung, B. H. Chung, and B. G. Chung, "Photo-crosslinkable hydrogel-based 3D microfluidic culture device," *ELECTROPHORESIS*, vol. 36, no. 7–8, pp. 994–1001, 2015, doi: 10.1002/elps.201400465.
[104] Y. Chen *et al.*, "Functional Human Vascular Network Generated in Photocrosslinkable Gelatin Methacrylate Hydrogels," *Adv Funct Materials*, vol. 22, no. 10, pp. 2027–2039, May 2012, doi: 10.1002/adfm.201101662.
[105] A. Orth *et al.*, "Optical Scattering Tomography for Volumetric Additive Manufacturing," in *Conference on Lasers and Electro-Optics (2022), paper ATh1D.3*, Optica Publishing Group, May 2022, p. ATh1D.3. doi: 10.1364/CLEO_AT.2022.ATh1D.3.
[106] C. Chung Li, J. Toombs, and H. Taylor, "Tomographic color Schlieren refractive index mapping for computed axial lithography," in *Symposium on Computational Fabrication*, Virtual Event USA: ACM, Nov. 2020, pp. 1–7. doi: 10.1145/3424630.3425421.

[107] I. S. Kinstlinger, G. A. Calderon, M. K. Royse, A. K. Means, B. Grigoryan, and J. S. Miller, "Perfusion and endothelialization of engineered tissues with patterned vascular networks," *Nat Protoc*, vol. 16, no. 6, Art. no. 6, Jun. 2021, doi: 10.1038/s41596-021-00533-1.
[108] S. De Boer *et al.*, "Endothelial characteristics in healthy endothelial colony forming cells; generating a robust and valid ex vivo model for vascular disease," *Journal of Thrombosis and Haemostasis*, vol. 18, no. 10, pp. 2721–2731, Oct. 2020, doi: 10.1111/jth.14998.
[109] E. Dejana, "Endothelial cell–cell junctions: happy together," *Nat Rev Mol Cell Biol*, vol. 5, no. 4, pp. 261–270, Apr. 2004, doi: 10.1038/nrm1357.
[110] L. Debbi, B. Zohar, M. Shuhmaher, Y. Shandalov, I. Goldfracht, and S. Levenberg, "Integrating engineered macro vessels with self-assembled capillaries in 3D implantable tissue for promoting vascular integration in-vivo," *Biomaterials*, vol. 280, p. 121286, Jan. 2022, doi: 10.1016/j.biomaterials.2021.121286.
[111] S. You *et al.*, "High cell density and high-resolution 3D bioprinting for fabricating vascularized tissues," *Sci. Adv.*, vol. 9, no. 8, p. eade7923, Feb. 2023, doi: 10.1126/sciadv.ade7923.
[112] L. Ouyang, J. P. K. Armstrong, Q. Chen, Y. Lin, and M. M. Stevens, "Void-Free 3D Bioprinting for In Situ Endothelialization and Microfluidic Perfusion," *Adv Funct Materials*, vol. 30, no. 1, p. 1908349, Jan. 2020, doi: 10.1002/adfm.201908349.
[113] B. Zohar *et al.*, "A micro-channel array in a tissue engineered vessel graft guides vascular morphogenesis for anastomosis with self-assembled vascular networks," *Acta Biomaterialia*, vol. 163, pp. 182–193, Jun. 2023, doi: 10.1016/j.actbio.2022.05.026.
[114] S. Romanazzo *et al.*, "Synthetic Bone-Like Structures Through Omnidirectional Ceramic Bioprinting in Cell Suspensions," *Adv Funct Materials*, vol. 31, no. 13, p. 2008216, Mar. 2021, doi: 10.1002/adfm.202008216.
[115] J. W. Tashman *et al.*, "In situ volumetric imaging and analysis of FRESH 3D bioprinted constructs using optical coherence tomography," *Biofabrication*, vol. 15, no. 1, p. 014102, Jan. 2023, doi: 10.1088/1758-5090/ac975e.
[116] D.-H. Kang *et al.*, "Engineered Whole Cut Meats Assembled of Cell Fibers Constructed by Tendon-Gel Integrated Bioprinting," In Review, preprint, Oct. 2020. doi: 10.21203/rs.3.rs-91978/v1.
[117] M. Kollep *et al.*, "Tomographic Volumetric Additive Manufacturing of Silicon Oxycarbide Ceramics," *Adv Eng Mater*, vol. 24, no. 7, p. 2101345, Jul. 2022, doi: 10.1002/adem.202101345.
[118] K. Matyjaszewski and M. Möller, Eds., *Polymer science: a comprehensive reference*. Amsterdam: Elsevier, 2012.
[119] M. G. Hennessy, A. Vitale, J. T. Cabral, and O. K. Matar, "Role of heat generation and thermal diffusion during frontal photopolymerization," *Phys. Rev. E*, vol. 92, no. 2, p. 022403, Aug. 2015, doi: 10.1103/PhysRevE.92.022403.
[120] T. Waddell *et al.*, "Use Of Volumetric Additive Manufacturing As An In-space Manufacturing Technology," in *Advancements in materials applications and rapid prototyping*, 72 st International Astronautical Congress (IAC), Sep. 2022. [Online]. Available: https://calfdm.com/wp-content/uploads/2022/09/IAC-CAL-final-15Sep22-print1.pdf
[121] R. Salajeghe, C. S. Kruse, D. H. Meile, D. Marla, and J. Spangenberg, "Investigating the influence of thermal and mechanical properties of resin on the sedimentation rate of the printed geometry in the volumetric additive manufacturing technique," 2022. doi: 10.26153/tsw/44203.
[122] R. Salajeghe, D. H. Meile, C. S. Kruse, D. Marla, and J. Spangenberg, "Numerical modeling of part sedimentation during volumetric additive manufacturing," *Additive Manufacturing*, vol. 66, p. 103459, Mar. 2023, doi: 10.1016/j.addma.2023.103459.
[123] R. J. C. Carbas, E. A. S. Marques, L. F. M. Da Silva, and A. M. Lopes, "Effect of Cure Temperature on the Glass Transition Temperature and Mechanical Properties of Epoxy Adhesives," *The Journal of Adhesion*, vol. 90, no. 1, pp. 104–119, Jan. 2014, doi: 10.1080/00218464.2013.779559.

[124] A. Tabatabaeian, A. R. Ghasemi, M. M. Shokrieh, B. Marzbanrad, M. Baraheni, and M. Fotouhi, "Residual Stress in Engineering Materials: A Review," *Adv Eng Mater*, vol. 24, no. 3, p. 2100786, Mar. 2022, doi: 10.1002/adem.202100786.
[125] D. A. Walker, J. L. Hedrick, and C. A. Mirkin, "Rapid, large-volume, thermally controlled 3D printing using a mobile liquid interface," *Science*, vol. 366, no. 6463, pp. 360–364, Oct. 2019, doi: 10.1126/science.aax1562.
[126] F. Jiang and D. Drummer, "Analysis of UV Curing Strategy on Reaction Heat Control and Part Accuracy for Additive Manufacturing," *Polymers*, vol. 14, no. 4, p. 759, Feb. 2022, doi: 10.3390/polym14040759.
[127] B. Ozkan, F. Sameni, A. Goulas, S. Karmel, D. S. Engstrøm, and E. Sabet, "Hot ceramic lithography of silica-based ceramic cores: The effect of process temperature on vat-photopolymierisation," *Additive Manufacturing*, vol. 58, p. 103033, Oct. 2022, doi: 10.1016/j.addma.2022.103033.
[128] F. Sameni, B. Ozkan, H. Zarezadeh, S. Karmel, D. S. Engstrøm, and E. Sabet, "Hot Lithography Vat Photopolymerisation 3D Printing: Vat Temperature vs. Mixture Design," *Polymers*, vol. 14, no. 15, p. 2988, Jul. 2022, doi: 10.3390/polym14152988.
[129] H. Zhang, Y. Zhang, and X. Zhao, "Predicting Process Temperature and Degree of Conversion in Vat Photopolymerization Additive Manufacturing: An Inverse Heat Conduction Approach," SSRN, preprint, 2023. doi: 10.2139/ssrn.4536009.
[130] H. Zhang and X. Zhao, "In-situ thermal monitoring informed modeling and simulation of process temperature during vat photopolymerization additive manufacturing," *Materials Today: Proceedings*, vol. 70, pp. 237–241, 2022, doi: 10.1016/j.matpr.2022.09.027.
[131] H. Wang, D. J. Kline, and M. R. Zachariah, "In-operando high-speed microscopy and thermometry of reaction propagation and sintering in a nanocomposite," *Nat Commun*, vol. 10, no. 1, Art. no. 1, Jul. 2019, doi: 10.1038/s41467-019-10843-4.
[132] E. Schena *et al.*, "Experimental assessment of CT-based thermometry during laser ablation of porcine pancreas," *Phys. Med. Biol.*, vol. 58, no. 16, pp. 5705–5716, Aug. 2013, doi: 10.1088/0031-9155/58/16/5705.
[133] E. Schena *et al.*, "Monitoring of temperature increase and tissue vaporization during laser interstitial thermotherapy of ex vivo swine liver by computed tomography," in *2013 35th Annual International Conference of the IEEE Engineering in Medicine and Biology Society (EMBC)*, Osaka: IEEE, Jul. 2013, pp. 378–381. doi: 10.1109/EMBC.2013.6609516.
[134] F. Fani, E. Schena, P. Saccomandi, and S. Silvestri, "CT-based thermometry: An overview," *International Journal of Hyperthermia*, vol. 30, no. 4, pp. 219–227, Jun. 2014, doi: 10.3109/02656736.2014.922221.
[135] A. H. Mahnken and P. Bruners, "CT thermometry: will it ever become ready for use?," *International Journal of Clinical Practice*, vol. 65, pp. 1–2, Apr. 2011, doi: 10.1111/j.1742-1241.2011.02651.x.
[136] P. Bruners *et al.*, "Multi-slice computed tomography: A tool for non-invasive temperature measurement?," *International Journal of Hyperthermia*, vol. 26, no. 4, pp. 359–365, Jan. 2010, doi: 10.3109/02656731003605654.
[137] G. D. Pandeya, M. J. W. Greuter, K. P. De Jong, B. Schmidt, T. Flohr, and M. Oudkerk, "Feasibility of Noninvasive Temperature Assessment During Radiofrequency Liver Ablation on Computed Tomography:," *Journal of Computer Assisted Tomography*, vol. 35, no. 3, pp. 356–360, May 2011, doi: 10.1097/RCT.0b013e318217121d.
[138] G. D. Pandeya *et al.*, "Feasibility of computed tomography based thermometry during interstitial laser heating in bovine liver," *Eur Radiol*, vol. 21, no. 8, pp. 1733–1738, Aug. 2011, doi: 10.1007/s00330-011-2106-6.
[139] A. Orth *et al.*, "On-the-fly 3D metrology of volumetric additive manufacturing," *Additive Manufacturing*, vol. 56, p. 102869, Aug. 2022, doi: 10.1016/j.addma.2022.102869.

[140] J. Zhou, B. del Rosal, D. Jaque, S. Uchiyama, and D. Jin, “Advances and challenges for fluorescence nanothermometry,” *Nat Methods*, vol. 17, no. 10, Art. no. 10, Oct. 2020, doi: 10.1038/s41592-020-0957-y.
[141] R. Mercadé-Prieto, L. Rodriguez-Rivera, and X. D. Chen, “Fluorescence lifetime of Rhodamine B in aqueous solutions of polysaccharides and proteins as a function of viscosity and temperature,” *Photochem Photobiol Sci*, vol. 16, no. 11, pp. 1727–1734, Nov. 2017, doi: 10.1039/c7pp00330g.
[142] M. A. Bennet, P. R. Richardson, J. Arlt, A. McCarthy, G. S. Buller, and A. C. Jones, “Optically trapped microsensors for microfluidic temperature measurement by fluorescence lifetime imaging microscopy,” *Lab Chip*, vol. 11, no. 22, pp. 3821–3828, Oct. 2011, doi: 10.1039/C1LC20391F.
[143] P. Lavieille, F. Lemoine, G. Lavergne, and M. Lebouché, “Evaporating and combusting droplet temperature measurements using two-color laser-induced fluorescence,” *Experiments in Fluids*, vol. 31, no. 1, pp. 45–55, Jul. 2001, doi: 10.1007/s003480000257.
[144] W. Van Aarle *et al.*, “Fast and flexible X-ray tomography using the ASTRA toolbox,” *Opt. Express*, vol. 24, no. 22, p. 25129, Oct. 2016, doi: 10.1364/OE.24.025129.
[145] F. L. Arbeloa, P. R. Ojeda, and I. L. Arbeloa, “FLUORESCENCE SELF-QUENCHING OF THE MOLECULAR FORMS OF RHODAMINE B IN AQUEOUS AND ETHANOLIC SOLUTIONS”.
[146] A. Vyšniauskas and M. K. Kuimova, “A twisted tale: measuring viscosity and temperature of microenvironments using molecular rotors,” *International Reviews in Physical Chemistry*, vol. 37, no. 2, pp. 259–285, Apr. 2018, doi: 10.1080/0144235X.2018.1510461.
[147] K. G. Casey and E. L. Quitevis, “Effect of solvent polarity on nonradiative processes in xanthene dyes: Rhodamine B in normal alcohols,” *J. Phys. Chem.*, vol. 92, no. 23, pp. 6590–6594, Nov. 1988, doi: 10.1021/j100334a023.
[148] C. M. Rackson *et al.*, “Latent image volumetric additive manufacturing,” *Opt. Lett., OL*, vol. 47, no. 5, pp. 1279–1282, Mar. 2022, doi: 10.1364/OL.449220.
[149] C. M. Rackson, “Fundamental Developments in Volumetric Additive Manufacturing,” Ph.D., University of Colorado at Boulder, United States -- Colorado, 2022. Accessed: Jun. 24, 2023. [Online]. Available: https://www.proquest.com/docview/2671944553/abstract/7D2531D42BFC444FPQ/1
[150] E. R. Ruskowitz and C. A. DeForest, “Photoresponsive biomaterials for targeted drug delivery and 4D cell culture,” *Nat Rev Mater*, vol. 3, no. 2, p. 17087, Jan. 2018, doi: 10.1038/natrevmats.2017.87.
[151] B. Wang *et al.*, “Stiffness control in dual color tomographic volumetric 3D printing,” *Nat Commun*, vol. 13, no. 1, p. 367, Jan. 2022, doi: 10.1038/s41467-022-28013-4.
[152] A. A. Szklanny *et al.*, “3D Bioprinting of Engineered Tissue Flaps with Hierarchical Vessel Networks (VesselNet) for Direct Host-To-Implant Perfusion,” *Advanced Materials*, vol. 33, no. 42, p. 2102661, Oct. 2021, doi: 10.1002/adma.202102661.
[153] T. Grix *et al.*, “Bioprinting Perfusion-Enabled Liver Equivalents for Advanced Organ-on-a-Chip Applications,” *Genes*, vol. 9, no. 4, p. 176, Mar. 2018, doi: 10.3390/genes9040176.
[154] Q. Thijssen, J. Toombs, C. C. Li, H. Taylor, and S. Van Vlierberghe, “From pixels to voxels: A mechanistic perspective on volumetric 3D-printing,” *Progress in Polymer Science*, vol. 147, p. 101755, Dec. 2023, doi: 10.1016/j.progpolymsci.2023.101755.
[155] D. D. La, S. V. Bhosale, L. A. Jones, and S. V. Bhosale, “Tetraphenylethylene-Based AIE-Active Probes for Sensing Applications,” *ACS Appl. Mater. Interfaces*, vol. 10, no. 15, pp. 12189–12216, Apr. 2018, doi: 10.1021/acsami.7b12320.